NUCLEI ON THE MOVE -

Physical Aspects of Interkinetic Nuclear Migration

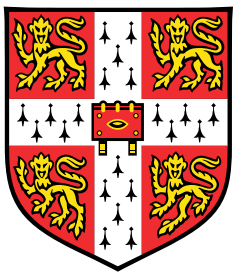

Anne Herrmann

Department of Applied Mathematics and Theoretical Physics
University of Cambridge

This dissertation is submitted for the degree of
Doctor of Philosophy

Clare Hall

February 2020

Declaration

I hereby declare that this dissertation is the result of my own work and includes nothing which is the outcome of work done in collaboration except as declared in the Preface and specified in the text. It is not substantially the same as any that I have submitted, or, is being concurrently submitted for a degree or diploma or other qualification at the University of Cambridge or any other University or similar institution. I further state that no substantial part of my dissertation has already been submitted, or, is being concurrently submitted for any such degree, diploma or other qualification at the University of Cambridge or any other University or similar institution.

The work presented in Chapter 5 is the result of a collaboration with Afnan Azizi, a PhD student of Prof. William A. Harris (Department of Physiology, Development and Neuroscience, University of Cambridge) at that time. I initiated this collaboration. All experimental data underlying the work in this dissertation has been made available to me in the framework of this collaboration, as outlined in Chapter 4. Further details regarding the exact contributions of Afnan Azizi and myself, as well as our respective Supervisors Prof. William A. Harris and Prof. Raymond E. Goldstein can be found at the beginning of Chapters 4 and 5. Except for my Supervisor, the remaining chapters are not collaboratory. Any input provided as the result of discussions with other people and any data acquisition performed by other people is specifically mentioned at the beginning of each Chapter or in the text in Chapters 4, 5, 6 and 7.

Despite this, I will exercise nosism throughout.

Anne Herrmann
February 2020

Abstract

Anne Herrmann

NUCLEI ON THE MOVE - Physical Aspects of Interkinetic Nuclear Migration

Embryonic development is a highly complex procedure, leading from initial, unspecialised cell types - the stem cells - to ever more specialised ones. In part, this process is regulated by genes; but interactions between cells, such as mechanical contacts and the exchange of diffusive signalling molecules, also play pivotal roles for the correct execution of developmental programmes. Therefore, unravelling the rules of cell differentiation requires insights from both biology and physics.

In this dissertation, we focus on the process of interkinetic nuclear migration (IKNM). IKNM takes place in cells of so-called pseudostratified epithelia (PSE) during development. In these tissues, the nuclei of cells move in a cell cycle dependent manner and position themselves in a specific region of the cells for each cell division. The correct nuclear positioning has been shown to be crucial for proper development in PSE. And because organs like the brain and the spinal cord develop from pseudostratified epithelial tissues, IKNM appears to be of paramount importance for the entire embryo.

The work presented here concerns IKNM in the retina, an experimentally accessible outgrowth of the brain, and relies on experimental data obtained from zebrafish. However, the conclusions are likewise relevant for understanding the development of many other PSE tissues.

Based on the experimental data, two previously posed hypotheses on how the majority of nuclear movements might be driven can be tested. The data is consistent with the idea that nuclear movements depend on the build-up of a gradient in nuclear packing density across the retinal tissue. Consequently, we develop the first mathematical model for the distribution of nuclei across the retinal tissue as a function of time. Underlying this model is the notion that individual nuclear trajectories phenomenologically resemble random walks during most of the cell cycle. Therefore, we model the time evolution of the nuclear density

using a diffusion equation with an effective diffusion constant to be determined from the data. Furthermore, we specifically account for the fact that nuclear divisions always take place in a defined region of the cells - leading to the aforementioned gradient in nuclear packing density. Finally, we also pay attention to the spherical geometry of the retinal tissue. Although the simplest linear model describes well the data from early in the experiments, it fails to do so for data from later stages in which nuclei approach close-packing. We hypothesise that the reason for this mismatch between model and data might result from the neglect of crowding. Therefore, we present a second, nonlinear model which now takes the volume of nuclei into account by introducing a maximum possible packing density. This enables us to replicate the experimental nuclear distribution across the whole range of experimental time points. We finally employ this second model to make statements about the influence of experimental parameters, specifically incubation temperature, on the dynamics of IKNM. The result also provides some indications for possible microscopic mechanisms underlying the nuclear movements.

Having studied the distribution of nuclei across the retinal tissue, we aim to investigate the significance of our obtained results on the level of individual cells. First, we compare the mobility of nuclei during IKNM with the expected mobility in the cases of Brownian motion and membrane-hindered Brownian motion. We find that IKNM appears to be both membrane-hindered and additionally driven throughout the entire cell cycle. Assuming a stochastic driving force and calculating its typical strength we deduce IKNM to be consistent with cytoskeletal transport. We then devise possible Langevin models for individual nuclear movements which are consistent with the model for the distribution of nuclei derived previously. The numerical simulation of each of these Langevin models enables us to distinguish between them; we identify the model which most likely reflects the biological process in each individual cell. This again leads to predictions about the potential microscopic underpinnings of nuclear movements during IKNM.

The apparent importance of the cell membrane in restricting nuclear mobility prompts us to examine the shape of PSE cells in closer detail. We numerically solve the Helfrich elastic model for lipid bilayers for increasingly large cell aspect ratios. In the case of long, slender cells and high membrane tension, we recover shapes not unlike those previously reported for membrane tethers. In contrast, shorter cells are almost cylindrical. The results of this systematic investigation into cell shapes might explain the different geometries of cells in various types of PSE. Furthermore, they might also be of relevance for more generally understanding peculiar cell shapes, such as those of neurons.

Dorothy Crowfoot Hodgkin (The Nobel Prize in Chemistry 1964), Address to the University Students on the Evening of December 10, 1964: '*I was chosen to reply to you this evening as the one woman of our group, a position, which I hope very much will not be so very uncommon in future that it will call for any comment or distinctions of this kind, as more and more women carry out research in the same way as men.*' [1]

More than 50 years on, it seems Dorothy Crowfoot Hodgkin's hope has still not come true - although I first saw this quote in a book that I had been given by another female researcher, my dear friend Maria.

So this is to all the young people around the globe who dream of making the world a better place through science and who fight for true equality among all humans.

Acknowledgements

My deepest gratitude goes to my Supervisor, Raymond E. Goldstein. I feel extremely honoured that I had the opportunity of learning from and working with Ray, a person with a tremendous breadth of scientific knowledge and thus a source of great inspiration for me. Ray also taught me that every person is equipped with their own scientific tools and that life as a scientist is not about mastering the exact same tools as everybody else but about tackling the unknown with the tools at one's disposal. Finally, Ray encouraged me not to go for the low hanging fruit, but to ask the (potentially) hard questions also and to embrace the possibility of strenuous work to get to the answer. As a result of this, Ray challenged me to define my own PhD research questions, and I am enormously proud to say that I successfully rose to the task.

During the period of determining my project, I had the opportunity to meet many brilliant biologists across the University of Cambridge and discuss possible ideas with them. For this, I would like to thank Alfonso Martinez Arias (Department of Genetics), David Turner, Vikas Trivedi and Naomi Moris from Alfonso's group, Cristina Pina (Department of Haematology), Ben Steventon (Department of Genetics) and Andrea Attardi from Ben's group, Octavian Voiculescu (Department of Physiology, Development and Neuroscience), William A. Harris (Department of Physiology, Development and Neuroscience), Afnan Azizi and Megan K. Eldred from Bill's group, Magdalena Zernicka-Goetz (Department of Physiology, Development and Neuroscience), Marta Shahbazi, Sarah Harrison and Neophytos Christodoulou from Magdalena's group and John B. Gurdon (The Gurdon Institute).

In the end, I established a very fruitful and fun collaboration with Afnan Azizi, who shared all his experimental data with me. In this way, it is due to Afnan and Bill that I am now able to write this dissertation at all. I would also like to thank Afnan and Bill for countless discussions about our joint work and for providing alternative points of view on many aspects of the project at hand. Even after the end of Afnan's own PhD, both continued

to stay trusted colleagues, helping with aspects related to the project and far beyond.

Through the collaboration with Afnan, I also obtained access to a set of data that had originally been provided to him by Yinan Wan and Philipp J. Keller (Howard Hughes Medical Institute, Janelia Research Campus, Ashburn, VA, USA) as outlined in the main text. This data set forms an important part of our work.

No less heartfelt than the acknowledgement of my collaborators are my thanks going to the members of both Ray's group and Eric Lauga's group at the Department of Applied Mathematics and Theoretical Physics. Kirsty Y. Wan, François J. Peaudecerf, Julius B. Kirkegaard, Gabriele de Canio, Francesco Boselli, Hélène de Maleprade, Pierre A. Haas, Stephanie Höhn, Mazi Jalaal, Kyriacos Leptos, Nuno Miguel Oliveira, George T. Fortune, Michael Gomez, Emily Riley, Tamsin Spelman, Justas Dauparas, Panayiota Katsamba, Lyndon Koens, Maciej Lisicki, Maria Tătulea-Codrean, Alexander J. Chamolly, Debasish Das, Mariia Dvoriashyna, Christian Esparza-López, Ivan Tanasijevic and Albane Théry have made biophysics come to life during office hours and also made life worth living in Cambridge outside the CMS.

Many other people have contributed to the scientific environment that I was able to enjoy during my PhD. First and foremost among them are my Advisor Michael E. Cates, Eric Lauga, Timothy J. Pedley and John R. Lister. In Clare Hall, my College Tutors Wai Yi Feng and Tobias Baldauf deserve my gratitude for their support. Too many people for me to be able to name have been a part of my social life both in the Faculty of Mathematics and Clare Hall. I am thankful to all of you.

Finally, I would like to say thank you to some very important people in my life. Without my mum, dad, sister, brothers and my boyfriend Philipp, I would not be where I am today. From the earliest parts of this journey to this day, they have given me all their love and support. In particular, Philipp has only ever given me his strongest encouragement, although this meant we both had to subordinate many private dreams. This sacrifice he was willing to make is still beyond belief to me. Now, I am more than excited about the future.

The work in this dissertation was supported by a grant from the Engineering and Physical Sciences Research Council, a Helen Stone Scholarship at the University of Cambridge awarded by The Cambridge Commonwealth, European and International Trust, and a grant from the Cambridge Philosophical Society.

Table of Contents

List of Figures

List of Tables

List of Abbreviations

AC	aphidicolin
LT	low temperature
hpf	hours post fertilisation
HT	hight temperature
HU	hydroxyurea
IKNM	interkinetic nuclear migration
MSD	mean-squared-displacement
PTU	phenylthiourea
PSE	pseudostratified epithelium
RPC	retinal progenitor cell
RE	relative error

A list of all relevant variables can be found at the beginning of each of the Chapters 5, 6 and 7.

Chapter 1

Introduction

Life on earth is breathtakingly complex. Based on a small number of molecular building blocks [2], millions of species have evolved [3]. Even today only a fraction or them are known to mankind [4]. Some organisms are unicellular - meaning they consist of just one cell which performs all the tasks necessary for survival and reproduction. In contrast, multicellular organisms consist of many cells that are permanently conjoined.

Within such groups of cells specialisation of cell types can occur. In this case, each individual cell only performs a small number of specific tasks (and typically is not capable of surviving by itself). Nonetheless, strikingly, during embryonic development multicellular animals and plants in all their complexity grow from a single, unspecialised cell.

How does this process of embryonic development work? How does, e.g., a human body with an estimated 3.72×10^{13} cells [5] develop from that one single, initial cell? In part, this is a genetics question. Within a multicellular organism, each cell usually contains the exact same genetic information as all the other cells. The cell types solely differ because they make use of this information in different ways [2]. But then, how does each individual cell know which genetic programmes to use at any given time and in a given part of the body? Again genetics holds part of the answer, as some genetic programmes also regulate the execution of others. However, interactions between cells and environmental factors can be equally important.

Depending on the organism at hand, the influence of the numerous forms of developmental regulation can vary considerably. For example, the cell division and differentiation steps in *Caenorhabditis elegans*, a nematode worm, are tightly controlled [6] [2]. This does not appear to be the case in some other organisms. Perhaps most dramatically, early

mammalian embryos can split into identical twins or merge into chimaeras, demonstrating the ability of these embryos to adapt to enormous disturbances in their usual developmental course.

Because of these drastic differences between species and the multitude of pathways involved, understanding how embryonic development is regulated remains a major scientific challenge. Furthermore, the full appreciation of the complexity of development also provides crucial insights to understand developmental anomalies and other disease.

Here, we are concerned with a process that appears to be essential for the proper development of the nervous system and other organs. These organs develop from tissues called pseudostratified epithelia (PSE); named this way because of their specific tissue architecture, consisting of a single layer of long, columnar cells. Within these cells the nuclei move in a cell cycle dependent manner during embryonic development. This process has been termed interkinetic nuclear migration (IKNM). While undergoing IKNM, the nuclei assume a particular position inside the cells for each cell division. If this nuclear positioning is disturbed, PSE tissues develop abnormally. Thus - as the brain, spinal cord and other organs grow from PSE - IKNM plays a crucial role in the developing embryo.

Although IKNM has first been described in 1935 [7] and has since been studied in multiple organisms, many questions about its precise mechanism remain.

In this dissertation, we study IKNM based on experimental data obtained from the zebrafish (*Danio rerio*) retina. The retina, being an outgrowth of the brain [8], serves as an important model system for neuroscience research. Compared to the brain, the retina is more easily accessible experimentally [9]. Therefore, live imaging techniques can be employed. Furthermore, the presented methods and drawn conclusions can straightforwardly be applied to other PSE systems.

Before presenting said work, we first briefly introduce multicellularity and some aspects of animal cell biology and development in Chapter 2. Additionally, we characterise pseudostratified epithelia in general and the zebrafish retina in particular in further detail. Finally, we illustrate how IKNM could be involved in regulating development and summarise previous work on the possible mechanisms that drive nuclear movements in the various PSE tissues.

In Chapter 3, we give a very short overview of the physical concepts and relevant equations underlying our work. We summarise some basic concepts relating to random motion, including the diffusion equation, Langevin equations (a type of stochastic differential equations) and the link between the two. Afterwards, we review properties of a thermodynamic model system called the lattice gas. Then, we introduce a theory for the physics of cell membranes known as the Helfrich elastic model for lipid bilayers [10] and lastly we outline a numerical procedure to solve stochastic differential equations.

Then, in Chapter 4, we outline the data acquisition and handling. All experimental data used in this dissertation has been made available in the framework of a collaboration with Afnan Azizi, a PhD student of Prof. William A. Harris (Department of Physiology, Development and Neuroscience, University of Cambridge) at that time. Unless specified otherwise, imaging and post-processing have been performed by Afnan Azizi [11]. Thus in this Chapter, we illustrate the state of processing in which the data was obtained for further analysis.

In the following Chapters 5 to 7 we present the results of our investigation into three different physical aspects of IKNM.

First, we examine IKNM on the tissue level. Previous studies have mostly been based on imaging single or sparsely labelled cells or nuclei in an otherwise unlabelled tissue. However, this approach cannot assess any collective effects and interactions between the nuclei, which are tightly packed within PSE. Thus, the work presented in Chapter 5 focusses on these tissue level phenomena. Based on the experimental data, we analyse possible driving mechanisms for the nuclear movements observed during IKNM and derive mathematical models for the distribution of nuclei across the tissue over time. The results are consistent with the existence of significant interactions between the nuclei.

Therefore, in Chapter 6, we extend our attention to the level of individual nuclei. Here, in contrast to previous work, we explicitly take the aforementioned nuclear interactions into account. We devise a stochastic model for the nuclear movements and again match it to the experimental data. Using this model we are also able to make some predictions about the possible microscopic mechanisms involved in IKNM.

In Chapter 7 we continue to focus on the single cell level but divert our attention away from the nuclei themselves. Instead, we concentrate on the fgeometry of the cells in

pseudostratified epithelia. As these cells are very slender and in fact often thinner than the nuclear diameter, we expect large membrane deformations to occur due to the IKNM movements. We study the membrane shape using the Helfrich elastic model for lipid bilayers and specifically consider the tissue architecture in PSE and the presence of the nuclei.

Finally, in Chapter 8, we summarise our results and conclude by sketching possible future lines of enquiry into IKNM and its role in the development of PSE tissues.

Chapter 2

Biological background

2.1 Multicellularity

In physics, we are well aware that all (visible) matter in the universe is constructed of only a few different particles and their interactions [12]. Intriguingly, when many particles come together, new properties of the system, that the individual constituents do not possess, emerge. In addition, such many particle systems can produce large-scale patterns, as is known for example for the Ising model [13] [14] [15].

In analogy to these physical systems, we can think of biological systems as being constructed from certain individual constituents with interactions between them [16] [17]. Some of the levels of organisation we can identify are:

- the interaction of simple organic molecules to form living entities, i.e. cells [2].
- the interaction of cells to form multicellular organisms and organs within them, e.g. [18].
- the interaction between individual organisms to form groups and ecosystems, e.g. [19].

Again, some of these biological systems can exhibit complex large-scale patterns [20], for instance the stunning skin, scale and fur patterns of animals such as nudibranchs (a group of sea slugs) [21], fish [22], lizards [23] and zebras [24], human finger prints [25], as well as the travelling waves observed in starving *Dictyostelium discoideum* [26].

Focussing on the second level of biological organisation listed above, we can investigate what steps cells had to take to transition from unicellular to multicellular organisms. Furthermore, we can assess the system properties that newly emerged with multicellularity and finally examine the interactions that are needed for multicellular organisation to occur.

2.1.1 The evolution of multicellularity

The transition from unicellular to multicellular life has taken place many times across the domains of life. Yet, this transition does not consist of just a single step, hence different organisms have gone different parts of this way [27]. Perhaps colonial life forms can be understood as the first step on the path to multicellularity. Colonial life forms exist in both prokaryotes (i.e. bacteria and archaea) and eukaryotes (all other organisms) [28]. Among the prokaryotes, many bacteria are known to form surface-associated biofilms when they encounter a suitable environment (compare e.g. [29]). Likewise, unicellular eukaryotes such as the amoeba *Dictyostelium discoideum* or choanoflagellates (the closest relatives of animals) form colonial associations under certain circumstances like starvation in the case of *D. discoideum* [26] [30]. Additionally, aggregation of cells can be induced in some normally unicellular organisms under specific laboratory conditions [31] [32]. Further steps in the transition to so-called complex multicellularity include obligatory multicellularity without cell type differentiation, cell type differentiation (which in the simplest case means differentiation into reproductive and body cells, i.e. germ-soma differentiation) and the emergence of specialised tissues (compare e.g. [27] [33] [34]). Among the plants the volvocine green algae have become model organisms to study the emergence of multicellularity as this group of closely related organisms contains the unicellular genus *Chlamydomonas*, several multicellular but undifferentiated taxa as well as the germ-soma differentiated genus *Volvox* [35]. Among the animals, members of the early diverging lineages Ctenophora (comb jellies), Porifera (sponges) and Placozoa show cell type differentiation but only the onset of true tissues and their exact phylogenetic relationship is still under debate [36] [37] [38] [39] [40].

2.1.2 Key properties of multicellular organisms

What are the required cellular properties permitting the existence and functioning of multicellular organisms? Srivastava et al. [37] list six characteristics of multicellularity in animals: '*(1) regulated cell cycling and growth; (2) programmed cell death; (3) cell–cell and cell–matrix adhesion; (4) developmental signalling and gene regulation; (5) allorecognition and innate immunity; and (6) specialization of cell types*'. More generally speaking, cell adhesion and cell signalling play key roles in the transition to multicellular life [33] [34]. Many genomic domains enabling these traits are present also in the unicellular relatives of multicellular organisms, indicating their potential involvement in the evolution of multicellularity [41] [42].

2.1.3 Interacting cells - cell adhesion and cell signalling at a glance

Cell adhesion not merely leads to cells sticking together, forming a multicellular unit. Rather, it also endows the cells with the capability to mechanically interact with other cells and their surrounding extracellular matrix [18]. These interactions are elementary for a multitude of features such as cell division [18], tissue growth [43] [44], the establishment of tissue boundaries [45] [46] [47] [48], cell migration during development [49] [50] and wound healing. Moreover, cells can sense applied stresses and strains and interpret them as mechanical signals [51]. These mechanical signals, like other signals interpreted by the cells, can induce changes in the cellular behaviour and even contribute to the progression of cancer [51].

Cell signalling is crucial not only for the cells in complex multicellular organisms but even for the unicellular bacteria [52]. Signalling enables cells to match their behaviour (which is important e.g. to organise embryonic development) [53] [54], distinguish between 'self' and 'other' and resolve conflicts [55]. Beside mechanical signalling, cells can also exchange chemical signalling molecules and ions [2]. If the signalling molecules released by one set of cells influence the development of another, they are called morphogens [56].

2.2 Animal cells, development and its regulation

During embryonic development, a multicellular animal (or plant) grows from a single, unspecialised cell. Undergoing this process, the cell divides many times and its daughter cells become more and more specialised. While the differentiated (i.e. final) cell types differ in their exact properties due to their specific functions, all animal cells possess some common fundamental components.

2.2.1 Some basic components of animal cell architecture

Cells are enlosed by a so-called cell membrane or plasma membrane (Figure 2.1, in grey). The cell membrane is a bilayer of various phospholipids which contains embedded cholesterol and proteins of diverse functions. This lipid-bilayer surrounds the cytoplasm - the inside of a cell - with its multiple components. These components all reside directly in the cytosol, the liquid component of the cytoplasm, in prokaryotic cells. In contrast, the inside of eukaryotic cells is heavily substructured. As animal cells are eukaryotic cells, they exhibit this substructuring. Most importantly, in eukaryotic cells the DNA is packed

inside the nucleus [28] (hence the term 'eukaryotic', meaning 'true nucleus' [57]), a specific membrane-enveloped region inside the cell (Figure 2.1, in green). Further to the nucleus, other membrane-bounded intracellular domains of separate functions, the organelles, can be identified (Figure 2.1, in yellow). Some of these exist in all eukaryotic cells, while others are specific to certain groups of organisms. For example, animal cells do not possess chloroplasts to perform photosynthesis, but plant cells do. In addition, eukaryotic cells contain structural poteins, collectively named the cytoskeleton (Figure 2.1, in blue) [28].

The cytoskeleton consistes of three different types of polymeric proteins with distinct physical properties and multiple functions: actin filaments (called microfilaments as well), microtubules and intermediate filaments (Figure 2.1 in dark, medium and light blue, respectively). The latter term describes, in contrast to the other two, a whole number of different proteins. Actin filaments play crucial roles in the mechanical stability and contractility of a cell. As such, they are relevant also for cell movements and cell division. Microtubules form intracellular networks along which directed cargo transport and DNA separation during cell division take place. Both the contractility of the actin cytoskeleton as well as the transport processes along the microtubules are enabled by so-called molecular motors (e.g. myosin motors in the case of actin). These are proteins undergoing conformational changes under the consumption of chemical energy. Cyclic repetition of these conformational changes leads to the motors moving along or pulling on the cytoskeleton. Intermediate filaments again provide mechanical stability to the cells [28] [58]. Furthermore, it recently emerged that the cytoskeleton might be relevant to provide additional stability to the nucleus [59]. This is important, as the nucleus is often the largest structure inside a cell and as such can be subject to mechanical stresses [60], but large deformations can lead to nucleus and DNA damage [61].

2.2.2 On the development of multicellular animals

The life of a multicellular animal begins with fertilisation, the fusion of a sperm and an egg cell. Afterwards, the fertilised egg divides many times, giving rise to so-called blastomeres which typically form a (hollow) sphere of cells, the blastula. The cells than undergo drastic rearrangements with the whole cell sheet folding inwards, a process termed gastrulation. Afterwards, the embryo consists of three layers of cells (or two in basal animals): the ectoderm on the outside, the endoderm on the inside and the mesoderm (which is missing in the basal animals) between the other two. The cells of these three germ layers continue dividing and produce more and more specialised daughter cells during the processes of organogenesis and histogenesis (the formation of organs and tissues). In these phases of development progenitor

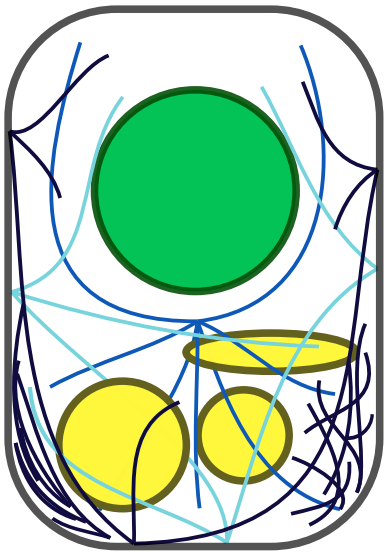

Figure 2.1 **Simplified schematic of an animal cell.** This schematic of an animal cell has been strongly simplified to focus on the components relevant to this dissertation. It shows the cell membrane (grey), the nucleus (green) and the cytoskeletal components (blue) with actin (dark blue), microtubules (medium blue) and intermediate filaments (light blue). Additionally, the presence of other cytoplasmic components and organelles is indicated (yellow). The schematic is loosely based on information provided in [28] [58]. It is not based on any particular cell type or stage of the cell cycle and is not to scale.

cells occur, which can still divide but are already steered towards certain fates and finally give rise to the differentiated cells. For example, the ectoderm forms the outer layer of the skin and the nervous system, the mesoderm muscles, skeleton and kidneys and the endoderm the digestive organs [62] [40].

2.2.3 Different modes of developmental regulation

Multicellular organisms have evolved a myriad of regulatory mechanisms for development. In some cases, termed mosaic development, cell fates are determined based on cell intrinsic properties and developmental history alone. In contrast, in so-called regulative development, cell fates are assigned based on non-cell-autonomous mechanisms [63].

Classic examples of mosaic development include the embryonic development of ascidians (sea squirts) and of the nematode worm *Caenorhabditis elegans* (*C. elegans*). Within the ascidians, even distantly related species exhibit similar early embryonic developmental patterns [64] [65] [66]. Likewise, the cell division and differentiation pattern in *C. elegans* is

strictly defined. Here, each adult individual has precisely the same number of cells (959 in the hermaphrodite and 1031 in the male) [2] and the full lineage tree for all of these cells can be mapped out [6].

However, closer examination revealed that even in these prime examples of mosaic development, interactions between the cells are crucial. For example in ascidian development, only very few cells seem to develop completely autonomously. The fates of other cells are determined by short-range inductions, wherby the contact area between cells appears to play a role [65]. Somewhat similarly, in *C. elegans*, exchanging the positions of 2 blastomeres or otherwise altering their interactions by removing one of them from the embryo also alters the fates of subsequently produced cells [67] [63].

The most dramatic examples of regulatory development are probably identical twins and chimaeras - two phenomena that also naturally occur in humans. In the case of identical twins, a single embryo splits into two during the early stages of development. Both resulting bodies can compensate for the loss of the respective other half of the cells and recover to grow normally. In chimaeras, the inverse process takes place. If combined, two different embryos can merge into one, again compensate for the change and form a single organism with cells from both original ones [63].

There are different ways in which such compensating behaviour might be achieved. On the one hand, cells might act independently from one another but without a strict genetic or lineage specification of their fates. Nevertheless, their individual fate choices can result in a advantageous outcome for the whole system. On the other hand, cells might also signal each other and in this way determine their fate as a collective.

Some important lessons about independent cellular decisions leading to group benefits can be learned from unicellular organisms. Consider the germination behaviour of the soil bacterium *Bacillus subtilis*. Under unfavourable conditions, *Bacillus subtilis* produces bacterial spores. These are extremely resistant forms that can often endure in the soil for years [68]. However, as a trade-off, their capability to monitor the environment for the occurrence of favourable conditions in decreased [69]. Therefore it is thought that *Bacillus subtilis* apply a bet hedging strategy. Sturm and Dworkin [69] reported that bacterial spores germinate at a low but measurable rate even in the absence of any known germination inducer. If, at any time, the few germinating bacteria encounter appropriate conditions they can grow into a new colony, while the remaining spores persist if the germinating cells do not [69]. In this way,

although each cell appears to germinate completely independently, they collectively ensure survival. Similar examples of (seemingly) random behaviour include bacterial switching under stress line nutrient-deprivation or the presence of antibiotics [70] and the lysis-lysogeny decision in the bacteriophage lambda (a virus infecting bacteria) [70] [71].

In multicellular eukaryotes, stochastic fate choices can serve as a way to achieve an otherwise unmanageable complexity of cell types [72]. For example, in the olfactory system of mice, each cell randomly expresses a different one of a very large number odorant receptors [72] [73] [74]. This random expression appears to be much easier to regulate than an explicit genetic encoding of the receptor distribution among the sensory neurons. In a similar manner, tissue development and self-renewal (called homeostasis) can be explained under the assumption that only the stem cell division rates and the probabilities of certain cell fates are fixed, but individual fate choices are stochastic [75] [76] [77].

In all of the above examples, cells appear to adapt certain fates independently from one another. However, the opposite case is also common. As already mentioned above, blastomores in the early development of ascidians and *C. elegans* require direct contact with certain neighbouring cells to produce the right types of offspring. In other organisms, cells only differentiate when they are in close association with many of their like, an aspect termed community effect [78] [79] [80] [81]. A similar phenomenon is even known in bacteria, where it is called quorum sensing. Here, certain bacterial competences like light production or pathogenicity only become activated when the bacterial density is high (or low) enough [52]. Further to such collective cellular behaviour, vertebrates also possess cells that exist primarily to direct the developmental fate choices of other cells [82] [83].

Unfortunately, vertebrate development is often challenging to study. On the one hand, it is difficult to experimentally observe developmental processes in vertebrates directly for both biological and ethical reasons. On the other hand, many of the aspects described above heavily interact with each other, adding to the complexity of the puzzle.

2.3 Pseudostratified epithelia

In the following, we focus on the development of the retina in zebrafish (*Danio rerio*). The retina constitutes an important model system for neuroscientific research because it develops as an outgrowth of the brain. Furthermore, in contrast to other neural tissues, the retina of

zebrafish can easily be observed experimentally during development.

Classified by tissue architecture, the developing zebrafish retina constitutes a so-called pseudostratified epithelium.

2.3.1 What are pseudostratified epithelia?

Pseudostratified epithelia (PSE) are a specific type of epithelial tissues. Epithelia are one of the basic classes of animal tissues and often form the surfaces of organs and other structures. Based on their cell shape, epithelia are classified into squamous (flat cells), cuboidal or columnar and based on the number of cell layers they are called simple (one cell layer) or stratified, i.e. layered [62].

Epithelial cells stand out from other cell types due to their multiple types of tight cell-cell connections as well as their cell polarity. The cell-cell connections mechanically link the cells and enable an epithelium to form a sealed tissue layer (necessary e.g. to line the inner intestine surfaces) [2]. Thus, there is no extracellular space between the individual epithelial cells. Furthermore, epithelial cells possess a so-called cell polarity, meaning they have two distinguishable sides. The apical side usually faces the outside of the tissue, e.g. the lumen of the intestine. The basal side normally connects the epithelium to a network of extracellular components - the basement membrane or extracellular matrix - on which the tissue resides.

Pseudostratified epithelia are epithelial tissues with a distinctive tissue architecture. Although they consist of one layer of columnar cells like other simple epithelia, they appear to be stratified tissues. This is due to the arrangement of the cells' nuclei. PSE cells can be very small in diameter but long in the apicobasal direction and within those cells, individual nuclei are positioned at different distances from the apical and basal cell surfaces. This organisation generally gives the PSE a stratified semblance, although the exact cell aspect ratio and packing density varies between the different PSE tissues [62] [84].

In addition to their specific tissue architecture, pseudostratified epithelia also serve a different function than other epithelia. Instead of forming surfaces, PSE appear during the development of a variety of organs and their cells are highly proliferative (i.e. they undergo a large number of cell divisions) [84]. Pseudostratified epithelia can be found in both invertebrates (e.g. in the sea anemone *Nematostella vectensis* and the fruit fly *Drosophila melanogaster* [85]) and vertebrates during development. In vertebrates, PSE contribute to

the development of organs such as the lung and liver [84] as well as the organs of the central nervous system, i.e. the brain and spinal cord [86] [87] [88] [84].

2.3.2 The zebrafish retina

Being an outgrowth of the brain [89], the zebrafish retina develops from a pseudostratified epithelium. The cells in this PSE tissue give rise to all cell types in the retina [90] and are thus called retinal progenitor cells (RPCs). RPCs in zebrafish are approx. 50 - 60 µm long in the apicobasal direction and thin perpendicular to it, bulging around their nuclei (see Figure 2.2 (a)). In the developing fish eye, the retinal pseudostratified epithelium forms a cup shape around the lens with the RPCs pointing radially outward. In this arrangement, the basal surfaces of the cells face the lens and the apical surfaces away from it (compare Figure 2.2 (b)).

During development, retinal progenitor cells undergo a phase of substantial proliferation (i.e. cell divisions), beginning at approx. 24 hours post fertilisation (hpf), before they differentiate [89]. Eventually, the RPCs begin to adopt neuronal fates. Once this cell fate differentiation takes place, the cells leave the original monolayer of the PSE and migrate to their final positions within the retina (compare e.g. [91]). At about 72 hpf the cell differentiation is completed [89] [91]. At the end of this process, the retina is composed of several layers consisting of different cell types. In total, the zebrafish retina contains six types of cells, namely photoreceptors, horizontal cells, amacrine cells, bipolar cells, Müller glia cells and retinal ganglion cell, which all develop from the RPCs [90] (compare Figure 2.2 (b)).

2.3.3 Evidence for stochastic fate choices during retina development

In recent years evidence has been increasing that zebrafish retina development is governed by stochastic processes rather than being tightly regulated [92] [89] [93] [8]. For example, experiments have shown that the number of daughter cells arising from each single retinal progenitor cell varies considerably. More specifically, when a single RPC was labelled at 24 hours post fertilisation (hpf) and its clone size (i.e. the number of all cells arising from this one cell) was determined at 72 hpf, a range between 3 and more than 20 cells per clone was found [89]. Furthermore, individual RPCs can give rise to completely different combinations of retinal cell types [89]. While it was thought previously that RPCs pass through a series of competence windows for each individual fate, it has now been suggested that they are

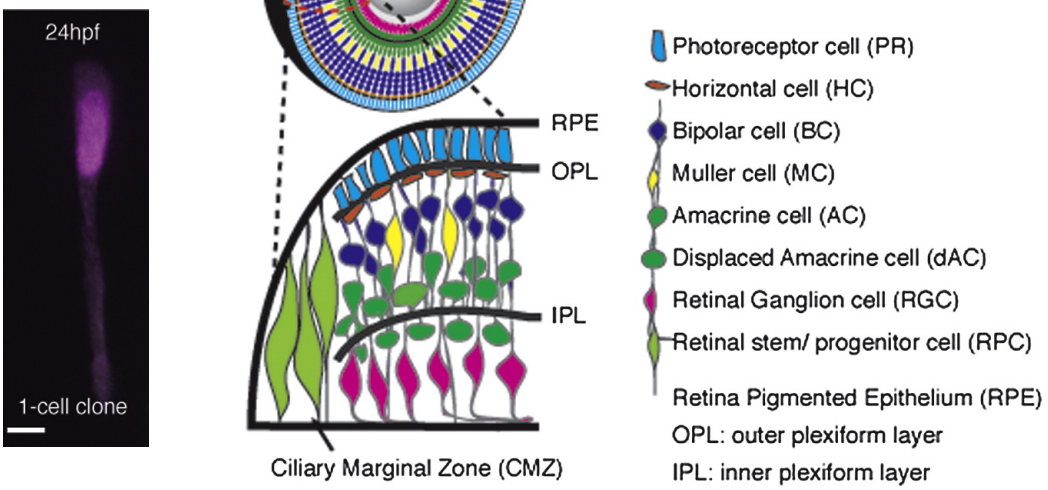

(a) (b)

Figure 2.2 **Development of the zebrafish retina.** The microscopy image in (a) shows a single retinal progenitor cell at 24 hpf. The cell is very slender, bulging around its nucleus. The scale bar is 5 µm. The schematic in (b) depicts the arrangement of the zebrafish retina around the lens as well as the various retinal cell types. During the proliferative phase, the retina consists of retinal progenitor cells (RPCs, light green, bottom left) that span the entire radial dimension of the tissue. RPCs give rise to all the major final cell types of the retina, which (upon differentiation) leave the original monolayer and organise as depicted in the bottm right part of the figure. Both images have been cropped from [89].

competent for multiple fates simultaneously [93]. The clonal size and composition have therefore been proposed to be controlled simply by the probabilities of a cell staying proliferative or becoming neurogenic and the probabilities of certain cell types arising [89] [93] [8].

How these probabilities themselves are set remains to be determined. Potentially, the process of interkinetic nuclear migration might play a crucial role in this.

2.4 Interkinetic nuclear migration

2.4.1 The process of interkinetic nuclear migration

During embryonic development, a remarkable process takes place within the cells of pseudostratified epithelia. While these cells are proliferative, their nuclei move between the apical and basal sides of the tissue in a cell cycle dependent manner (compare Figure 2.3). This movement is termed interkinetic nuclear migration (IKNM). Under normal conditions, the nuclei are located directly at the apical cell surface for each cell division. This phase is also called mitosis or M phase and both the cell itself and the nucleus divide at this point. During the following so-called first gap phase (or G1 phase), the nuclei move away from the apical surface. They remain at more basal but variable positions during the phase of DNA replication (the S phase of the cell cycle). Finally, the nuclei rapidly move back towards the apical tissue surface during the second gap phase (G2 phase) before the next cell division takes place [7] [94] [92] [95] [96] [86].

In early studies, it was assumed that nuclei undergoing IKNM move smoothly along the apicobasal polarity axis of PSE cells (Figure 2.3 left). However, it later emerged that in the zebrafish retina the nuclear movements resemble random walks during G1 and S phases [92] [96] (Figure 2.3 right). This observation explains the large variability of nuclear positions noticed previously [94]. Similar findings have been made for the nuclear positions in the developing mouse retina [94] and brain [97] [86] and recently the randomness of G1 nuclear movements in the mouse retina was shown on the phenomenological level [98].

Interkinetic nuclear migation has first been described by Sauer [7] in 1935. Since then, IKNM has been studied in the retina [92] [89] [8] [94] [96], the brain [86] [87] and the spinal cord [88] as well as in multiple organisms such as the zebrafish [92] [89] [8] [96] [99], chicken [88] [7], pig [7], mouse [94] [86] [87] [100] and ferret [100]. Despite these efforts

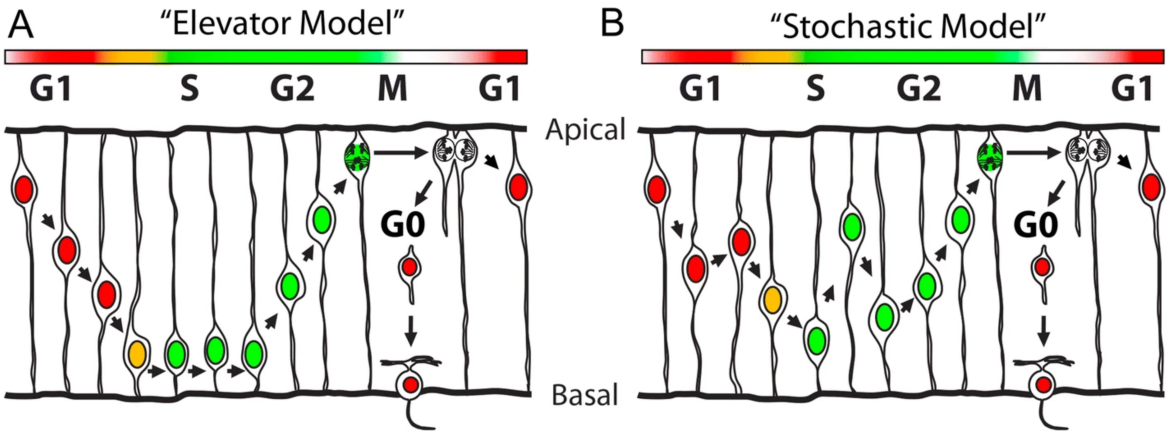

Figure 2.3 **Schematic of interkinetic nuclear migration.** Nuclei of PSE cells move along the apicobasal axis of the cells in line with the cell cycle. Previously, it was assumed that these movements are smooth, taking the nuclei from the apical surface of the cell to the basal surface in G1 and back again in G2. This 'elevator model' is shown on the left. However, it more recently emerged that IKNM resembles a random walk during the majority of the cell cycle, as depicted on the right. Image from [98].

many questions about the mechanisms and precise role of IKNM remain.

2.4.2 IKNM as a possible mechanism to regulate cell differentiation

One aspect of IKNM that has been unveiled in the past is its involvement in tissue maturation of pseudostratified epithelia [101]. Specifically, the positioning of the nucleus at the apical cell surface during mitosis appears to be essential for the proper tissue development in PSE. If a nucleus divides away from the apical surface the integration of the daughter cells into the tissue after cell division is perturbed. Such daughter cells can be come ectopic (i.e. displaced), form clusters and remain proliferative while other RPCs start to differentiate [102] [84]. Those ectopic cells hence impair the correct tissue development [102] [87].

If the apical positioning of a nucleus during cell division is so important for developing PSE, why is it that nuclei move away from the apical tissue surface in the first place? A potential reason is an effect termed crowding [87] [103]. This term refers to the high packing density of nuclei within PSE tissues. In the mouse brain it has been shown that the suppression of basalward nuclear movements after cell division can induce apical overcrowding. The cells then also detach from the apical tissue surface, migrate basally, develop ectopically and interfere with tissue development. Consequently, IKNM might be necessary to regulate the

nuclear packing density within developing PSE [87] [103].

Another possible role of IKNM is connected to the observation that nuclear trajectories resemble random walks during the majority of the cell cycle [92] [96], as described above. It has been suggested that the migrating nuclei sample an apicobasal gradient of the signalling factor Notch [99]. Notch has been associated with diverse roles in development and disease [104]. Among these, Notch and its homolog have been implicated to regulate cell cycle exit in the retina [105] [99]. If the nuclei indeed sampled a Notch gradient, the random walk phenomenology of nuclear trajectories would lead to individual nuclei receiving different amounts of the signal over the course of each individual cell cycle. This possibility has recently been modelled computationally [106]. However, at the protein level the exitence of the suggested Notch gradient could not be confirmed by research in progress in the Norden Lab (Caren Norden, personal communication).

In addition to the mechanisms describe above, several other possible reasons for the necessity of nuclear returns to the apical cell surface before each cell division have been put forward (summarised e.g. in [84]).

2.4.3 How do nuclei move during IKNM?

While the recurrent nuclear returns to the apical cell surface before cell divisions have attracted considerable attention in the past, much less is known about the nuclear movements in the G1 and S phases. Furthermore, although the concept of apical overcrowding has been proposed as a rationale for the existence of IKNM, previous studies have mostly focussed on individual cells without examining interactions between the neighbouring cells or nuclei.

In relation to their proposed functions, the seemingly directed nuclear movements towards the apical cell surface before mitosis have been studied in some detail on the molecular level [84]. In the developing brains of mice and rats both microtubule- and actomyosin-dependent processes are thought to play a role [107] [108]. In contrast, actomyosin alone appears to be sufficient to enable the apicalward nuclear movements in the zebrafish retina [92] [96]. This dissimilarity might be related to the differences in cell size between the two tissues [84]. Furthermore, differences in tissue architecture between the zebrafish brain and retina (having straight and curved geometries, respectively) have been linked to varying mechanisms of nuclear transport [109].

The molecular details of the more random walk-like nuclear movements during the other phases of the cell cycle are known in less in-depth, although similar molecular motors seem to be required [110] [111]. However, different mechanistic hypotheses for the nuclear movement in G1 and S phases exist. These hypotheses link the G1 and S phase nuclear movements to either the apicalward G2 movements of other nuclei [92] or to apical crowding [86] [87].

The first hypothesis - linking G1 and S phase nuclear movements to apicalward G2 movements of other nuclei - is based on the idea of direct energy transfer between the nuclei in a billiard ball-like fashion [92]. This suggestion is supported by the results of pharmacological experiments. In these studies, the DNA replication taking place during S phase was blocked in RPCs. As a result, these cells did not enter G2 and forewent the normally occurring rapid apicalward G2 movements [96] [86]. Surprisingly, the movements of G1 and S phase nuclei were also reduced in velocity [86]. This last result backs the idea that G1 and S phase nuclear movements are normally driven by apicalward moving nuclei colliding with them [92].

The second hypothesis - linking G1 and S phase nuclear movements to apical crowding - is based on experiments observing the adverse effects of overcrowding described above. Here, nuclei are suggested to move away from the apical tissue surface to reduce the local nuclear packing density and thus prevent overcrowding [86] [87]. In this scenario, the nuclei could either be actively transported by cytoskeletal components or be passively pushed away from the apical tissue surface. The implied passive transport mechanism was backed by inserting microbeads into the developing mouse brain tissue. These beads, when inserted close to the apical tissue surface, migrated basalward in a way similar to the nuclear migration inside the cells [86].

Unfortunately, both hypotheses have been lacking direct evidence based on tissue-wide nuclear tracking so far. Previous experiments mostly tracked sparsely labelled nuclei in an unlabelled tissue environment, omitting the possibility of studying cellar or nuclear interactions [92] [94] [96] . However, the above scenarios both explain the apparently random motion of nuclei, existing during the majority of the cell cycle, based on interactions with other nuclei or tissue scale effects (i.e. the apical crowding). Therefore, it has so far not been possible to test these hypotheses based on the data from single nuclei.

Chapter 3

Physics background

In this Chapter, we provide a collection of some physical and numerical concepts which will be needed for our studies of the various aspects of interkinetic nuclear migration presented in the Chapters 5, 6 and 7. Although some of these concepts are discussed here in their historic, physical context, we will make use of their general features when applying them to the biological questions.

First, in Section 3.1 we review Brownian motion as an example of random walk processes and its two mathematical descriptions by way of diffusion equations and Langevin equations. Next, in Section 3.2 we briefly consider some thermodynamic quantities of the lattice gas. Then, in Section 3.3 we introduce the Helfrich elastic model for lipid bilayers and lastly, in Section 3.4 we summarise the Euler-Maruyama method for the numerical solution of stochastic differential equations.

3.1 Brownian motion, diffusion and Langevin equations

3.1.1 Brownian motion and the diffusion equation

In 1827, the botanist Robert Brown observed a phenomenon which now bears his name: Brownian motion [112]. Studying the pollen of plants, he observed small particles collected from these pollen to exhibit striking movements when suspended in water. He further made the same observations when using small particles extracted from diverse types of organic and inorganic matter [113]. Much later, in 1905, Albert Einstein derived a theory for the movements of particles suspended in liquids; although his work stated that for the lack of accurate information, he did not want to make a definite statement of whether or not the

movements described in his study were identical to Brownian motion [114]. Einstein's considerations were based on fundamental principles of thermodynamics and result in the derivation of a diffusion constant as well as in linking his calculations to the differential equation for diffusion [114], previously derived by Adolf Fick in 1855 [115].

Today we know that the random motion of Brownian particles and diffusion are the same phenomenon (compare e.g. [13] [15]). While the trajectories of individual particles are random walks, their distribution, or concentration c, behaves according to the diffusion equation

$$\frac{\partial c(\vec{r},t)}{\partial t} = \nabla \cdot (D \nabla c(\vec{r},t)) \tag{3.1}$$

where $\vec{r}$ denotes position, t time and D is the so-called diffusion constant. This equation holds true for the simple case of (non-interacting) Brownian particles where

$$D_{\text{thermal}} = \frac{k_{\text{B}} T}{6\pi\eta R}, \tag{3.2}$$

with k_{B} being the Boltzmann constant, T the temperature, η the viscosity of the liquid and R the radius of the Brownian particles [114]. However, in general, D can also depend on $\vec{r}$, t or $c(\vec{r},t)$ itself.

3.1.2 Langevin equations

The mathematical description for the random movements of individual Brownian particles was first realised by Paul Langevin in 1908 [116] (compare [117]). To this end, Langevin considered a force balance acting on each particle. Since Brownian motion is driven by random collisions of the particle with surrounding water molecules on a time scale much faster than any other time scale in the system [15] [118], the force administered by the water molecules is stochastic. Thus

$$m\frac{\partial^2 r}{\partial t^2} = -F_{\text{friction}} + \mathscr{F} \tag{3.3}$$

where m is the mass of the particle, F_{friction} is the friction acting on the particle and $\mathscr{F}$ is the stochastic force. Additionally, the Brownian particle can be subject to a force F_{external} that acts on it due to the presence of an external potential, such that

$$m\frac{\partial^2 r}{\partial t^2} = F_{\text{external}} - F_{\text{friction}} + \mathscr{F}. \tag{3.4}$$

In the overdamped limit, neglecting inertia, equation 3.3 becomes

$$0 = -F_{\text{friction}} + \mathscr{F} \tag{3.5}$$

and with $F_{\text{friction}} = \gamma(\partial r/\partial t)$, where γ is the friction coefficient, we obtain

$$\gamma \frac{\partial r}{\partial t} = \mathscr{F}(t). \tag{3.6}$$

Time integration and averaging over realisations of the stochastic force $\mathscr{F}(t)$ yield

$$r(t) = \frac{1}{\gamma}\int_0^t dt' \mathscr{F}(t') \tag{3.7}$$

$$\langle r(t)\rangle = \frac{1}{\gamma}\int_0^t dt' \left\langle \mathscr{F}(t')\right\rangle \tag{3.8}$$

$$\left\langle r^2(t)\right\rangle = \frac{1}{\gamma^2}\int_0^t dt'' \int_0^t dt' \left\langle \mathscr{F}(t')\mathscr{F}(t'')\right\rangle \tag{3.9}$$

3.2 Entropy and chemical potential of the lattice gas

A lattice gas is a system in which space is divided into discrete sites. These sites can either by empty or occupied by a single gas particle. Due to the lattice, particles cannot get closer than the lattice spacing from each other, and thus there is a maximum possible number of particles (or maximum possible concentration) in the system if there is a finite number of lattice sites [14]. The entropy $\mathscr{S}$ of a lattice gas is

$$\mathscr{S} = k_{\text{B}} \ln \Omega = k_{\text{B}} \ln\left(\frac{M!}{N!\,(M-N)!}\right) = k_{\text{B}}\left(\ln M! - \ln N! - \ln (M-N)!\right) \tag{3.10}$$

where k_{B} is the Boltzmann constant, M the number of lattice sites and N the number of particles. Using Stirling's formula $\ln a! \approx a\ln a - a$ we obtain

$$\mathscr{S} \approx k_{\text{B}}\left(M\ln M - N\ln N - (M-N)\ln(M-N)\right). \tag{3.11}$$

The chemical potential can be calculated from the entropy as

$$\mu = -T\frac{\partial S}{\partial N} \tag{3.12}$$

thus

$$\mu = k_{\mathrm{B}}T\left(\ln N - \ln\left(M-N\right)\right). \tag{3.13}$$

We can also rewrite the entropy in Equation 3.11 by introducing the additional term $N\ln V + M\ln V - N\ln V - M\ln V$, where V is the volume, to obtain

$$\begin{aligned}\mathscr{S} &\approx k_{\mathrm{B}}\left(M\ln M - M\ln V - N\ln N + N\ln V - (M-N)\ln\left(M-N\right) + M\ln V - N\ln V\right)\\ &= -k_{\mathrm{B}}\left(N\ln\frac{N}{V} + (M-N)\ln\frac{M-N}{V} - M\ln\frac{M}{V}\right).\end{aligned} \tag{3.14}$$

Then, the chemical potential reads

$$\mu = k_{\mathrm{B}}T\left(\ln\frac{N}{V} - \ln\frac{M-N}{V}\right) \tag{3.15}$$

and with $N/V = c$ and $M/V = c_{\max}$ this becomes

$$\mathscr{S}_{\text{lattice gas}} \propto c\ln c + (c_{\max}-c)\ln\left(c_{\max}-c\right) \tag{3.16}$$

and

$$\mu = k_{\mathrm{B}}T\left(\ln c - \ln\left(c_{\max}-c\right)\right). \tag{3.17}$$

3.3 The Helfrich elastic model for lipid bilayers

As introduced in Chapter 2, biological membranes such as the cell membrane consist of a bilayer of various phospholipids with other enclosed components. This architecture leads to these membranes being only resistant to bending but not to shear, which is relevant for the cell's shape and its deformations [119]. One model to capture these properties is known as the Helfrich elastic model. The following is a summary of work published in [10].

The energy E of a lipid bilayer membrane is given by

$$E = \frac{1}{2}\kappa\int\left(c_1 + c_2 - c_0\right)^2 dA + \Delta p\int dV + \sigma\int dA \tag{3.18}$$

where A is the membrane surface area, V the volume, κ the bending rigidity of the membrane, c_1, c_2 and c_0 are its principal curvatures and spontaneous curvature, Δp is the pressure difference between the inside and outside of the cell and σ the surface tension.

From this expression, using a variational principle, an equilibrium condition can be derived to be

$$\Delta p - 2\sigma H + \kappa(2H + c_0)\left(2H^2 - 2K - c_0 H\right) + 2\kappa\Delta H = 0 \tag{3.19}$$

where

$$H = -\frac{1}{2}(c_1 + c_2) \tag{3.20}$$

is the negative mean curvature and

$$K = c_1 c_2 \tag{3.21}$$

the Gaussian curvature.

Expressions for H and K can also be derived more generally using surface parameterisations and the formalism of differential geometry. In a given parameterisation with the parameters u and v, we can represent a surface in 3-dimensional space as a set of points $\vec{R}(u,v)$. One can introduce

$$\begin{aligned}
\vec{R}_i &= \partial_i \vec{R} \\
\vec{R_{ij}} &= \partial_i \partial_j \vec{R} \\
g_{ij} &= \vec{R}_i \cdot \vec{R}_j \\
g^{ij} &= \left(g_{ij}\right)^{-1} \\
g &= \det\left(g_{ij}\right) \\
\vec{n} &= \frac{\vec{R}_1 \times \vec{R}_2}{\sqrt{g}} \\
L_{ij} &= \vec{R_{ij}} \cdot \vec{n} \\
L &= \det\left(L_{ij}\right)
\end{aligned} \tag{3.22}$$

with $i, j = 1, 2$ and $\partial_1 = \partial_u$ and $\partial_2 = \partial_v$. Using this notation, one obtains

$$H = \frac{1}{2} g^{ij} L_{ij} \tag{3.23}$$

and

$$K = \frac{L}{g} \tag{3.24}$$

as well as an expression for Δ, the Laplace-Beltrami operator, in Equation 3.19 as

$$\Delta = \frac{1}{\sqrt{g}} \partial_i \left(g^{ij} \sqrt{g} \partial_j \right). \tag{3.25}$$

3.4 Numerical solution of stochastic differential equations

In order to solve stochastic differential equations numerically we employ the Euler-Maruyama method [120]. In this method of time discretisation, a stochastic differential equation

$$dX_t = a(X_t)dt + b(X_t)dW_t \tag{3.26}$$

where t is time, X is the true solution of the equation and W_t is a Wiener process is being approximated by a Markov chain Y where

$$Y_{n+1} = Y_n + a(Y_n)\Delta t + b(Y_n)\Delta W_n. \tag{3.27}$$

In this approximation $\Delta t > 0$ is a discrete time step with $n \geq 0$ denoting the n-th step, and ΔW_n are normally distributed random variables with mean zero and variance Δt.

Chapter 4

The data

In this Chapter, we give a brief overview of the experimental data which underlies the work presented throughout the Chapters 5, 6 and 7. This data has been made available in the framework of a collaboration with Afnan Azizi, a PhD student of Prof. William A. Harris (Department of Physiology, Development and Neuroscience, University of Cambridge) at that time. Unless specified otherwise, imaging and post-processing have been performed by Afnan Azizi [11]. We here outline the experimental and data handling procedures to provide an insight into the state of processing in which the data was received and used for the work presented in the following Chapters.

First, in Section 4.1, we provide an overview of the different data sets. Then, in Section 4.2, we illustrate the data acquisition and analysis procedure. Finally, in Section 4.3, we present the state in which the data was received for our subsequent work.

The information provided in Section 4.2, including all the figures, has been published in

Afnan Azizi*, Anne Herrmann*, Yinan Wan, Salvador J. R. P. Buse, Philipp J. Keller, Raymond E. Goldstein, William A. Harris, 'Interkinetic nuclear migration in the zebrafish retina as a diffusive process', *sub judice*, DOI: 10.1101/570606, arXiv: 1903.05414 (2019) [121]

and was written for publication by Afnan Azizi. Minor modifications have been made here to adapt the text to the scope of the dissertation.

Table 4.1 **Overview of data sets.** We use data from five different samples for the work presented throughout this dissertation and here provide an overview of some of the most relevant experimental parameters for these data sets. Specifically, the incubation temperature during imaging, the duration of imaging and the initial number of tracked nuclei, N_0 are shown. More details regarding the experimental procedure are provided in Section 4.2.

Data set description	Incubation T	Imaging time	N_0
Normal condition (main data set)	28.5 °C	400 min	144
Normal condition (repeat data set)	28.5 °C	400 min	71
High temperature data set	32.0 °C	200 min	38
Low temperature data set	25.0 °C	200 min	84
HU-AC treatment data set	28.5 °C	160 min (starting 120 min after drug treatment)	95

4.1 Overview of the data sets

In total, we use 5 different data sets for the work presented in the Chapters 5, 6 and 7. Table 4.1 provides an overview of the different data sets and the relevant conditions. In this table the incubation temperature during imaging, the duration of imaging and the initial number of tracked nuclei, N_0, are shown. More details regarding the experimental procedure are provided in the following Section. Most of the analyses in the Chapters 5, 6 and 7 are based on the main normal condition data set (top entry in 4.1).

4.2 Data acquisition and processing

4.2.1 Animals and Transgenic Lines

All animal work was approved by Local Ethical Review Committee of the University of Cambridge and performed in accordance with a Home Office project license PL80/2198.

All zebrafish were maintained and bred at 26.5 °C. All embryos were incubated at 28.5 °C before imaging sessions. At 10 hours post fertilization (hpf), 0.003% phenylthiourea (PTU) (sigma) was added to the medium to stop pigmentation in the eye.

4.2.2 Generating image sets with high temporal resolution

We imaged fluorescently-labelled nuclei of whole retinas of developing zebrafish at 2 min intervals, an optimal time period given the difficulty to track nuclei accurately over long times and the increased photobleaching with shorter intervals. We compared movies of retinas imaged at 2 min and at 20 s intervals over a period of 2 hours and found that the improvement in temporal resolution made no difference to our analyses. This suggests that it is unlikely that within each 2 min interval there were important intervening movements that might complicate the analysis.

To follow the nuclei of all cells within a portion of the retina we used H2B-GFP transgenic lines with GFP expression exclusively in the nuclei (see Figure 4.1 (a)). In order to achieve the desired temporal resolution without sacrificing image quality, fluorescence bleaching and sample drift must be minimized as much as possible. The retinas of H2B-GFP embryos were imaged using either a single-angle lightsheet microscope (see Figure 4.1 for a schematic) or an upright two-photon scanning microscope. Both of these methods yield images with minimal bleaching compared to other microscopic techniques [122] [123]. However, while the single-angle lightsheet can generate large stacks of images, it is very sensitive to lateral drift due to a small area of high resolution imaging. Therefore, some datasets were produced using two-photon microscopy, which, despite the limitations of scanning time, could produce areas of high resolution images of sufficient size.

4.2.3 Lightsheet microscopy

Images of retinal development for the main dataset were obtained using lightsheet microscopy. This data set was provided by Yinan Wan and Dr. Philipp Keller (Howard Hughes Medical Institute, Janelia Research Campus, Ashburn, VA, USA) [11]. Double transgenic embryos, Tg(bactin2:H2B-GFP::ptf1a:DsRed) were dechorionated (i.e. the surrounding coat was removed) at 24 hpf and screened positive for the fluorescent transgenic markers prior to the imaging experiment. The embryo selected for imaging was then embedded in 0.4% low gelling temperature agarose (Type VII, Sigma-Aldrich) prepared in the imaging buffer (0.3x Daniau's solution with 0.2% tricaine and 0.003% PTU [124]) within an FEP tube with 25 µm thick walls (Zeus), with an eye facing the camera and the illumination light shedding from the ventral side. The tube was held in place by a custom-designed glass capillary (3 mm outer diameter, 20 mm length; Hilgenberg GmbH). The capillary itself was mounted vertically in the imaging specimen chamber filled with the imaging buffer. To

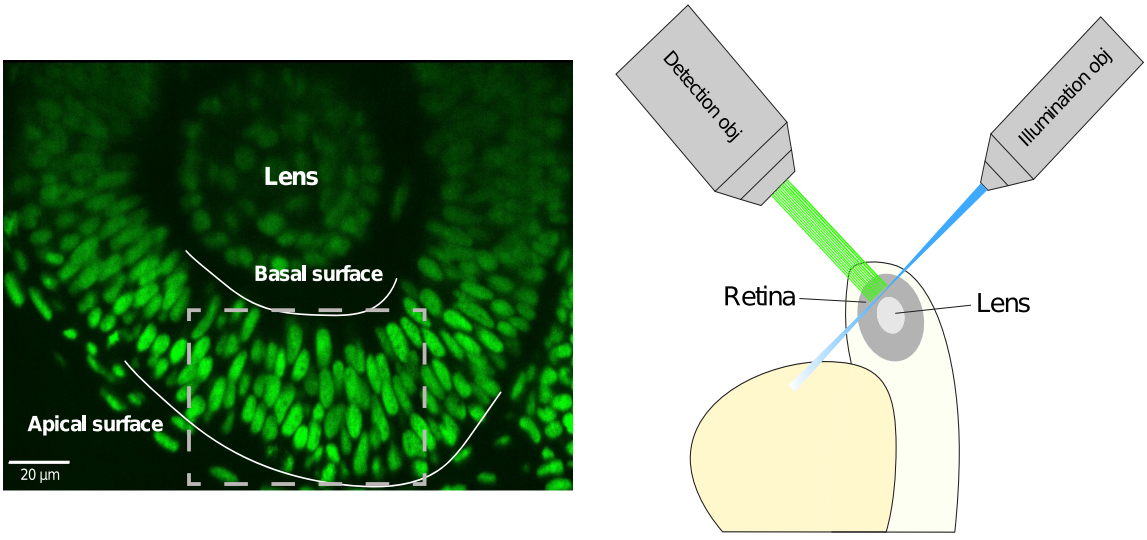

(a) (b)

Figure 4.1 **Imaging of fluorescently labelled nuclei.** (a) A transgenic H2B-GFP embryonic retina imaged using lightsheet microscopy at $\sim$ 30 hpf. The lens, as well as apical and basal surfaces are indicated. The area framed in grey is shown in Figure 4.2. (b) A schematic representation of single-angle lightsheet imaging of the retina. Laser light is focused into a sheet of light by the illumination objective and scans the retina. Fluorescent light is then collected by the perpendicular detection objective.

ensure normal development, a perfusion system was used to pump warm water into the specimen chamber, maintaining a constant temperature of 28.5 °C at the location of the specimen.

Time-lapse recording of retinal development was performed using a SiMView light-sheet microscope [125] with one illumination and one detection arm. Lasers were focused by Nikon 10x/0.3 NA water immersion objectives. Images were acquired with Nikon 40x/0.8 NA water immersion objective and Hamamatsu Ocra Flash 4.0 sCMOS camera. GFP was excited with scanned light sheets using a 488 nm laser, and detected through a 525/50 nm band pass detection filter (Semrock). Image stacks were acquired with confocal slit detection [126] with exposure time of 10 ms per frame, and the sample was moved in 0.812 µm steps along the axial direction. For each time point, two 330 × 330 × 250 μm^3 image stacks with a 40 µm horizontal offset were acquired to ensure the coverage of the entire retina. The images were acquired every 2 min from 30 hpf to 72 hpf. The position of the sample was manually adjusted during imaging to compensate for drift. The two image stacks in the same time point were fused together. An algorithm based on phase correlation was subsequently used to estimate and correct for the sample drift over time. The processing pipeline was implemented with MATLAB (MathWorks) [127].

4.2.4 Two photon microscopy

Images for the repetition dataset and all other conditions were obtained using a TriM Scope II 2-photon microscope (LaVision BioTec). A previously established Tg(H2B-GFP) line, generated by injecting a DNA construct of H2B-GFP driven from the actin promoter [89], was used for all these experiments. Embryos were dechorionated and screened for expression of GFP at 24 hpf. An embryo was then embedded in 0.9% UltraPure low melting point agarose (Invitrogen) prepared in E3 medium containing 0.003% PTU and 0.2% tricaine. The agarose and embryo were placed laterally within a 3D printed half cylinder of transparent ABS plastic, 0.8 mm in diameter, attached to the bottom of a petri dish, such that one eye faced the detection lens of the microscope. The petri dish was then filled with an incubation solution of E3 medium, PTU, and tricaine in the same concentrations as above. For the experiment involving cell cycle arrest, hydroxyurea and aphidicolin (Abcam) were added to the incubation solution right before imaging, to a final concentration of 20 mM and 150 µM, respectively. The imaging chamber was maintained at a temperature of 25 °C, 28.5 °C, or 32 °C, as required, using a precision air heater (The Cube, Life Imaging Services).

Green fluorescence was excited using an Insight DeepSee laser (Spectra-Physics) at 927 nm. The emission of the fluorophore was detected through an Olympus 25x/1.05 NA water immersion objective, and all the signal within the visible spectrum was recorded by a sensitive GaAsP detector. Image stacks with step size of 1 µm were acquired with exposure time of 1.35 ms per line averaged over two scans. The images were recorded every 2 min for 10-15 hours starting at 26-28 hpf. The same post processing procedure for data compression and drift correction was used on these raw images as on those from lightsheet imaging.

4.2.5 Data processing and analysis of nuclear tracks

Both lightsheet and two-photon microscopes produced images of at least half the retina with a depth of at least 50 µm over several hours in 2 min intervals. The images were processed using a suite of algorithms [128] to compress them to a lossless format, Keller Lab Block (KLB), correct global and local drift, and normalize signal intensities for further processing. Automated segmentation and tracking of the nuclei were carried out through a previously published computational pipeline that takes advantage of watershed techniques and persistence-based clustering (PBC) agglomeration to create segments and Gaussian mixture models with Bayesian inference to generate tracks of nuclei through time [129] [128]. Two main parameters greatly affect tracking results, overall background threshold and PBC agglomeration threshold. To obtain best automated tracking results, ground truth tracks were created for a section of the retina over 120 min and were compared to tracks generated over a range of these two parameters. The best combination of the two parameters was chosen as the one with highest tracking fidelity and lowest amount of oversegmentation over that interval.

The most optimal combination of parameters yielded an average linkage accuracy, from each time point to the next, of approximately 65%. Hence, extensive manual curation and correction of tracks were required. Tracking by Gaussian mixture models (TGMM) software generates tracks that can be viewed and modified using the Massive Multi-view Tracker (MaMuT) plugin of the Fiji software [130] [131]. A region of the retina with the best fluorescence signal was chosen and all tracks within that region were examined and any errors were corrected. The tracks consist of sequentially connected sets of 3D coordinates representing the centres of each nucleus (Figure 4.2 (a)), with which their movement across the tissue can be mapped over time. For example, Figure 4.2 (b) shows IKNM of a single nucleus tracked from its birth, at the apical surface of the retina, to its eventual division into two daughter cells.

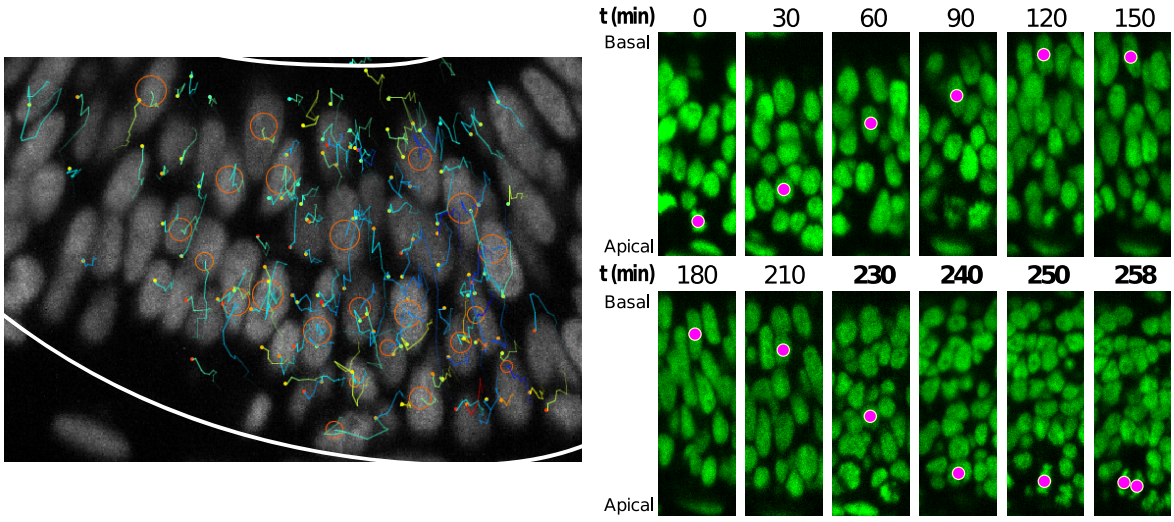

(a) (b)

Figure 4.2 **Tracking fluorescently labelled nuclei.** (a) Track visualisation and curation using the MaMuT plugin of Fiji (image enlarged from Figure 4.1 (a)). All tracks within a region of the retina are curated and visualised. Circles and dots represent centres of nuclei, and lines show their immediate (10 previous steps) track. (b) The position of a single nucleus within the retinal tissue from its birth to its eventual division. The magenta dot indicates the nucleus tracked at various time points during its cell cycle. The last 4 panels are at shorter time intervals to highlight the rapid movement of the nucleus prior to mitosis.

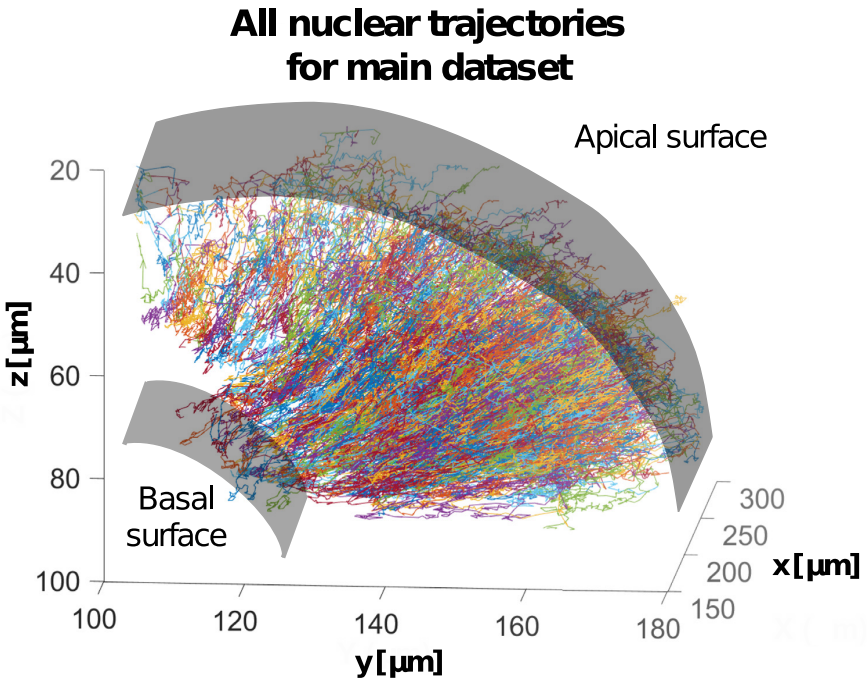

Figure 4.3 **All nuclear tracks.** Extracted trajectories of nuclei in 3 dimensions. All curated tracks of the main dataset over 400 minutes in the region shown in Figure 4.2 are presented.

This process yielded tracks for hundreds of nuclei, across various samples, over time intervals of at least 200 min. We used custom-written MATLAB scripts to analyze these tracks. The aggregated tracks of the main dataset, in Cartesian coordinates, for all tracked lineages is shown in Figure 4.1. Single tracks for any given time interval can be extracted and analyzed from this collection. In order to transform the Cartesian coordinates of the tracks into an apicobasal coordinate system, we drew contour curves at the apical surface of the retina (e.g. see Figure 4.1 (a)) separating RPC nuclei from the elongated nuclei of the pigmented epithelium. We then calculated curves of best fit (second degree polynomials) in both the xy- and yz-planes. Assuming that the apical cortex is perpendicular to the apicobasal axis of each cell, displacement vectors of the nuclei at each time point can be separated into apicobasal and lateral components. Since, in IKNM, the apicobasal motion is that of interest, we used this component for our analysis of nuclear velocity (see Chapter 5).

4.3 State of processing upon receipt of data sets

As a result of the extensive data analysis described above, we obtain hundreds of nuclear tracks. For the work presented in the Chapters 5, 6 and 7 this tracking data was made

Table 4.2 **Tracking data example.** Nuclear tracking data as obtained for the work presented in Chapters 5, 6 and 7. Each nuclear position is asigned a unique identifier (first column). The nuclear positions are provided in Carthesian coordinates (second to fourth column). In addition, the parent identifier, i.e. the identifier of the nucleus' position at the previous time point, is provided (fifth column). In this example, the nuclear position with the identifier 1 is the position at the beginning of the experiment, thus it does not possess a parent identifier. The parent identifier of the nuclear position 2 is 1, indicating that 2 is the same nucleus as 1 but one time step later. In this way, full tracks can be reconstructed. The entries with the identifiers 4 and 5 both possess the parent identifier 3. This means the nucleus from position 3 divided during this time step, giving rise to both nuclei at the positions 4 and 5.

Identifier	x	y	z	parent identifier
1	x_1	y_1	z_1	-
2	x_2	y_2	z_2	1
3	x_3	y_3	z_3	2
4	x_4	y_4	z_4	3
5	x_5	y_5	z_5	3

available as spreadsheets in MATLAB [127]. These spreadsheets contain lists of (drift corrected) nuclear positions in Carthesian coordinates. Each nuclear position possesses a unique identifier. Additionally, the identifier of each nucleus' previous position is provided, allowing the reconstruction of the whole trajectory. If a nucleus divides, resulting in the existence of two new daughter nuclei in the next time step, the two daughter nuclei's positions obtain individual identifiers but are assigned the same parent identifier. In this way, cell and nuclear divisions can be retraced as well. An example of such tracking data is provided in Table 4.2. Further to the information on identifiers and nuclear positions, the data sets contain information on parameters such as (image) quality, not taken into account here.

In addition to the tracking data, lists of distances of the nuclei from the apical tissue surface were also provided. These apical distances are obtained from the tracking data as described above in Section 4.2 and again provided as spreadsheets in MATLAB. In this case, data is sorted by experimental time point and for each time point the set of all nuclear distances from the apical tissue surface is listed.

a	radial coordinate of apical tissue surface
b	radial coordinate of basal tissue surface
c, c_{exp}	nuclear concentration, experimental values for c
c_{max}	maximum nuclear concentration
D	diffusion constant
D^*, D^*_{lin}, D^*_{nonlin}	optimal D-value, D^* linear model, D^* nonlinear model
$\tilde{D}$	effective diffusion constant
f_0	variable in calculation, see Appendix 5.B
g_0	variable in calculation, see Appendix 5.B
H_i	eigenfunctions of radial diffusion problem
h_i	prefactors of eigenmodes
i	index of eigenmodes
L	tissue thickness
l_n	distance of a single nucleus from the apical tissue surface
m	index of data points after binning
N, N_0, N_{bin}	number of nuclei, initial N of tracked nuclei, N in a given bin
n	index denoting a single nucleus
$p_{n,\mathrm{bin}}$	probability of finding a given nucleus in a given bin
r	radial coordinate of the tissue
r_{bin}, $r_{\mathrm{bin,\ inner}}$, $r_{\mathrm{bin,\ outer}}$	radial position of a given bin and its outer and inner values
r_n	radial coordinate of a single nucleus
S	apical tissue surface area
$\mathscr{S}$	entropy
s	rescaled (experimental) time
T	temperature
$\mathscr{T}$	decay times of eigenmodes
T_P	average cell cycle
t	(experimental) time
V,V_{total}	volume, total volume in which nuclei were tracked
α_i	variable in calculation, see Appendix 5.B
λ_i	eigenvalues
ν	number of degrees of freedom for fit
ξ	rescaled radial coordinate of the tissue
ξ_{bin}, ξ_m	rescaled position of bin (general) and specific data point
ρ	b/a
σ	variable in calculation, see Appendix 5.B
σ_{D^*}	standard deviation of optimal D-value
σ_m	effective total uncertainty of data point for fitting
$\sigma_{x,\mathrm{bin}}$, $\sigma_{x,m}$	positional uncertainty of bin count, rescaled $\sigma_{x,\mathrm{bin}}$ for data point
$\sigma_{y,\mathrm{bin}}$, $\sigma_{y,m}$	standard deviation of bin count, rescaled $\sigma_{y,\mathrm{bin}}$ for data point
$\sigma_{y,\mathrm{indirect},m}$	contribution of $\sigma_{x,m}$ to σ_m
τ	$T_P/\ln 2$
Ω	solid angle

Chapter 5

From one to many - tissue scale IKNM

The results presented in this Chapter have been published in

Afnan Azizi*, Anne Herrmann*, Yinan Wan, Salvador J. R. P. Buse, Philipp J. Keller, Raymond E. Goldstein, William A. Harris, 'Interkinetic nuclear migration in the zebrafish retina as a diffusive process', *sub judice*, DOI: 10.1101/570606, arXiv: 1903.05414 (2019) [121].

William A. Harris (Department of Physiology, Development and Neuroscience, University of Cambridge) first suggested to model nuclear movements in IKNM based on diffusion. The analysis of nuclear trajectories presented in Subsections 5.2.3 and 5.2.4 have been performed by Afnan Azizi (Department of Physiology, Development and Neuroscience, University of Cambridge at that time). Afnan Azizi also provided further experimental input parameters (the total retinal volumes V_{total}, the cell cycle times T_P and the measurements upon which the estimation of the nuclear principal semi-axes is based) and prepared the graphs in Figures 5.2, 5.3 and 5.4 (c). The text in Subsections 5.2.3, 5.2.4 and 5.2.5 as well as parts of the Discussion in this Chapter are based on parts of the publication that had been written collaboratively between Afnan Azizi and myself. However, this text has been fully revised for the scope of this dissertation. The remaining parts of the text in this Chapter constitute my own contribution to the publication. Oliver Y. Feng (Department of Pure Mathematics and Mathematical Statistics, University of Cambridge) provided advice on how to calculate the expectation value and variance of the bin count when binning nuclei. Timothy J. Pedley (Department of Applied Mathematics and Theoretical Physics, University of Cambridge) encouraged us to transform a previous, 1-dimensional version of the model in Section 5.3 into the full 3-dimensional model presented here. Michael E. Cates (Department of Applied Mathematics and Theoretical Physics, University of Cambridge) and Raymond E. Goldstein suggested to

base the nonlinear version of the model in Section 5.4 on incorporating the entropy of the lattice gas into the diffusion equation. Salvatore Torquato (Department of Chemistry, the Princeton Institute for the Science and Technology of Materials, and the Princeton Center for Theoretical Science, Princeton University, USA) provided the maximum possible packing density for aligned ellipsoids, necessary to calculate the maximum nuclear concentration $c_{\max}$. Except for collaborations with my Supervisor Raymond E. Goldstein, who specifically provided very valuable input for the calculations of the apical boundary condition and the full solution of the linear diffusion model shown in the Appendices, recommended to use the minimum-χ^2 method for fitting and suggested to calculate the decay times of the different modes of the linear model, the remainder of the work presented in this Chapter is my own.

5.1 Introduction

Our first aim in this dissertation is to obtain a quantitative description of IKNM on the tissue level.

Based on the experimental data, in Section 5.2 we start by assessing the hypotheses on how nuclear movements might be driven that we presented in Chapter 2. We find no evidence supporting the first hypothesis but our data is consistent with the apical crowding scenario. Motivated by this result, in Section 5.3 we define a simple model for IKNM, which consists of the diffusion equation to describe the distribution of nuclei in the retinal tissue and appropriate boundary conditions. We then fit this model to the experimental data. As it turns out, this model fits the data well for early experimental time points but fails to provide a good prediction of the data at later experimental times, even when we only take data from these late times into account for the fit. Therefore, in Section 5.4, we explore the potential of a nonlinear diffusion equation to describe the experimental data more accurately. By fitting this new model to the data, we show that it reproduces the experimentally observed distribution of nuclei very well for the whole duration of the experiments. Furthermore, the nonlinear model enables us to fit experimental data from many time points simultaneously. Finally, in Section 5.5, we apply the nonlinear model to experimental data obtained under varied conditions. We find that changing the incubation temperature during the experiments has effects on IKNM that are independent of the well-known temperature-dependent changes in cell cycle time, hinting at potential microscopic mechanisms for IKNM. We will further explore these microscopic mechanisms in Chapter 6 where we develop a Langevin-type description for the

individual nuclear movements based on the models presented in the following.

5.2 IKNM tissue level variability and driving mechanism

In this Section, we use the biological data from Chapter 4 to examine the properties of IKNM on the tissue level.

First, in Subsection 5.2.1, we set up the coordinate system that we use for most of the work presented in this Chapter. Then, in Subsection 5.2.2, we describe how we obtain nuclear concentration profiles as a function of time from the data presented in Chapter 4. In the following, when speaking of nuclear concentration, we will always mean number concentration (or number density), i.e.

$$c = \frac{N}{V} \tag{5.1}$$

where c is the nuclear (number) concentration and N is the number of nuclei in the volume V. The nuclear concentration profiles are used throughout Chapters 5 and 6, with the exception of Subsections 5.2.3 and 5.2.4. For the results presented in these two Subsections, the data is used directly in the state of processing presented in Chapter 4. Subsection 5.2.3 contains an analysis of various properties of the nuclear trajectories in IKNM. Most importantly, this Subsection provides an account of the variability of IKNM throughout the majority of the cell cycle. Similar analyses have been carried out before [94] [92] [96] [86] but so far relied on data obtained from single nuclei in unlabelled tissues. In contrast, the results presented here are based on tracking all nuclei in a section of the retinal tissue simultaneously and thus these results provide an account of the variability of IKNM on the tissue level. Finally, the Subsections 5.2.4 and 5.2.5 scrutinise the two hypotheses previously put forward on how IKNM might be driven (compare Chapter 2) [92] [96] [86] [87]. We find no evidence for direct interactions between the nuclei, but the experimental data is consistent with the apical crowding scenario.

5.2.1 Considering the geometry of the retina

In order to calculate the nuclear concentration profile, which is needed throughout most of this Chapter and Chapter 6, we first set out to define a coordinate system that is different from the one used for processing the experimental data in Chapter 4. In the experiments,

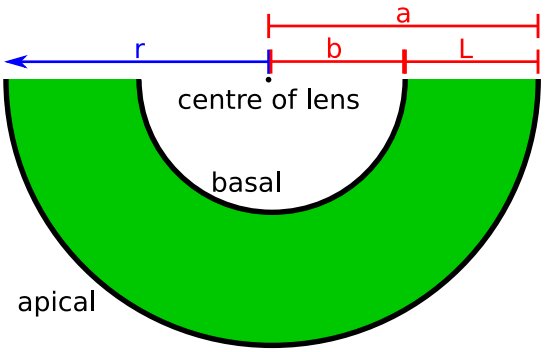

Figure 5.1 **Definition of coordinate system.** For the concentration profile needed in the Chapters 5 and 6 it proves advantageous to define the coordinate system differently than during data processing. While during the data processing the distance of nuclei from the apical tissue surface was measured, we here define a spherical polar coordinate system. In this coordinate system the is origin located at the centre of the lens and the basal and apical tissue surfaces are positioned at $r = b$ and $r = a$, respectively. L is the tissue thickness.

the nuclear position was defined as the distance from the apical tissue surface and the experimental data is also used in this way for the analyses presented in Subsections 5.2.3 and 5.2.4. However, for the mathematical models presented in Sections 5.3 and 5.4, a different choice of coordinate system appears advantageous. In choosing the coordinate system we pay special attention to the geometry of the retinal tissue. The retina can be approximated as one half of a hollow sphere (or spherical shell) around the lens, and thus we employ spherical polar coordinates with the origin of the coordinate system at the centre of the lens. In this system, the basal tissue surface is consequently located at $r = b$ and the apical surface at $r = a$ (see Figure 5.1).

Now, the radial coordinates r_n of nuclei are calculated by subtracting l_n from a, wherein l_n is the distance between the centre of a given nucleus n and the apical surface, as obtained during data processing (compare Chapter 4). We estimate a total uncertainty of $\Delta r_n = \pm 3$ µm for each single distance r_n. This value is a result of experimental uncertainties in detecting the centre of the nucleus and in establishing the exact position of the apical surface.

5.2.2 The nuclear concentration profile

To transform the data on nuclear positions from above into a concentration profile, we bin the nuclei based on their radial coordinates and thus obtain estimates for the number of nuclei N as a function of r. Because each nuclear position has an uncertainty Δr, binning the data leads to an uncertainty in the bin count. In order to calculate this uncertainty,

we consider the probability distribution of a nucleus' position. In the simplest case, this probability is uniform within the width of the positional uncertainty and zero elsewhere. Then, the probability, $p_{n,\mathrm{bin}}$, of finding a given nucleus n within a given bin, is proportional to the size of the overlap of probability distribution and bin. It follows that the expectation value for the number of nuclei within a bin is given as $\mathbb{E}[N_{\mathrm{bin}}] = \sum_n p_{n,\mathrm{bin}}$. Correspondingly, $\mathrm{Var}(N_{\mathrm{bin}}) = \sum_n p_{n,\mathrm{bin}}(1 - p_{n,\mathrm{bin}})$ is the variance of the number of nuclei within this bin. Thus, the standard deviation of the bin count is $\sigma_{y,\mathrm{bin}} = \sqrt{\mathrm{Var}(N_{\mathrm{bin}})}$.

The nuclear distribution profile $N(r,t)$ is not expected to be uniform or linear, therefore the expectation value $\mathbb{E}[N_{\mathrm{bin}}]$ does not necessarily correspond to the number of nuclei at the centre of the bin. However, the position where $N(r) = \mathbb{E}[N_{\mathrm{bin}}]$ is not known *a priori*. Therefore, we nevertheless locate $\mathbb{E}[N_{\mathrm{bin}}]$ at the centre of the bin but include a positional uncertainty. Here we assume this uncertainty to be the square-root of the bin size Δr_{bin}, i.e. $\sigma_{x,\mathrm{bin}} = \sqrt{\Delta r_{\mathrm{bin}}}$.

Furthermore, we need to obtain the total retinal volume V_{total} within which nuclei tracking took place, and $V(r)$. V_{total} can be estimated directly from the microscopy images. To this end, we outline the area of observation in each image slice using the Fiji software [132] and multiply this area with the distance between subsequent images in the stack. Because we assume the retinal tissue to be one half of a spherical shell around the nucleus, the region within which nuclei were tracked is simply a sector of this shell. Knowing the apical and basal tissue radii, $r = a$ and $r = b$, one can thus calculate the solid angle Ω of this region as $\Omega = 3V_{\mathrm{total}}/(a^3 - b^3)$. This gives the volume of each bin as $V_{\mathrm{bin}} = \Omega\left(r^3_{\mathrm{bin,outer}} - r^3_{\mathrm{bin,inner}}\right)/3$, where $r_{\mathrm{bin,outer}}$ and $r_{\mathrm{bin,inner}}$ denote the outer and inner radii of a bin, respectively.

When calculating the volume of each bin, we do not consider any uncertainties thereof. The reason is that each bin volume was simply calculated as a fraction of the total volume V_{total}. Thus, for subsequently calculating the concentration profile $c(r,t)$, V_{total} is merely a scaling factor. Hence, uncertainties in V_{total} are only relevant for the absolute value of $c(r,t)$ but not for its functional shape.

Finally, $c(r,t)$ is simply calculated from the distribution of nuclei $N(r,t)$ and the bin volumes.

5.2.3 IKNM - a random movement during the majority of the cell cycle

Based on our experimental data we first perform an extensive analysis of the dynamical properties of moving nuclei in IKNM. For example, we extract the distribution of cell cycle lengths and that of the maximum distance a nucleus moved away from the apical surface over the course of the entire cell cycle (see Figure 5.2 (a) for the latter). In total, we analyse 16 different features of the nuclear trajectories (compare [11]). Most importantly, we closely examine the velocity (defined as displacement along the apicobasal axis between two consecutive microscopy images divided by the time between these images, i.e. by 2 min) and position as functions of cell cycle for all nuclei that were tracked for a full cell cycle (see Figure 5.2 (b) and (c)). Although similar properties of IKNM have been analysed before [94] [92] [96], previous studies have only considered sparsely labelled nuclei in otherwise unlabelled environments. Therefore, the data analysis presented here provides an important account of the variability of IKNM on the tissue level.

As Figures 5.2 (b) and (c) show, both nuclear velocity and position are highly variable during the majority of the cell cycle. The only exceptions are brief periods directly after cell division in early G1, when all nuclei move towards the basal surface, and in G2, when nuclei move towards the apical surface for the following cell division (arrows in Figure 5.2 (b)). The brief period of basalward movement right after cell division has previously been observed by Shinoda et al. [100] and Barrasso et al. [98] while the apicalward movement in G2 is well studied [7] [94] [108] [107] [92] [95] [86] [96] [84]. However, the apicalward movements of nuclei during G2 only account for approx. 8% of the cell cycle [96] while the period of initial basalward movement is even shorter (compare Figure 5.2 (b)). Therefore, in the following, we focus on the remaining, major part of the cell cycle, which so far has been studied in less detail.

It is evident from the data in Figure 5.2 (b), that during the majority of the cell cycle the mean velocity of IKNM nuclei is close to zero, although the individual nuclei are clearly moving. Such a velocity distribution for a group of particles indicates the possibility that individual constituents might move in a random fashion. Random motion also leads to a spreading of the spatial distribution of individual particles, similar to the spreading of nuclear positions shown in Figure 5.2 (c). Indeed previous publications have suggested that the movement of nuclei during IKNM might be stochastic [92] [96]. However, again, all previous studies were based on data from individual nuclei in unlabelled environments. This hitherto excluded the possibility of examining any collective effects, such as potential interactions between nuclei or changes in concentration profiles. But being able to analyse these collective

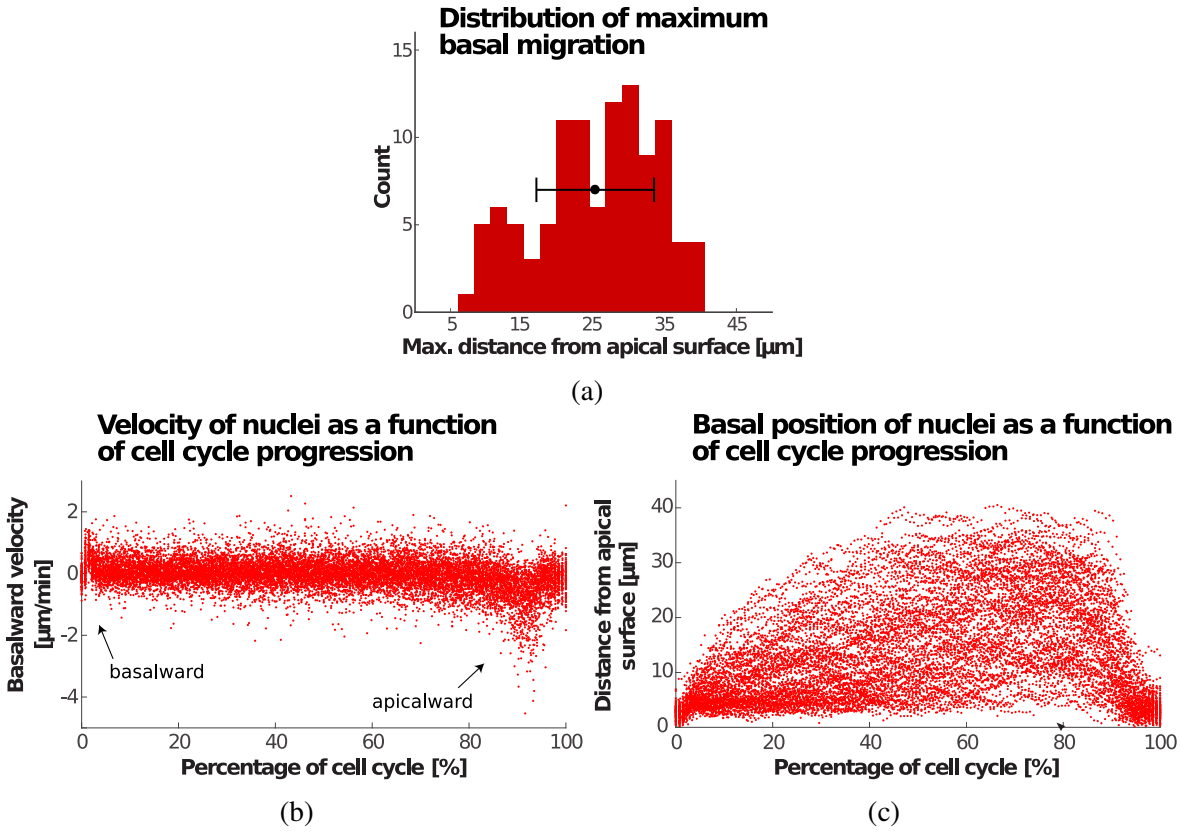

(a)

(b)

(c)

Figure 5.2 **Variability of IKNM.** We extract the distributions of a total of 16 different features from the nuclear trajectories [11]. As an example, the distribution of the maximum distance each nucleus migrated away from the apical tissue surface is shown in (a). Furthermore, (b) shows the nuclear velocity (defined as displacement along the apicobasal axis between two consecutive microscopy images divided by the time between these images, i.e. by 2 min) and (c) shows the nuclear position along the apicobasal axis. Both properties are depicted as a function of cell cycle progression in % of the cell cycle. All three graphs take all nuclei that were tracked for the full cell cycle into account.

effects is necessary e.g. for making statements about possible driving mechanisms of the suspected random nuclear motion in IKNM. Furthermore, previous studies did not take major geometric constraints based on the shape and architecture of the retinal progenitor cells and the retinal tissue into account. For example, the observed basalward motion of nuclei directly after cell division (arrow in Figure 5.2 (b)) might be a consequence of the presence of the apical tissue boundary, rather than a separate phase of movement as implied by some authors [92] [96] [87].

In the following, we analyse the apparent randomness of IKNM movements in more detail than previously possible, taking into account possible collective effects between the nuclei.

5.2.4 No indication of direct energy transfer between nuclei

Based on our experimentally obtained nuclear tracks, we are able to directly test the two previously proposed hypotheses on how nuclei are driven during most of IKNM (compare Chapter 2).

First, we search the experimental tracks for evidence of direct interactions between rapidly apicalward moving nuclei and their neighbours. To this end, we test for correlations in speed and direction of movement between the nuclei. For these tests, we choose all neighbour nuclei with centres of mass (i.e. the tracked points) within a cylindrical volume of height and base diameter twice the length of long and short axis, respectively, of an average nucleus. As Figure 5.3 shows, there is no correlation between the speed of apicalward moving nuclei and the average speed of their neighbours (correlation coefficient $R^2 = 0.001$). We thus further sub-categorise the neighbouring nuclei by their position in relation to the nucleus of interest (further apical or further basal), their direction of movement (apicalward or basalward) and whether they are moving in the same direction as the nucleus of interest or not. None of the resulting eight cases shows a correlation between the speed of the apicalward moving nuclei and the average speed of their neighbours. Even when considering the movements of neighbouring nuclei one time point (2 min) before or one time point after the movements of the nucleus of interest, no correlations in speed can be found. These results suggest that no (or only little) direct interaction between neighbouring nuclei takes place. Therefore, they speak against the first of the two described hypotheses for how nuclear movements during the majority of the cell cycle arise in IKNM.

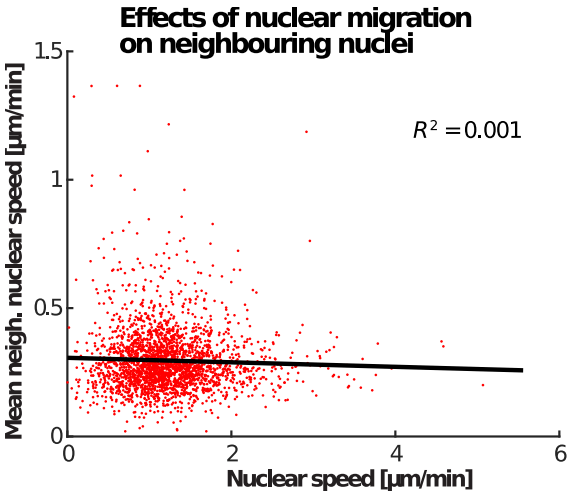

Figure 5.3 **Correlation between nuclear speeds.** In order to determine whether there might be direct interactions between the nuclei we search for correlations between the speed of rapidly apicalward moving nuclei and the speed of their neighbours. Here, we take neighbouring nuclei with centres of mass within a cylindrical volume of height and base diameter twice the length of the long and short axis, respectively, of an average nucleus into account. As the graph shows, there is no correlation between the speed of the rapidly apicalwards moving nuclei and the speed of their neighbours, $R^2 = 0.001$.

5.2.5 Apical crowding influences IKNM

Next, we consider how apical crowding might result in the experimentally observed properties of IKNM. This can be understood qualitatively by comparing IKNM to a diffusion process. As introduced in Chapter 3, in diffusion each individual particle performs a random walk which effectively leads to an average movement of particles from areas of high to areas of low particle concentration. Similarly, during the development of neural tissues, a nuclear concentration gradient might be created because nuclei divide exclusively at the apical tissue surface [87] [103]. If nuclei independently performed random walks during the majority of the cell cycle (like Brownian particles), this presumed nuclear concentration gradient would result in a net movement of nuclei away from the area of strongest crowding, i.e. away from the apical side of the neuroepithelium. The presence of the apical tissue boundary and possible interactions between the nuclei might additionally enhance this effect. Indeed, in IKNM we find that nuclear trajectories strongly resemble random walks (compare Figure 5.2 (b) and also [92]). Furthermore, nuclei on average move away from the apical surface after cell divisions until they have spread across the whole apicobasal dimension of the retinal tissue (compare Figure 5.2 (c)). However, the question remains whether, in fact, such a presumed nuclear concentration gradient exists.

The $c(r,t=0)$ calculated in Subsection 5.2.2 immediately shows that indeed a nuclear concentration gradient exists in the retinal tissue (see Figure 5.4 (a) data in black, where $\xi = r/a$). The nuclei are densest close to the apical tissue surface, even though the tissue here has more volume for the nuclei to distribute in than the tissue close to the basal surface. Furthermore, comparing $c(r,t=0)$ with concentration profiles from later time points (see Figure 5.4 (a) data in red) indicates that the nuclear concentration gradient even builds up over time. This is presumably due to G2 nuclei returning to the apical tissue surface and dividing there, leading to a continuous addition of nuclei near $r = a$.

The existence and time evolution of the observed nuclear concentration gradient so far support the hypothesis that IKNM could be driven by apical crowding and might be described by comparison to diffusion. Now, to test how far this analogy goes, we ask what would happen to the concentration gradient if we blocked the cell cycle in S phase, which inhibits both the apicalward movement of the nuclei in G2 and mitosis at the apical surface. If the comparison to diffusion was valid, we would expect the blockage to abolish the build-up and maintenance of the concentration gradient. We, therefore, compare the normally evolving distribution of nuclei in a control retina with a distribution obtained from a retina where the cell cycle was arrested in S phase using a combination of hydroxyurea (HU) and aphidicolin (AC) [92] [133]. For the chemically treated retina we retrieve the number distribution of nuclei in a three dimensional section of the tissue containing approximately 100 nuclei, at equal time intervals, starting at 120 min after drug treatment. The delay ensures that almost all cell divisions, from nuclei that had already completed the S phase at the time of treatment, have taken place. As expected from the comparison to diffusion, over the course of 160 min, the mean of the nuclear distribution moves further towards the basal surface in the treated retina, and the concentration difference between the apical and basal surfaces diminishes (see Figure 5.4 (b) and (c)). In contrast, in the control retina the mean of the nuclear distribution moves towards the apical surface over the same period of time (see Figure 5.4 (a) and (c)) as the gradient continues to build up. These results support the suitability of a diffusion model to describe the time evolution of the nuclear distribution during IKNM.

We conclude that for the cells in the G1 and S phases (which account for more than 90% of the cell cycle time in our system), IKNM has, at least on a phenomenological level, the main features of a diffusive process. Therefore, we continue to use the correspondence between the phenomenologies of IKNM and diffusion and in the following make use of the well established mathematical framework of the latter to describe tissue level IKNM quantitatively.

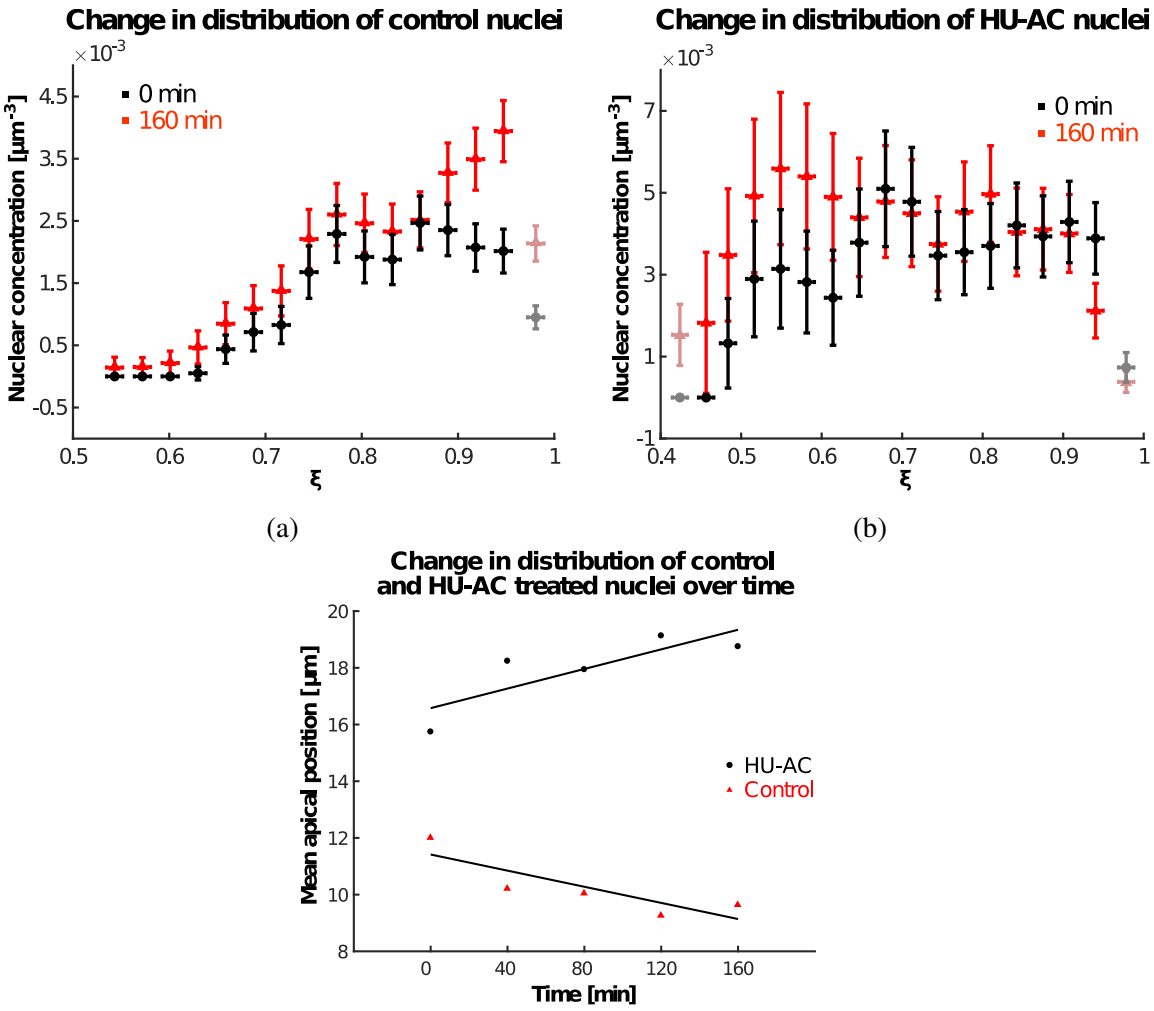

Figure 5.4 **Apical crowding and its role in driving IKNM.** In order to understand whether apical crowding might be relevant in driving nuclear movements in interkinetic nuclear migration, we examine the nuclear concentration across the retinal tissue and over time. The nuclear concentration profiles at $t = 0$ min (black) and $t = 160$ min (red) of the main data set are shown in (a). Evidently, a concentration gradient exists in this sample and builds up over time. The nuclear concentration profiles at $t = 0$ min (black) and $t = 160$ min (red) of a sample treated with hydroxyurea (HU) and aphidicolin (AC) are shown in (b). In this sample, the concentration profile flattens out over time. This flattening of the concentration profile in the HU-AC treated case is apparent from the data shown in (c). Here, the mean apical position of all nuclei in the tissues has been plotted for both samples over time (normal sample in red, HU-AC treated sample in black). While the mean position of all nuclei becomes more apical over time in the normal sample (indicating the build-up of the nuclear concentration gradient) the mean position of all nuclei becomes more basal over time in the HU-AC treated sample (indicating the flattening of the nuclear concentration gradient).

5.3 A diffusion model for IKNM

To investigate whether a diffusion model would also provide a useful quantitative description for IKNM, we formalise the process of IKNM in mathematical terms. Our ultimate aim is to derive a model that can predict the time evolution of the distribution of nuclei across the retinal tissue from an experimentally known initial condition (i.e. the distribution of nuclei at the start of an experiment) and an experimentally known average cell cycle time only. To this end, as introduced in Section 5.2, we describe the distribution of nuclei as a nuclear concentration profile across the retina. Furthermore, we assume two points as given. Firstly, we know that nuclei exclusively divide close to the apical tissue boundary, leading to an addition of nuclei at this boundary only. Secondly, it is well known that in a proliferative system with a constant average cell cycle time and no cell deaths, the number of cells grows exponentially (compare e.g. [134]). We briefly check that this second point indeed holds true for the number of cells in the growing zebrafish retina in Subsection 5.3.1 but use it as an input for our model thereafter. Finally, in this whole Section, we further assume that the time evolution of the distribution of nuclei can be described using the standard diffusion equation as introduced in Chapter 3. Then the only unknown in our model is the diffusion constant, which here describes the effective mobility of the nuclei. Fitting this model to our experimental data provides us with an estimate of this diffusion constant and, more importantly, with an understanding whether the model so specified represents the time evolution of the nuclear distribution in the zebrafish retinal tissue well. If this is the case we conclude that a simple diffusion model is suitable to describe the nuclear distribution during IKNM and thus fulfils our aim; else we will seek to modify the model hereafter. In Subsection 5.3.1 we derive the basic equations of our model, consisting of the diffusion equation in radial coordinates and the appropriate boundary conditions for the case of IKNM. Then, in Subsection 5.3.3 we present the analytical solution thereof. The prefactors in this solution can be calculated using the initial distribution of nuclei in the experiment (see Subsection 5.3.4), leaving the effective diffusion constant as the only unknown parameter in the model. We proceed to determine this effective diffusion constant by fitting our model to the time evolution of the experimental data. To this end, we either fit the data from individual time points, as described in Subsection 5.3.5, or fit the data from multiple time points simultaneously, as explained in Subsection 5.3.6. The results of these fits are summarised in Subsection 5.3.7. We find that the model derived here provides a good description of the data at early experimental time points but fails to describe the data obtained at later times. Therefore, we will present a nonlinear extension to this model in the following Section 5.4.

5.3.1 Formalising IKNM based on apical crowding

Our mathematical formalisation focuses on the crowding of nuclei at the apical side of the tissue. Crowding can be thought of, mathematically, as creating a gradient in nuclear concentration c along the apicobasal direction of the retina. In contrast, we assume no dependence of the nuclear concentration on the lateral position within the tissue. Thus we employ the diffusion equation for the nuclear concentration $c(r,t)$ as a function only of the apicobasal distance r and time t.

We first study the simplest diffusion equation for this system, in which there is a diffusion constant D independent of position, time, and c itself, namely

$$\frac{\partial c(r,t)}{\partial t} = D\frac{1}{r^2}\frac{\partial}{\partial r}\left(r^2\frac{\partial c(r,t)}{\partial r}\right). \tag{5.2}$$

By analysing the experimental data we seek to determine D. This equation provides the basis for our mathematical description of IKNM in terms of a diffusion process.

In addition to Equation 5.2, we also need to specify the boundary conditions adequate for describing IKNM. As mentioned above, we focus our description of IKNM on the apical crowding of nuclei. Since nuclei only divide close to the apical surface of the tissue, we treat mitosis as creating an effective influx of nuclei through the apical boundary. To quantify this influx, we extract the number of cells $N(t)$ as a function of time. As during the stages of development examined here cells are neither dying nor exiting the cell cycle [135], we assume that the number of cell divisions is always proportional to the number of currently existing cells. This assumption predicts an exponential increase in the number of cells or nuclei over time, also recently found by Matejčić, Salbreux and Norden [136],

$$N(t) = N_0 e^{t/\tau}, \tag{5.3}$$

where N_0 is the initial number of nuclei and $\tau = T_P/\ln 2$, with T_P the average cell cycle length. In the case of the main data set, a sufficient number of nuclear tracks covering a whole cell cycle is available. Thus we directly calculate the average cell cycle duration from these tracks. Figure 5.5 shows the agreement between the theoretically predicted curve $N(t)$ and the experimentally obtained numbers of nuclei over time. Having obtained N_0 and T_P from our experimental data, the predicted curve does not have any remaining free parameters and thus no fitting is necessary.

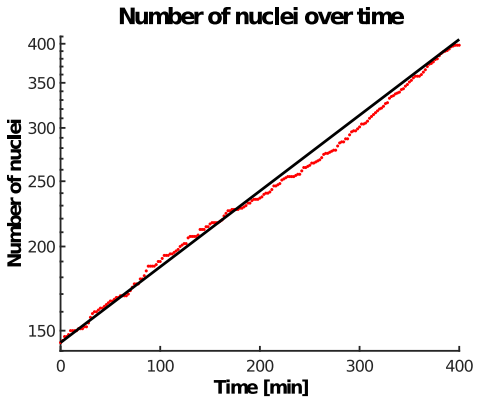

Figure 5.5 **Time evolution of the number of nuclei.** The number of nuclei in the examined section of retinal tissue grows exponentially, as predicted by Equation 5.3. In this graph, the experimental number of nuclei as a function of time is shown in red while the black curve corresponds to Equation 5.3, with N_0 and T_P as obtained from the experimental data (log-lin plot). Thus, no fitting is necessary.

For the other datasets, we subsequently make use of the fact that the number of nuclei follows an exponential growth law (as stated in Equation 5.3) to retrieve T_P. Knowing the initial number of tracked nuclei N_0 for each data set, we obtain T_P from fitting $\ln N(t) = \ln N_0 + t/\tau = \ln N_0 + (\ln 2/T_P)t$ to the number of nuclei as a function of time in a log-lin plot. Then T_P can be deduced from the slope of this fit.

The description for the number of nuclei over time, Equation 5.3, can be used to formulate the influx boundary condition for our mathematical model (for full derivation see Appendix 5.A)

$$D\frac{\partial c}{\partial r}\bigg|_{r=a} = \frac{1}{S}\frac{\partial N(t)}{\partial t} = \frac{N_0}{S\tau}e^{t/\tau} \tag{5.4}$$

where S is the apical surface area of our domain of interest (i.e. the surface area through which the effective nuclear influx occurs). Here, we calculate S from the solid angle Ω obtained earlier in the calculation of the nuclear concentration profiles (see Subsection 5.2.2). The surface area is simply given as $S = \Omega a^2$.

In contrast to the apical side of the tissue, there is no creation (or depletion) of nuclei at the basal side [136], and hence we apply a no-flux boundary condition here,

$$\frac{\partial c}{\partial r}\bigg|_{r=b} = 0. \tag{5.5}$$

Equations 5.2, 5.4 and 5.5 fully specify this simplest mathematical model of IKNM.

5.3.2 The diffusion model has no non-trivial steady states

Before we attempt to solve the diffusion model for IKNM, we first analyse the existence of steady states in the derived mathematical model. To this end, we set $\partial c/\partial t = 0$ in Equation 5.2. Thus

$$\begin{aligned} 0 = \frac{\partial c}{\partial t} &= D\frac{1}{r^2}\frac{\partial}{\partial r}\left(r^2\frac{\partial c}{\partial r}\right) \\ \Rightarrow 0 &= \frac{\partial}{\partial r}\left(r^2\frac{\partial c}{\partial r}\right) \end{aligned} \tag{5.6}$$

where we omit the trivial solution $D = 0$. It follows that the term $r^2\,(\partial c/\partial r)$ must be a constant with respect to r. Now considering the basal boundary condition, Equation 5.5, we find at $r = b$

$$r^2\frac{\partial c}{\partial r} = b^2\frac{\partial c}{\partial r}\bigg|_{r=b} = 0. \tag{5.7}$$

Therefore, $r^2\,(\partial c/\partial r) = 0$ must hold for all r, including $r = a$. Combining this expression with the apical boundary condition, Equation 5.4, thus yields

$$0 = r^2\frac{\partial c}{\partial r} = a^2\frac{\partial c}{\partial r}\bigg|_{r=a} = \frac{a^2}{D}\frac{N_0}{S\tau}e^{t/\tau}. \tag{5.8}$$

This equation only has the trivial solution $N_0 = 0$, i.e. $c(r,t) = 0$. Therefore, there are no (non-trivial) steady state solutions for the distribution of nuclei across the retinal tissue according to this diffusion model.

5.3.3 The nuclear concentration profile

From Equations 5.2, 5.4 and 5.5 we can derive an expression for the concentration of nuclei $c(r,t)$ in the retinal tissue. To this end, we introduce dimensionless variables for space and time,

$$\xi = \frac{r}{a}, \qquad s = \frac{Dt}{a^2} \tag{5.9}$$

and further define $\rho = b/a < 1$. The exact solution for the nuclear concentration, of which the detailed derivation is given in the Appendix 5.B, is

$$c(\xi,s) = \sum_{i=1}^{\infty} \left(h_i e^{-\lambda_i^2 s} + \frac{\alpha_i f_0}{\sigma + \lambda_i^2} e^{\sigma s} \right) H_i(\xi) + \frac{1}{1-\rho} \left(\frac{1}{2}\xi^2 - \rho\xi + g_0 \right) f_0 e^{\sigma s}. \quad (5.10)$$

The first term within parentheses describes the decay over time of the initial condition $c(\xi, s=0)$. Here, λ_i are the eigenvalues and $H_i(\xi)$ the eigenfunctions of the radial diffusion problem, and the coefficients h_i are determined from the experimental initial condition (see Equation 5.11 below). The second terms within the sum and the final term on the right hand side of Equation 5.10 are constructed such that the solution fulfils the boundary conditions 5.4 and 5.5. In the last term, the constant g_0 can be obtained using the constraint that the volume integral of the initial concentration yields the initial number of nuclei N_0 (see Appendix 5.B). f_0, σ and α_i emerge within the calculation of the solution and are specified in Appendix 5.B. Thus, the effective diffusion constant D in Equations 5.2 and 5.10 is the only unknown in the model.

To determine D, we fit our analytical solution in Equation 5.10 to the data obtained from the experiments. To fit D and calculate h_i we convert the experimental distribution of nuclei in the retinal tissue into a concentration profile as described in Subsection 5.2.2. Then we rescale the data in accordance with the non-dimensionalisation of the theoretical variables r and t (see Equation 5.9). Thus we obtain $c_{\mathrm{exp}}(\xi,s)$ from $c_{\mathrm{exp}}(r,t)$. Thereafter, the optimal D-value, henceforth termed D^*, can be retrieved using a minimal-χ^2 approach.

5.3.4 The initial condition can be extracted from experiments

We determine the prefactors h_i in Equation from the experimental nuclear distribution at the start of the experiment, $c_{\mathrm{exp}}(\xi,0)$. For convenience, we choose to determine first $\widetilde{h_i} = h_i + \alpha_i f_0/(\sigma + \lambda_i^2)$ and then calculate h_i by subtracting $\alpha_i f_0/(\sigma+\lambda_i^2)$ from the results. The $\widetilde{h_i}$ can be computed from the data, using Equation 5.10 for $s = 0$, as

$$\widetilde{h_i} = \sum_m \xi_m^2 H_i(\xi_m) c_{\mathrm{exp}}(\xi_m, 0) \Delta\xi_{\mathrm{m}} - \frac{f_0}{1-\rho} \int_\rho^1 \xi^2 H_i(\xi) \left(\frac{1}{2}\xi^2 - \rho\xi + g_0 \right) d\xi, \quad (5.11)$$

where m denotes the m-th binned data point, ξ_m its position and $\Delta\xi_{\mathrm{m}}$ the width of bin m. As in Equation 5.10, the index i denotes the i-th eigenfunction or -mode. The resulting initial

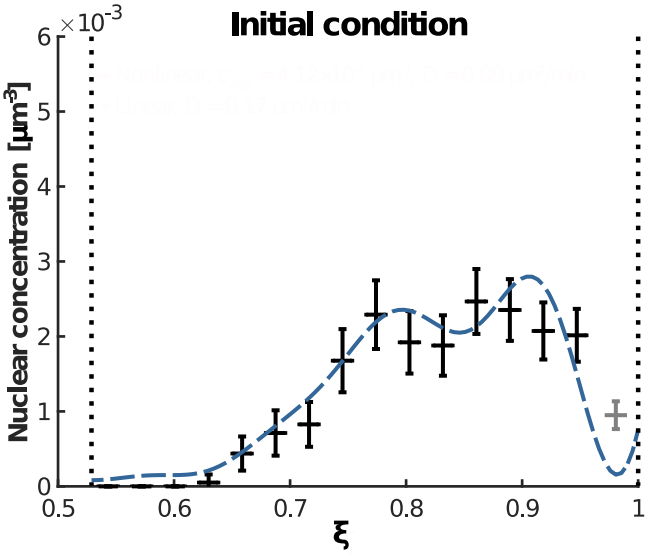

(a)

Figure 5.6 **Initial condition nuclear concentration profile.** This plot shows the initial condition for fitting the concentration profiles. Experimental data is shown in black with data points not subsequently included in the fit in grey (data binning width 3 µm, apical exclusion width 4 µm). Error bars are the uncertainties in nuclear concentration and data point location resulting from the uncertainties in bin counts as calculated in Subsection 5.2.2. The blue dashed curve represents the initial condition calculated using Equations 5.10 for $s = 0$ and 5.11. The vertical black dotted lines indicate the ξ-values where the boundary conditions are applied, equivalent to $a = 104$ µm and $b = 55$ µm.

condition curve is shown in Figure 5.6.

5.3.5 Fitting individual time points to obtain D

For fitting D, we employ a minimum-χ^2 method. In this approach, the goodness of fit parameter reads $\chi^2 = \sum_m \left(c_{\text{exp}}(\xi,s) - c(\xi,s)\right)^2 / \sigma_m^2$, where $\sum_m$ denotes the summation over all bins m [137]. Since binning the experimental data results in uncertainties $\sigma_{y,\text{bin}}$ and $\sigma_{x,\text{bin}}$ in the x- and y-directions (compare Subsection 5.2.2), both have to be taken into account when calculating σ_m and χ^2. The combined contribution of x- and y- uncertainties is $\sigma_m^2 = \sigma_{y,m}^2 + \sigma_{y,\text{indirect},m}^2$ with $\sigma_{y,\text{indirect},m} = \sigma_{x,m}\left(\mathrm{d}c(\xi,s)/\mathrm{d}\xi\right)\big|_{\xi=\xi_m}$ [137]. In our fits, we calculate the value χ^2 for a large range of possible diffusion constants D, from $D = 0.01$ µm^2/min to $D = 10$ µm^2/min. By finding the value of D for which χ^2 becomes minimal for a given data set and time point, we establish our optimal fit.

The width of the so obtained $\chi^2(D)$-curve at $\chi^2 = \chi^2_{\text{min}} + 1$ indicates the standard deviation of the optimal D-value, σ_{D^*} [137]. By approximating the minimum with a quadratic curve, we obtain an estimate for this standard deviation as $\sigma_{D^*} = \Delta D \sqrt{2\left(\chi^2_{D^*-\Delta D} - 2\chi^2_{D^*} + \chi^2_{D^*+\Delta D}\right)}$ [137] where ΔD is the step size between individual fitted D-values, here $\Delta D = 0.01$ µm^2/min.

In principle, the full solution for $c(\xi, s)$ in Equation 5.10 is composed of infinitely many modes. However, in practice, we truncate this series and only include a finite number of modes in our fits. This is due to the fact that we have a finite set of data points, so adding too many modes could lead to overfitting. We use the Nyquist–Shannon sampling theorem which states that the bandlimit frequency of modes to be fitted must be smaller than $1/2$ the sample (or data) frequency [138]. In order to be consistent between data sets, we here choose a maximum number of 8 modes to be included in all performed fits. For the large normal condition data set, fits with a range of numbers of modes were found to result in the same value D^*.

To determine the range of data to be included in our fits we use the range of nuclear sizes in our experimental system. We first randomly select 100 nuclei from our dataset of tracked nuclei and measure the size of their longest diameter in both the xy- and yz-planes of the microscopy image stacks. From these measurements we establish that the size of the principal semi-axes of each nucleus is likely to be in the range of about 3 µm to 5 µm, where the nuclear shape is regarded to be ellipsoidal. Because the centre of a nucleus cannot be any closer to a surface than the nuclear radius all data collection very close to the apical or basal tissue surfaces must have been due to the measurement uncertainties Δr mentioned in Subsection 5.2.1. Thus, any data closer than 3 µm to 5 µm from the apical or basal tissue surfaces is not taken into account for fitting.

The minimal-χ^2 approach indeed enables us to determine the optimal binning width Δr_{bin} (or $\Delta\xi_{\text{bin}}$) and width of data exclusion for the fits. In order to do so, fits of the normal data set are performed for different data binning widths and exclusion sizes of 3 µm to 5 µm. For each of these fits the χ^2-value and the number of degrees of freedom ν, i.e. the number of data points minus the number of free fit parameters (here number of data points minus 1), are registered. From χ^2 and ν we calculate the reduced χ^2 value, $\chi^2_\nu = \chi^2/\nu$ [137]. Using ν and χ^2_ν, the probability $P_\chi(\chi^2;\nu)$ of exceeding χ for a given fit can be estimated, which should be approximately 0.5 [137]. We find our optimal data binning width of 3 µm to 4 µm as the width that results in a $P_\chi(\chi^2;\nu)$ as close to 0.5 as possible for all the different time points when fitting the nonlinear model which we present in Section 5.4. The exact

choice of exclusion width was found not to influence the fitting result for the nonlinear model employed there.

It should be noted that the optimisation of the binning width is based on the largest normal condition data set (see Chapter 4). Therefore, the chosen binning size is not necessarily ideal for the other data sets. As Bevington and Robinson [137] point out, each bin should usually contain a certain minimal number of data points. While this condition is satisfied for nearly all bins of the normal condition data set, due to the smaller size of the other data sets (compare Chapter 4) it is not necessarily satisfied for some of their bins.

All fits are performed using a custom MATLAB [127] routine.

5.3.6 Fitting many time points simultaneously

In addition to fitting data obtained from individual time points, we also investigate whether we can find a single D^* that well describes the data from a whole range of time points simultaneously. To this end, we use a modified minimal-χ^2 approach. Here, we sum the χ^2-values obtained for each D over all time points, in this way producing a $\sum_t \chi^2(D)$-curve. The minimum of this curve indicates D^* for the whole time series. Furthermore, dividing $\sum_t \chi^2(D)$ by the number of time points included in the optimization yields an average χ^2- and reduced χ^2-value corresponding to this D^*. Finally, for the overall fits we use the width of this time averaged $\chi^2(D)$-curve at $\chi^2 = \chi^2_{\text{min}} + 1$ to obtain the standard deviation of the overall optimal D-value.

Again, we perfom these fits using a custom MATLAB [127] routine.

5.3.7 The linear model describes early IKNM only

The overall optimal D-value obtained using the diffusion model in Equation 5.10 is $D^*_{\text{lin}} = (0.17 \pm 0.07)$ µm^2/min when taking all data up to $t = 200$ min into account (binning width 3 µm, apical exclusion width 4 µm).

Using this value D^*, we can examine the decay times of the different modes in the first term of Equation 5.10. The slowest decaying modes are the ones with the smallest eigenvalues λ_i and we find that the longest three decay times are $\mathscr{T}_1 \approx 1325$ min, $\mathscr{T}_2 \approx 350$

min and $\mathscr{T}_3 \approx 158$ min. This shows that indeed all three terms of Equation 5.10 are relevant on the timescale of our experiment and need to be taken into account when calculating the concentration profile.

Two plots of $c(\xi, s)$ corresponding to the fits with $D^*_{\text{lin}} = (0.17 \pm 0.07)$ µm^2/min are shown in Figures 5.7 (a) and (b). As can be seen from this figure, the diffusion model fits the data very well at early times, $t \leq 200$ min. However, for $t \geq 200$ min the model does not fit the data as well. The experimentally observed nuclear concentration levels off at a value between 4.00×10^{-3} µm^{-3} and 4.50×10^{-3} µm^{-3}, an aspect that is not captured by the model of linear diffusion (compare Figure 5.7 (c) which shows the individual time point fit for $t = 300$ min). Furthermore, as we will discuss again in the next Section, the optimal D-value for individual time point fits varies considerably between the time points, especially for $t \geq 200$ min.

Therefore, in the following Section 5.4, we explore a possible reason for the deviation between experimental data and the linear diffusion model and present an alternative, nonlinear diffusion model which better explaines the experimental observations.

5.4 A nonlinear diffusion model for IKNM

In this Section, we present an alternative diffusion model in order to improve our fits compared to the results obtained using Equation 5.2. First, in Subsection 5.4.1, we discuss a possible reason why the previously presented model might be failing to describe the experimental data at later times. Then, in Subsection 5.4.2, we introduce a nonlinear extension to the model, which might be able to adjust for the shortcoming of the previous version. This new model introduces a maximum possible nuclear packing density, i.e. a maximum concentration c_{max}, which we calculate in Subsection 5.4.4. Afterwards, in Subsection 5.4.5, we fit the new model to the experimental data, similar to the fits performed in the previous Section. We compare the results obtained from fitting individual time point data to the results from similar fits using the linear model to demonstrate the improvement in fit outcome due to the nonlinear extension in Subsection 5.4.6. Finally, we present the results of fitting the data of many time points simultaneously in Subsection 5.4.7. We conclude that the nonlinear model is suitable to describe the nuclear distribution in the retinal tissue during IKNM quantitatively for the whole period of embryonic development studied here.

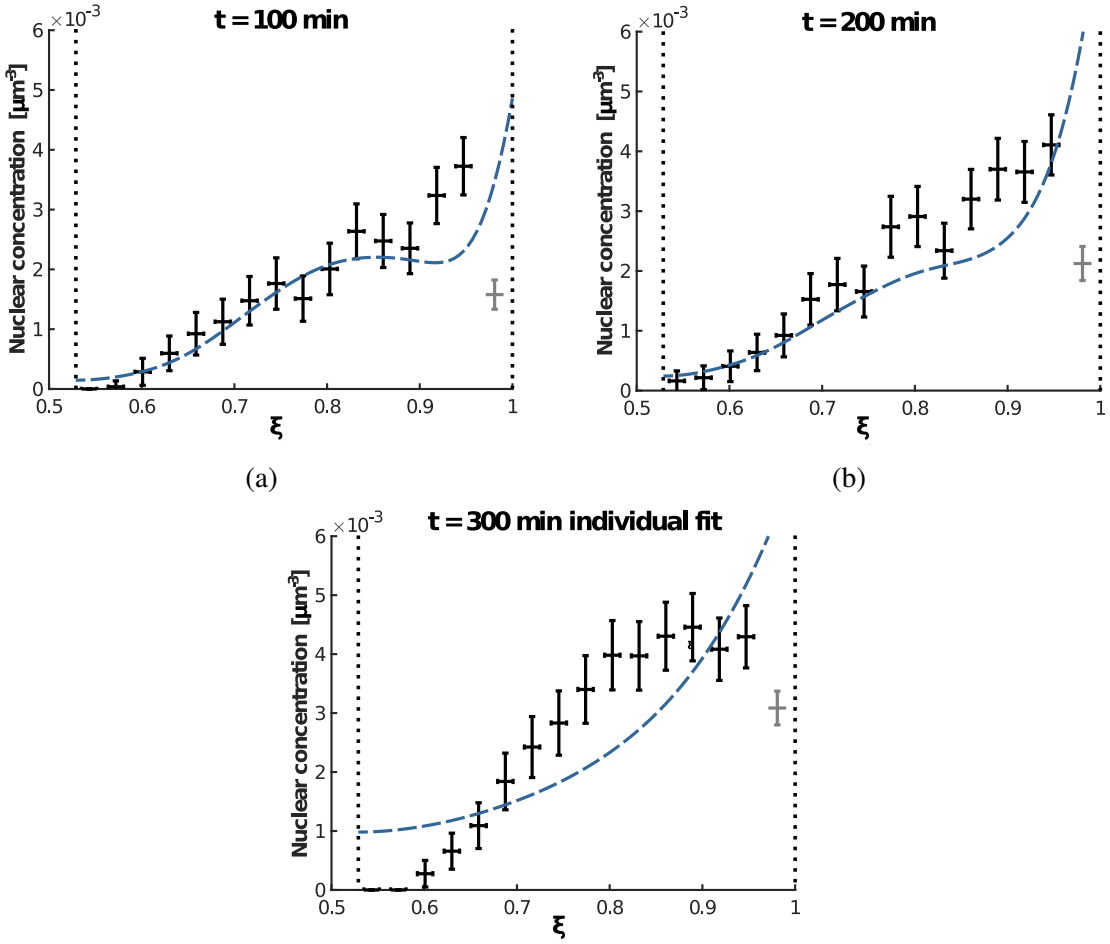

Figure 5.7 **Fit results using the linear model.** Exemplary plots for fitting the data of all time points up to $t = 200$ min simultaneously (plots (a) for $t = 100$ min and (b) for $t = 200$ min) and for fitting the data of individual time points (plot (c) for $t = 300$ min). Experimental data is shown in black with data points not included in the fit in grey. Error bars are the uncertainties in nuclear concentration and data point location resulting from the uncertainties in bin counts as calculated in Subsection 5.2.2. All fits are performed using a binning width of 3 µm and an apical exclusion width of 4 µm. The vertical black dotted lines indicate the ξ-values where the boundary conditions are applied, equivalent to $a = 104$ µm and $b = 55$ µm. The blue dashed curves represent the respective fit results. The linear model provides a good fit of the data for small experimental times but fails to reproduce the data for larger t.

5.4.1 Motivation of the nonlinear model

One particular aspect of the biology that the linear model neglects is the spatial extent of the nuclei. In a linear diffusion model, particles are treated as point-like and non-interacting. However, our microscopy images clearly indicate that the nuclei have finite incompressible volumes (compare Figure 4.1 (a) in Chapter 4), so that their dense arrangement within the retinal tissue leads to steric interactions once the nuclear concentration is sufficiently high (i.e. at later time points during the experiment). Moreover, the packing density of nuclei can not exceed a maximum value dictated by their geometry. Next, we examine whether accounting for these effects leads to a more accurate theory.

5.4.2 The nonlinear model as an extension of the linear version

If we write the diffusion equation 5.2 in the form

$$\frac{\partial c}{\partial t} = D\frac{1}{r^2}\frac{\partial}{\partial r}\left(r^2 c\frac{\partial}{\partial r}\left(\frac{\partial}{\partial c}(c\ln c)\right)\right), \tag{5.12}$$

we can identify the term $c\ln c$ as proportional to the entropy $\mathscr{S}$ of an ideal gas (except for terms linear in c), and its derivative with respect to c as a chemical potential.

In an ideal gas, all particles are treated as point-like and without mutual interactions. In order to include the spatial extent of the nuclei, we estimate the entropy using the model of a lattice gas as introduced in Chapter 3. Due to the discrete lattice in this model, particles cannot get closer than the lattice spacing to each other, and there is a maximum possible concentration $c_{\max}$ [14].

Substituting the Expression 3.16 for the term $c\ln c$ in Equation 5.12, we obtain the nonlinear diffusion equation

$$\frac{\partial c}{\partial t} = D\frac{1}{r^2}\frac{\partial}{\partial r}\left(r^2\frac{c_{\max}}{c_{\max}-c}\frac{\partial c}{\partial r}\right). \tag{5.13}$$

Adjusting the boundary conditions at the apical side of the tissue accordingly leads to

$$D\frac{c_{\max}}{c_{\max}-c}\frac{\partial c}{\partial r}\bigg|_{r=a} = \frac{N_0}{S\tau}e^{t/\tau}, \tag{5.14}$$

while the basal boundary condition remains the same as Equation 5.5. Together, Equation 5.13 and the boundary conditions in Equations 5.14 and 5.5 represent an extension to the

diffusion model for IKNM, which now accounts for steric interactions between the nuclei.

Due to the introduction of the maximum nuclear concentration $c_{\max}$, this model is now valid for $c < c_{\max}$ only.

5.4.3 The nonlinear model has no non-trivial steady states

Similar to the approach for linear diffusion model in Section 5.3, we first analyse the existence of steady states in the nonlinear diffusion model as well. We here set $\partial c/\partial t = 0$ in Equation 5.13 and thus ontain

$$\begin{aligned} 0 = \frac{\partial c}{\partial t} &= D\frac{1}{r^2}\frac{\partial}{\partial r}\left(r^2\frac{c_{\max}}{c_{\max}-c}\frac{\partial c}{\partial r}\right) \\ \Rightarrow 0 &= \frac{\partial}{\partial r}\left(r^2\frac{c_{\max}}{c_{\max}-c}\frac{\partial c}{\partial r}\right) \end{aligned} \tag{5.15}$$

where, as previously, we omit the trivial solution $D = 0$. It follows that, in the case of the nonlinear model, the term $r^2 c_{\max}/\left(c_{\max}-c\right)\left(\partial c/\partial r\right)$ must be a constant with respect to r. Now considering the basal boundary condition, Equation 5.5, we find at $r = b$

$$r^2\frac{c_{\max}}{c_{\max}-c}\frac{\partial c}{\partial r} = b^2\frac{c_{\max}}{c_{\max}-c}\frac{\partial c}{\partial r}\bigg|_{r=b} = 0. \tag{5.16}$$

Therefore, $r^2 c_{\max}/\left(c_{\max}-c\right)\left(\partial c/\partial r\right) = 0$ must hold for all r. At the apical tissue surface we employ the new boundary condition, Equation 5.14, and hence find

$$0 = r^2\frac{c_{\max}}{c_{\max}-c}\frac{\partial c}{\partial r} = a^2\frac{c_{\max}}{c_{\max}-c}\frac{\partial c}{\partial r}\bigg|_{r=a} = \frac{a^2}{D}\frac{N_0}{S\tau}e^{t/\tau}. \tag{5.17}$$

The only solution of this equation is the trivial solution $N_0 = 0$, which implies $c(r,t) = 0$. Therefore, like for the linear diffusion model, there are no (non-trivial) steady state solutions for the distribution of nuclei across the retinal tissue according to the nonlinear diffusion model.

5.4.4 Obtaining the maximum concentration from nuclear packing

In order to determine the maximum nuclear concentration $c_{\max}$ for the nonlinear model, we again use our estimation of the range of nuclear sizes (compare Subsection 5.3.5). The range of nuclear principal semi-axes lengths of about 3 µm to 5 µm leads to the range of possible maximum concentrations $c_{\max}$, although we did not measure the precise nuclear volume. The lower limit for the nuclear volume is set by the volume of a sphere of radius 3 µm, the upper limit by a sphere of radius 5 µm. Taking into account the maximum possible packing density of nuclei, which for aligned ellipsoids is the same as that of spheres [139], $\pi/\left(3\sqrt{2}\right) \approx 0.74$, we obtain a range of $1.41 \times 10^{-3}\ \mu\text{m}^{-3} \leq c_{\max} \leq 6.55 \times 10^{-3}\ \mu\text{m}^{-3}$.

5.4.5 Fitting the nonlinear model

Similar to fitting the linear model, we also need to establish a description of the initial condition. To make both models consistent with each other, we employ the linear model's initial condition, Equation 5.10 at $s = 0$ with h_i as obtained from Equation 5.11, as an initial condition for this nonlinear model as well.

The time evolution of this initial condition, according to Equation 5.13, is performed using the pdepe solver [140] in MATLAB [127].

Fitting this concentration profile to the data is again carried out by means of a minimal-χ^2 approach for either individual time points or a range of time points as described in Subsections 5.3.5 and 5.3.6, respectively.

For the overall time point fits, based on the average reduced χ^2-values, we also compare several $c_{\max}$-values within the range established above for each data set to find the fit with probability $P_\chi(\chi^2; \nu)$ the closest to 0.5 in each case.

5.4.6 The nonlinear model improves individual time point fits

The resulting values for the diffusion constant D^* as a function of the experimental time point of which the data was fitted are shown in Figure 5.8 (a) for both the linear model described in Section 5.3 as well as the nonlinear model described here. As the plot shows, the best fit for the diffusion constant D^* does not strongly depend on the choice of model for experimental

time points up to approx. 200 min or 250 min. However, for later times, D^* appears to be model-dependent with lower values for $c_{\max}$ tending to lead to lower and overall more constant values of D^*.

This result provides support for the nonlinear model over the linear model. Firstly, from a biological point of view, there is no obvious reason why the diffusion constant would suddenly change so much and fluctuate so strongly as indicated by the linear model. Furthermore, we have previously seen in Section 5.3 that the linear model did not fit the data at later time points well. In contrast Figure 5.8 (b) shows the individual time point fit of the nonlinear model for $t = 300$ min (red solid line, binning width 3 µm, apical exclusion width 4 µm, $c^*_{\max} = 4.12 \times 10^{-3}$ µm^{-3}). In comparison to the individual time point fit performed using the linear model from Section 5.3 (Figure 5.8 (b) blue dashed line), the nonlinear model clearly provides a much better fit of the data.

Finally, the result that the right choice of $c_{\max}$ leads to a roughly constant value of D^* independent of the experimental time point of which data was fitted promts us to also examine the multiple time point fits for the nonlinear model.

5.4.7 The nonlinear model describes the data for all times well

When the optimisation over multiple time points takes all the data up to $t = 200$ min into account, we find $D^*_{\text{nonlin}} = (0.09 \pm 0.05)$ µm^2/min (see Figure 5.9, binning width 3 µm, apical exclusion width 4 µm, $c^*_{\max} = 4.12 \times 10^{-3}$ µm^{-3}). As can be seen, by choosing $c_{\max}$ correctly, an excellent fit to the data can be obtained not only for individual time points but for a whole range of data. These results show that a lattice-gas based diffusion model is indeed suitable to describe the time evolution of the nuclear concentration profile in zebrafish retina tissue during IKNM over several hours of development.

5.5 Experimental incubation temperature influences IKNM

The diffusion model may also address mechanistic questions about IKNM in retinas growing under varying experimental conditions. Zebrafish embryos are often grown at different temperatures to manipulate their growth rate [141] [142], but it has been unclear how the

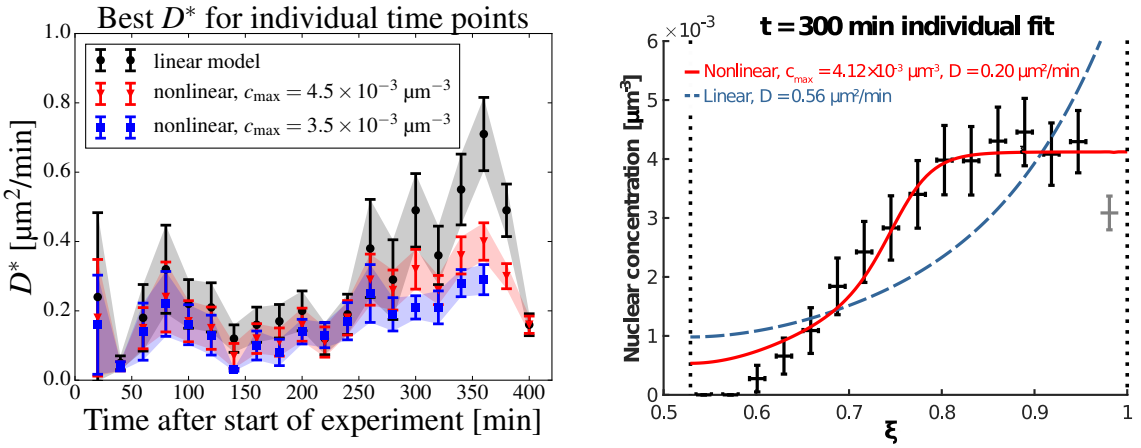

(a) (b)

Figure 5.8 **Comparison of individual time point fit results using both models.** The data of individual time points is fitted using either the linear diffusion model presented in Section 5.3 or the nonlinear model introduced in Section 5.4. All fits are performed using a binning width of 3 µm and an apical exclusion width of 4 µm. (a) This plot provides a comparison of the resulting D^* values for various time points. D^* values obtained using the linear model are depicted as black circles. For fitting the nonlinear model, two different values of c_{max} are shown here: $c_{max} = 4.5 \times 10^{-3}$ µm^{-3} (red triangles) and $c_{max} = 3.5 \times 10^{-3}$ µm^{-3} (blue squares). Error bars represent the standard deviation σ_{D^*}. While the resulting D^* differ very little when fitting data from $t \leq 200$ min or 250 min, they appear model-dependent for later times, with the nonlinear model generally producing less variable results. (b) Examplary fit results for $t = 300$ min. Experimental data is shown in black with data points not included in the fit in grey. Error bars are the uncertainties in nuclear concentration and data point location resulting from the uncertainties in bin counts as calculated in Subsection 5.2.2. The vertical black dotted lines indicate the ξ-values where the boundary conditions are applied, equivalent to $a = 104$ µm and $b = 55$ µm. The blue dashed line and red solid line represent the fit result when applying the linear model and nonlinear model with $c_{max} = 4.12 \times 10^{-3}$ µm^{-3}, respectively. As the graph shows, the experimental data levels off close to the apical tissue surface (located at $\xi = 1$), an aspect that is only reproduced by the nonlinear model. Therefore, the nonlinear model provides a much improved fit of the data compared to the linear version.

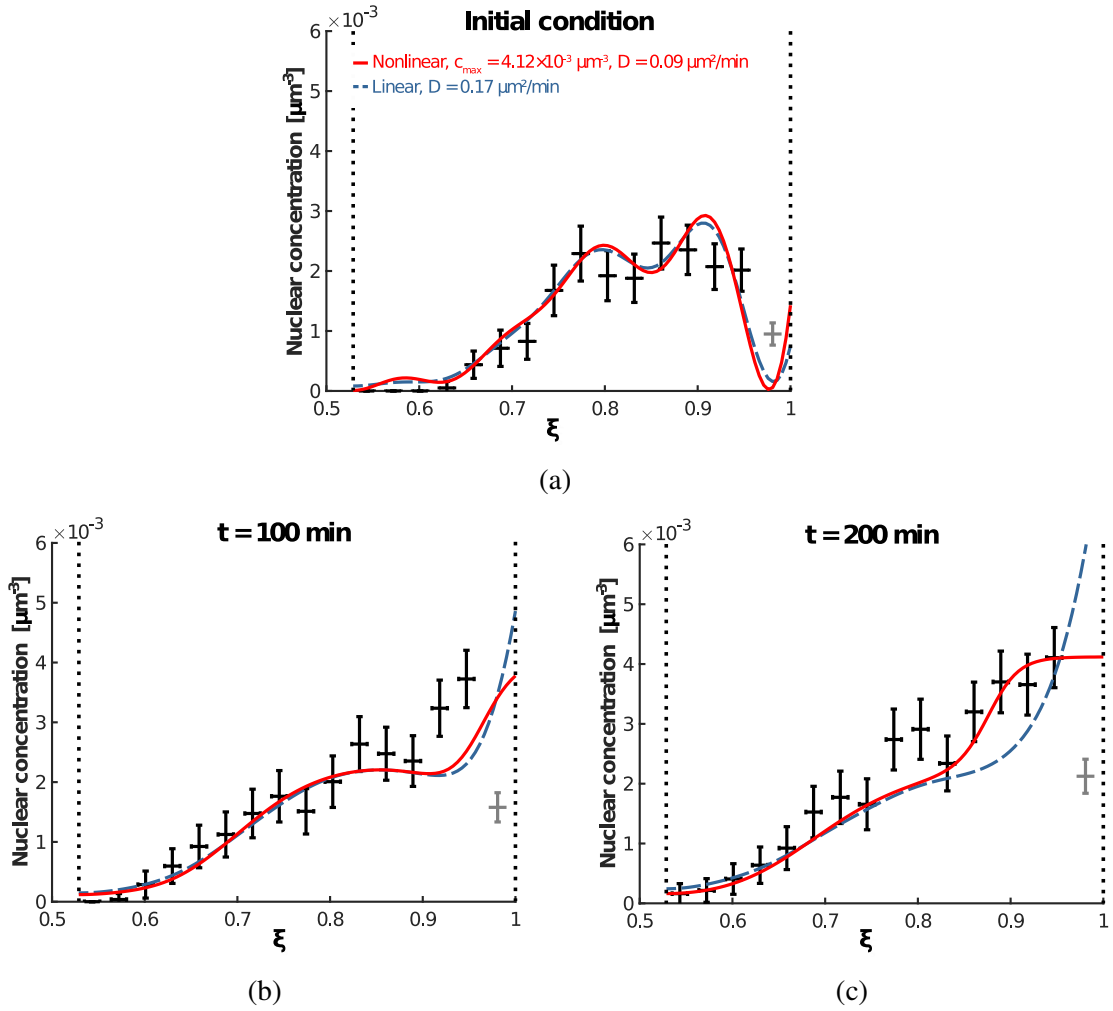

Figure 5.9 **Multiple time point fit results using both models.** The data of all time points up to $t = 200$ min is fitted simultaneously using either the linear diffusion model presented in Section 5.3 (blue dashed lines) or the nonlinear model introduced in Section 5.4 with $c_{\max} = 4.12 \times 10^{-3}$ µm^{-3} (red solid lines). The initial condition curves (plot (a)) and representative fit results for $t = 100$ min (plot (b)) and $t = 200$ min (plot (c)) are shown. Experimental data is shown in black with data points not included in the fit in grey. Error bars are the uncertainties in nuclear concentration and data point location resulting from the uncertainties in bin counts as calculated in Subsection 5.2.2. All fits are performed using a binning width of 3 µm and an apical exclusion width of 4 µm. The vertical black dotted lines indicate the ξ-values where the boundary conditions are applied, equivalent to $a = 104$ µm and $b = 55$ µm. The resulting curves of the linear and nonlinear model are nearly identical for small t, but for larger times the nonlinear model provides an improved fit.

Table 5.1 **Fitting results for all studied experimental conditions.** List of overall best-fit diffusion constants D^*_{nonlin}, their standard deviations and probabilities for the normal condition (28.5 °C) data set described in the main text, a repeat normal condition data set and data sets obtained under higher (32 °C) or lower (25 °C) incubation temperature.

	D^*_{nonlin} (μm^2/min)	σ_{D^*} (μm^2/min)	$P_\chi(\chi^2;\nu)$
Normal	0.09	0.05	0.49 - 0.51
Normal (repeat sample)	0.10	0.06	0.47 - 0.48
High T	0.13	0.08	0.42
Low T	0.06	0.05	0.69 - 0.7

nuclei in the retina behave at these different temperatures.

To examine this issue, we grow the embryos at the normal temperature of 28.5 °C overnight and then incubate them at lower temperature (LT) of 25 °C or higher temperature (HT) of 32 °C during imaging. We obtain the respective cell cycle lengths from experimental data using Equation 5.3 as described in Section 5.3 and find that in HT the average cell cycle takes 205.5 min, while in LT it takes a much longer 532.78 min.

We are then able to use these values in the nonlinear model to investigate whether the change in temperature influences the processes that determine the effective diffusion constant of the nuclei. The resulting values for D^*_{nonlin} are summarised in Table 5.1.

Based on the values in Table 5.1, we perform two-sided t-tests for unequal variances, also known as Welch's t-tests [143], to assess whether there are significant differences between the different samples. It should be noted again that the D^* and σ_{D^*} values are not obtained by averaging several data sets of the same experimental condition but instead each value results from one data set only. Nevertheless, the sample size for each data set is set to 100 for the t-tests because 100 time points are taken into account for each overall optimisation. These time points might not be completely uncorrelated, limiting the predictive power of the t-tests performed here.

The t-tests confirm that there is no significant difference between the D^*-values obtained from the two normal condition data sets. In contrast, D^*-values for the LT and HT data sets are significantly different from the normal ones, with $p \leq 0.01$. These results indicate, that aside from its effect on cell cycle length, incubation temperature is likely to influence IKNM directly by altering the mobility of nuclei, here represented by the effective diffusion constant

D^*.

The temperature dependence of D^* provides some first indications for possible microscopic mechanisms of IKNM, which we will further explore in Chapter 6.

5.6 Discussion

In this Chapter, we have shown that high density nuclear trajectories can be used to tease apart the possible physical processes behind the apparently stochastic movement of nuclei during interkinetic nuclear migration. Analysis of speed and spatial distributions of more than a hundred nuclei revealed a large degree of variability in their movements during G1 and S phases. Although this variability had been observed before, previous experiments had only considered sparsely labelled nuclei within an otherwise unlabelled environment [94] [92] [96]. Thus, our results provide an important account of the variability of IKNM on a whole tissue level. In effect, the variability of IKNM means that nuclear trajectories appear stochastic during the majority of the cell cycle. Previously, it had been suggested that the origins of this apparent stochasticity lay in the transfer of kinetic energy from nuclei in G2 exhibiting rapid apical migration to nuclei in G1 and S phases of the cell cycle [92]. However, we found no evidence for direct transfer of kinetic energy between nuclei and their immediate neighbours. Recently Shinoda et al. [100] have also provided evidence that suggests direct collisions do not contribute to basalward IKNM. Another possibility is that the stochastic trajectories of G1 and S nuclei might depend on a nuclear concentration gradient between the apical and basal sides of the tissue [103]. This gradient might be formed by nuclear divisions taking place exclusively at the apical surface. We confirmed the presence of such a gradient by calculating the nuclear concentration along the apicobasal dimension within the retinal tissue at various time points. Further, to probe the source of the gradient, we treated a zebrafish retina with HU-AC to stop the cell cycle in S phase. While we observed the build-up of the nuclear concentration gradient over time in the control retina, the nuclear distribution flattened when cell division was inhibited with HU-AC treatment. These phenomenological similarities between IKNM and diffusion suggested the diffusion model for IKNM we subsequently derived.

The diffusion model for IKNM includes two key features: most importantly, it focuses on the crowding of nuclei at the apical surface of the tissue, here included as the apical boundary condition. Additionally, in the nonlinear extension of the model, it incorporates a maximum

possible nuclear concentration. This addition provided a striking overall improvement to the fits to experimental data over periods of many hours. The resulting difference in the obtained D^*-values between the linear and nonlinear versions of our model can be understood heuristically when closely examining the difference between the Equations 5.2 and 5.13. The latter introduces the new term $c_{\max}/(c_{\max}-c)$ which one could think of as corresponding to an effective, concentration dependent diffusion constant $\tilde{D} = Dc_{\max}/(c_{\max}-c)$. In general $\tilde{D}$ will vary across the tissue thickness and, since $c > 0$ for most of the retinal tissue, $\tilde{D} > D$. Therefore, averaging across the retina tissue, $\tilde{D}$ might actually be in very good agreement with the D^*-value found in the linear model. However, the fact the linear model fails to describe, and which leads to a better representation of the data using the nonlinear model, is that the mobility of the nuclei is likely to be concentration dependent.

The underlying processes causing IKNM during the G1 and S phases of the cell cycle in pseudostratified epithelia have been largely elusive. Several partially competing ideas have been put forward, ranging from the involvement of cytoskeletal transport processes to mechanisms of direct energy transfer or movements driven by apical nuclear crowding [110] [111] [92] [86]. Here we showed that a process comparable to diffusion which takes steric interactions between nuclei into account produces an excellent representation of the time evolution of the actual nuclear distribution within the retinal tissue during early development. Consequently, our work builds on earlier models of apical crowding based on *in silico* simulations of IKNM [86]. In addition, our work revealed the remarkable importance of simple physical constraints imposed by the overall tissue architecture, which could not be explored in previous studies which tracked sparse nuclei, and thus lacked the means to explore the effect of such 3-dimensional arrangements. Hence, we paid special attention to the spherical shape of the retina and the concentration of nuclei in that space. Examining the evolution in distribution of nuclei over time unveiled the importance of spatial restriction due to the curvature of the tissue. Additionally, the size of the nuclei in comparison to the neuroprogenitor cells leads to the emergence of a maximum nuclear concentration which must be taken into account to accurately model IKNM.

Another geometrical aspect of the developing retina is the shape of the individual retinal progenitor cells. As described in Chapter 2, these cells are long in the apicobasal direction but thin perpendicular to it. Furthermore, as examined in detail by Matejčić, Salbreux and Norden [136], RPCs actually exhibit a non-uniform actin distribution along their apicobasal axis during the early stages of retinal development. This actin distribution results in a basal nuclear exclusion zone, meaning that nuclei are inhibited from entering the basalmost area of

the retinal tissue [136]. Although we have not explicitely incorporated the basal exclusion zone or the presence of the lateral cell walls in the models of IKNM, both aspects have been considered throughout the various parts of our work. Firstly, in the evaluation of the experimental nuclear velocities, we specifically focussed on the apicobasal component of the nuclear movements (as also indicated in Chapter 3). This choice is due to the cellular geometry of RPCs, as their shape only allows very little lateral movement. Later, when setting up the diffusion model for IKNM, we specifically assumed no dependence of the nuclear concentration c on the angular dimensions of the retinal tissue. Again this specification is based on the cellular geometry. Because of the small radius of RPCs, effective lateral-only (i.e. angular-only) equalisation of the nuclear concentration cannot take place. Any potential angular differences in c could only be balanced by differences in cell division rates or adjustments of nuclear positions along the apicobasal (i.e. radial) dimension of the retina. But retinal growth appears to be homogeneous [136]. Therefore, no angular terms are included in the derived mathematical models of IKNM. Finally, while we do not specifically account for the basal exclusion zone, the existence of this zone naturally emerges in the modelled nuclear concentration profiles. Given that these profiles are fits of the experimental data and that the data itself includes the presence of the exclusion zone, the resulting fits do as well. Incorporating the nuclear exclusion zone explicitely by forcing the modelled nuclear concentration profile to zero at a specific value of the radial coordinate (e.g. by defining a $c = 0$ boundary condition at the radius where the nuclear exclusion zone begins) might have actually been more complicated. In this case, we would have had to extract the precise value of this radius either experimentally or from previous publications. In our model however, knowing the approximate length of RPCs (compare Chapter 2) is sufficient.

Interestingly, as Matejčić, Salbreux and Norden [136] noted, the nuclear exclusion zone starts to vanish at around 36 hpf. Furthermore, these authors observed that simultaneously the RPCs start to elongate in the apicobasal direction. Both aspects seem to lead to an increase in nuclear stacking along the apicobasal dimension of the retina (i.e. an increase of the number of nuclei packed roughly in one line between the apical and basal tissue surfaces) [136]. Given the time scales of our experiments (compare also Chapter 4), these processes appear to be initiated around the same time or slightly after we observe the nuclear concentration to level off close to the apical tissue surface. In the future, it would be interesting to investigate whether there are any connections between these different observations. This is, could the nuclear packing density - by locally approaching $c_{\max}$ - be relevant for triggering the onset of tissue growth?

By changing the incubation temperature during experiments, we finally used the nonlinear model for IKNM to shed light on some of the properties and mechanisms of the stochastic movements of nuclei during IKNM. From our results and previous studies, we knew that cell cycle length is affected by changes in incubation temperature [141] [142]. However, our results also indicate a significant influence of temperature on the mobility of nuclei and thus on the underlying processes controlling their movement. For example, the speed and dynamic properties of both the microtubule and actomyosin systems are dependent on temperature and could in part explain the changes in the diffusion constant that we see as a function of temperature [144] [145] as the diffusion constant may be influenced by stochastic associations with motor proteins or the physical properties of the epithelium. However, a much closer examination of molecular mechanisms driving stochastic nuclear movements is required to better understand the connections between these phenomena. Furthermore, the diffusion constant reported here contains all types of nuclear movement during IKNM as it is derived from the changing nuclear concentration profile over time. However, it is not immediately clear what the contribution of the rapid apical migration to this overall diffusion constant may be. Nonetheless, despite the large displacement during rapid apical migration at G2, this phase only accounts for about 8% of the cell cycle [96]. Therefore, given this small portion of the cell cycle when rapid migration can happen and the good agreement of our calculated diffusion constant with those previously reported in the literature for individual nuclei [96], the proposed model appears to describe tissue wide IKNM quite well.

If one whished to improve the hitherto presented models and incorporate the rapid apicalward migration of nuclei during G2 phase, the following points should be taken into consideration. Most importantly, the rapid apicalward movement of nuclei only takes place during a small period of the cell cycle. Therefore, the total population of nuclei needs to be subdivided into two groups. The nuclei in one group are those performing the random walk motion described so far while the nuclei in the other group are those performing the rapid apicalward movement. The total nuclear concentration profile, $c(r,t)$, that can be fitted to experimental data, then results as the sum of the nuclear concentration profiles of both individual groups. While the movements of nuclei in the first group can still be described using the same set of equations as before, there are several details regarding the mathematical description of the movements of nuclei in the second group that are less obvious. Firstly, we need to establish how the total number of nuclei is to be divided into the two given subgroups. To this end, we need to determine the number of nuclei undergoing rapid apicalward movements as well as their spatial distribution at any given time. The plot in Figure 5.2 (b) shows that we can estimate the approximate onset and duration of apicalward movements

as fractions of the cell cycle length, with these movements starting at about 85% of the cell cycle and persisting for about 8% of the cell cycle [96]. Since we know the average cell cycle length for each data set, we can calculate the expected number of nuclei undergoing apicalward movements at a given time t as $\int_{0.93T_P}^{0.85T_P} N_0 e^{(t-t')/\tau} dt'$. This means, the number of nuclei rapidly moving apicalward at a given time t should be equal to the number of nuclei born approximately during the period $0.93T_P$ to $0.85T_P$ before t. However, in addition to their total number, we need to establish how the rapidly apicalward moving nuclei are distributed throughout the retinal tissue. The plot in Figure 5.2 (c) suggests that at the onset of rapid apicalward movements the respective nuclei are distributed across the whole retina. But this plot does not properly distinguish between the possibilities of these nuclei forming a constant concentration themselves or representing a constant fraction of the total nuclear concentration, for example. In order to clarify this point, additional experiments, where nuclei are labelled with several fluorescent markers to distinguish the different cell cycle phases (compare [98]), are needed. Otherwise, the underlying distribution of rapidly apicalward moving nuclei is subject to assumption. Furthermore, it is not *a priori* clear, whether the nuclei in this phase of movement are still under the influence of the concentration gradient based driving mechanism assumed earlier or whether the rapid apical migration overwrites the concentration gradient based migration in some way. This probably depends on the exact microscopic mechanisms of both modes of migration; however, these mechanisms are still under investigation, as outlined in Chapter 2. As long as this question is not answered, several competing models have to be tested. In any case, these models will need to include a new term to describe the apicalward migration of nuclei as these movements phenomenologically resemble directed (ballistic) movements rather than stochastic ones [92] [96] [98]. Therefore, a new term of the form $\left(1/r^2\right)\left(\partial/\partial r\right)\left(r^2 v_r c_{\text{apicalward}}(r,t)\right)$ needs to be introduced. Here, v_r is the radial component of the velocity field of the apically moving nuclei (which have a concentration profile $c_{\text{apicalward}}(r,t)$). As we have assumed that nuclei are mainly moving along the radial dimension of the retina, the angular components of their velocity field can be set to zero. Even so, including the rapid apicalward migration of nuclei means introducing several new parameters, specifically the time of onset and the duration of these movements as well as v_r, which either have to be estimated from the experimental data or fitted (as in the case of v_r). Futhermore, assumptions about the underlying distribution of these nuclei have to be made. Therefore, we here omit the influence of the rapidly apicalward moving nuclei and continue to work with the hitherto presented models.

Having said this, in the following Chapter 6 we undertake work to better understand the general scale of the diffusion constant ($D^*_{\text{nonlin}} \sim 0.1\ \mu\text{m}^2/\text{min}$) from microscopic consid-

erations, analogous to those used to relate random walks to diffusion [146]. Furthermore, we provide stochastic models based on the nonlinear diffusion model presented here to describe the individual nuclear movements during IKNM. These stochastic models enable us to examine whether the nonlinear model is also capable of reproducing the properties of individual nuclear trajectories. In addition, the results presented in Chapter 6 will further elucidate the possible microscopic mechanisms underlying IKNM.

Appendix 5.A The apical influx boundary condition

The apical influx boundary condition, Equation 5.4, can be obtained from the diffusion equation, Equation 5.2, and the known exponential increase of the number of cells, Equation 5.3. Starting with Equation 5.2, we integrate both sides over the total volume

$$\int dV \left(\frac{\partial c(r,t)}{\partial t} \right) = \int dV \left(D \frac{1}{r^2} \frac{\partial}{\partial r} \left(r^2 \frac{\partial c(r,t)}{\partial r} \right) \right). \tag{5.18}$$

The right hand side of this equation can be rewritten as

$$\int dV \left(\frac{\partial c(r,t)}{\partial t} \right) = \frac{\partial}{\partial t} \left(\int c(r,t) dV \right) = \frac{\partial}{\partial t} \left(N(t) \right) = \frac{N_0}{\tau} e^{t/\tau} \tag{5.19}$$

while for the left hand side we make use of the coordinate-free notation

$$\int dV \left(D \frac{1}{r^2} \frac{\partial}{\partial r} \left(r^2 \frac{\partial c(r,t)}{\partial r} \right) \right) = \int \left(\nabla \cdot (D \nabla c) \right) dV. \tag{5.20}$$

Using Gauss' divergence theorem, the volume integral can be rewritten as a surface integral

$$\int \left(\nabla \cdot (D \nabla c) \right) dV = \int \left((D \nabla c) \cdot \vec{n} \right) dS = \int \left(\left(D \frac{\partial c(r,t)}{\partial r} \right) \cdot \vec{n} \right) dS \tag{5.21}$$

where $\vec{n}$ is the surface normal in each point and dS is the surface element. Because the surface normal $\vec{n}$ and the nuclear concentration gradient $(\partial c)/(\partial r)$ are perpendicular for all the lateral surfaces of the volume V, the contributions of these surfaces to the integral are all zero and only the contributions of the basal and apical surfaces, where $\vec{n}$ and $(\partial c)/(\partial r)$ are parallel in each point, remain. For these surfaces, which we approximate as spherical, we have $dS = \Omega r^2_{\text{surface}}$, thus

$$\int \left(\left(D \frac{\partial c}{\partial r} \right) \cdot \vec{n} \right) dS = \left(D \frac{\partial c}{\partial r} \bigg|_{r=a} \right) \left(\Omega a^2 \right) - \left(D \frac{\partial c}{\partial r} \bigg|_{r=b} \right) \left(\Omega b^2 \right) \tag{5.22}$$

where the different signs between the contributions of the apical and basal surfaces arise from the fact that the surface normal $\vec{n}$ always points outward. Finally requiring the flux through the basal surface to be zero (see Equation 5.5), setting $S = \Omega a^2$ and combining the left and right hand sides of Equation 5.18, we obtain for the apical boundary condition Equation 5.4

$$\begin{aligned} \frac{N_0}{\tau} \cdot e^{t/\tau} &= DS \left.\frac{\partial c}{\partial r}\right|_{r=a} \\ \Rightarrow D \left.\frac{\partial c}{\partial r}\right|_{r=a} &= \frac{1}{S}\frac{1}{\tau} N_0 e^{t/\tau}. \end{aligned} \tag{5.23}$$

Appendix 5.B Full solution of the linear diffusion equation

After rescaling space and time as in Equation 5.9 and introducing $\rho = b/a < 1$, Equation 5.2 and the boundary conditions 5.4 and 5.5 read

$$\begin{aligned} &\frac{\partial c(\xi,s)}{\partial s} = \frac{1}{\xi^2}\frac{\partial}{\partial \xi}\left(\xi^2 \frac{\partial c(\xi,s)}{\partial \xi}\right), \\ &\left.\frac{\partial c(\xi,s)}{\partial \xi}\right|_{\xi=1} = f_0 e^{\sigma s} = f(s) \qquad \text{and} \qquad \left.\frac{\partial c(\xi,s)}{\partial \xi}\right|_{\xi=\rho} = 0, \end{aligned} \tag{5.24}$$

where we have defined $f_0 = aN_0/DS\tau$ and $\sigma = a^2/D\tau$.

We transform this homogeneous differential equation with inhomogeneous boundary conditions into the problem of solving an inhomogeneous differential equation with homogeneous boundary conditions by writing $c(\xi,s)$ as a sum of two contributions,

$$c(\xi,s) = \phi(\xi,s) + \psi(\xi,s), \tag{5.25}$$

where we require $\phi(\xi,s)$ to satisfy the inhomogeneous boundary conditions

$$\left.\frac{\partial \phi(\xi,s)}{\partial \xi}\right|_{\xi=1} = f_0 e^{\sigma s} \qquad \text{and} \qquad \left.\frac{\partial \phi(\xi,s)}{\partial \xi}\right|_{\xi=\rho} = 0. \tag{5.26}$$

These conditions are satisfied if $\phi(\xi,s)$ has the form

$$\phi(\xi,s) = \frac{1}{1-\rho}\left(\frac{1}{2}\xi^2 - \rho\xi + g_0\right) f_0 e^{\sigma s} \tag{5.27}$$

where g_0 is a constant of integration to be determined later.

The remaining problem to solve for $\psi(\xi,s)$ is

$$\frac{\partial\psi(\xi,s)}{\partial s}=\frac{1}{\xi^2}\frac{\partial}{\partial\xi}\left(\xi^2\frac{\partial\psi(\xi,s)}{\partial\xi}\right)+\frac{f_0e^{\sigma s}}{1-\rho}\left(3-\frac{2\rho}{\xi}-\sigma\left(\frac{1}{2}\xi^2-\rho\xi+g_0\right)\right), \tag{5.28}$$

with homogeneous boundary conditions

$$\left.\frac{\partial\psi(\xi,s)}{\partial\xi}\right|_{\xi=1}=0 \qquad \text{and} \qquad \left.\frac{\partial\psi(\xi,s)}{\partial\xi}\right|_{\xi=\rho}=0. \tag{5.29}$$

We can further write $\psi(\xi,s)$ as the sum of two contributions,

$$\psi(\xi,s)=\psi_h(\xi,s)+\psi_p(\xi,s), \tag{5.30}$$

where ψ_h is the general solution of the homogeneous problem

$$\begin{aligned}&\frac{\partial\psi_h(\xi,s)}{\partial s}=\frac{1}{\xi^2}\frac{\partial}{\partial\xi}\left(\xi^2\frac{\partial\psi_h(\xi,s)}{\partial\xi}\right),\\&\left.\frac{\partial\psi_h(\xi,s)}{\partial\xi}\right|_{\xi=1}=0 \qquad \text{and} \qquad \left.\frac{\partial\psi_h(\xi,s)}{\partial\xi}\right|_{\xi=\rho}=0,\end{aligned} \tag{5.31}$$

and ψ_p is a particular solution of the full inhomogeneous problem, Equation 5.28.

The full solution of the homogeneous problem is given as a series of linearly independent eigenfunctions, each of the form

$$e^{-\lambda^2 s}W(\xi)=e^{-\lambda^2 s}\left(A\frac{\sin\lambda\xi}{\xi}+B\frac{\cos\lambda\xi}{\xi}\right), \tag{5.32}$$

where the eigenvalues λ can be found from simultaneous solution of the boundary conditions,

$$\begin{aligned}&A\left(\lambda\cos\lambda-\sin\lambda\right)-B\left(\lambda\sin\lambda+\cos\lambda\right)=0\\&A\left(\frac{\lambda\cos\lambda\rho}{\rho}-\frac{\sin\lambda\rho}{\rho^2}\right)-B\left(\frac{\lambda\sin\lambda\rho}{\rho}+\frac{\cos\lambda\rho}{\rho^2}\right)=0,\end{aligned} \tag{5.33}$$

which yields the transcendental relation

$$\tan\left(\lambda\left(1-\rho\right)\right)=\frac{\lambda\left(1-\rho\right)}{\lambda^2\rho+1}, \tag{5.34}$$

for which each eigenvalue λ_i is a solution corresponding to one of the linearly independent eigenfunctions (only $\lambda_i > 0$ need to be taken into account).

We can further deduce from the Equation 5.33 that $B_i = \beta_i A_i$, where

$$\beta_i=\frac{\lambda_i\cos\lambda_i-\sin\lambda_i}{\lambda_i\sin\lambda_i+\cos\lambda_i}, \tag{5.35}$$

and we normalize the obtained expression for $W_i(\xi)$ from Equation 5.32 to

$$H_i(\xi)=\frac{1}{Y_i}\left(\frac{\sin\lambda_i\xi}{\xi}+\beta_i\frac{\cos\lambda_i\xi}{\xi}\right), \tag{5.36}$$

with

$$Y_i^2=\frac{1}{2}\left(1-\rho\right)\left(1+\beta_i^2\right)-\frac{1}{4\lambda_i}\left(\sin 2\lambda_i-\sin 2\lambda_i\rho\right)\left(1-\beta_i^2\right)+\frac{\beta_i}{\lambda_i}\left(\sin^2\lambda_i-\sin^2\lambda_i\rho\right). \tag{5.37}$$

Thus, the homogeneous solution ψ_h is

$$\psi_h=\sum_{i=1}^{\infty}h_iH_i(\xi)e^{-\lambda_i^2 s}, \tag{5.38}$$

with prefactors h_i to be determined from the initial condition.

In order to find a particular solution of the inhomogeneous problem, we first rewrite Equation 5.28 as

$$\frac{\partial\psi(\xi,s)}{\partial s}-\frac{1}{\xi^2}\frac{\partial}{\partial\xi}\left(\xi^2\frac{\partial\psi(\xi,s)}{\partial\xi}\right)=\mathscr{R}(\xi,s). \tag{5.39}$$

Now, we express $\mathscr{R}(\xi,s)$, as well as the unknown particular solution $\psi_p(\xi,s)$ in terms of the normalized eigenfunctions $H_i(\xi,s)$ of the homogeneous problem,

$$\mathscr{R}(\xi,s)=\sum_{i=1}^{\infty}R_i(s)H_i(\xi), \tag{5.40}$$

and

$$\psi_p(\xi,s)=\sum_{i=1}^{\infty}C_i(s)H_i(\xi). \tag{5.41}$$

Substituting these forms into Equation 5.39, and noting that each term in the series must vanish separately we obtain

$$\frac{\partial C_i(s)}{\partial s} + \lambda_i^2 C_i(s) - R_i(s) = 0. \tag{5.42}$$

From the form of $\mathscr{R}(\xi, s)$ it follows that $R_i(s) = \alpha_i f_0 e^{\sigma s}$ with some purely numerical prefactors α_i, so we expect $C_i(s) \propto p_i e^{\sigma s}$ and find

$$p_i = \frac{\alpha_i f_0}{\sigma + \lambda_i^2}. \tag{5.43}$$

Finally, we determine the α_i by reconsidering Equation 5.40. We multiply both sides by $\xi^2 H_j(\xi)$, where $H_j(\xi)$ is one specific but arbitrary eigenfunction of the homogeneous problem, and then integrate over the whole volume V. Due to the orthogonormality of the eigenfunctions we obtain

$$\alpha_j = \int \frac{1}{1-\rho}\left(3 - \frac{2\rho}{\xi} - \sigma\left(\frac{1}{2}\xi^2 - \rho\xi + g_0\right)\right)\xi^2 H_j(\xi) d\xi, \tag{5.44}$$

and all the α_i can be calculated explicitly. Thus, the full solution of the linear problem is

$$c(\xi, s) = \sum_{i=1}^{\infty}\left(h_i e^{-\lambda_i^2 s} + \frac{\alpha_i f_0}{\sigma + \lambda_i^2} e^{\sigma s}\right) H_i(\xi) + \frac{1}{1-\rho}\left(\frac{1}{2}\xi^2 - \rho\xi + g_0\right) f_0 e^{\sigma s}. \tag{5.45}$$

The constant g_0 can now be calculated from the requirement that $\int c(\xi, s=0) dV = N_0$. Here we make use of the fact that $\int H_i(\xi)\xi^2 d\xi = 0$ if λ_i satisfies Equation 5.34, thus

$$g_0 = \frac{\frac{(1-\rho)}{\sigma} - \frac{1}{10} + \frac{1}{4}\rho + \frac{1}{10}\rho^5 - \frac{1}{4}\rho^5}{\frac{1}{3}(1-\rho^3)}. \tag{5.46}$$

a	radial coordinate of apical tissue surface
b	radial coordinate of basal tissue surface
c	nuclear concentration
$c_{\max}$, $c^*_{\max}$	maximum nuclear concentration and optimal $c_{\max}$-value
D, D_{lin}, D_{nonlin}	diffusion constant, D linear model, D nonlinear model
D^*, D^*_{lin}, D^*_{nonlin}	optimal D-value, D^* linear model, D^* nonlinear model
D_{thermal}	diffusion constant in case of thermal diffusion
D_{tube}	diffusion coefficient of a rigid particle within a narrow, fluid-filled membrane tube
F_{external}	force due to an external potential
F_{friction}	friction (force)
$\mathscr{F}$	stochastic force
k_{B}	Boltzmann constant, 1.38×10^{-23} $\text{m}^2\text{kg/s}^2\text{K}$
m	mass of the particle
N_0	initial number of tracked nuclei
n	index of steps in Markov chain during simulation
p	substituted variable for integration
Q	correlation function of the stochastic noise
q	substituted variable for integration
R	(average) nuclear radius
r	radial coordinate of the tissue
S	apical tissue surface area
T	temperature
t	(experimental) time
U_{external}	external potential
$\widetilde{\Delta W}$	normally distributed random variables, mean zero, variance 1
x	generic spatial variable
Y	step in Markov chain during simulation
Γ	integral over the correlation function of the stochastic noise
Γ_{IKNM}	Γ in the specific case of IKNM
Γ_{thermal}	Γ for thermal diffusion
γ, γ_{Stokes}	friction coefficient, Stokes' friction coefficient
γ_{tube}	friction coefficient of a particle within a narrow, fluid-filled membrane tube
η	viscosity (of water), 8.90×10^{-4} Pa·s at 25 °C, 7.97×10^{-4} Pa·s at 30 °C
κ	bending rigidity of the cell membrane
μ	chemical potential
σ	surface tension of the cell membrane
τ	average cell cycle time $/\ln 2$

Chapter 6

From many to one - single cell IKNM

Michael E. Cates (Department of Applied Mathematics and Theoretical Physics, University of Cambridge) suggested the Langevin model based on the chemical potential of the lattice gas leading to the additional, external force. Julius B. Kirkegaard (Niels Bohr Institute, University of Copenhagen) suggested the Euler–Maruyama method for the numerical solution of stochastic differential equations. Except for collaborations with my Supervisor Raymond E. Goldstein, specifically relating to the interpretation of the nuclear diffusion constant and the calculation of the stochastic driving force at low concentrations, the remainder of the work presented in this Chapter is my own.

6.1 Introduction

In the previous Chapter 5 we examined IKNM on the tissue level. Our results indicate that the high nuclear density within the retina plays a major role in determining the distribution of nuclei along the apicobasal axis of the tissue over time. Therefore, we should expect the nuclear density to influence the individual nuclear motilities and trajectories as well. Hence, in this Chapter, we investigate the effects of the nuclear packing on the scale of individual nuclear movements.

We begin by interpreting the exact value of the diffusion constant D^*_{nonlin}, as obtained in Chapter 5, microscopically in Section 6.2. Then, in Section 6.3, we develop two possible Langevin equations for describing the movement of individual nuclei within the crowded environment of the retial tissue. We use these equations to simulate the trajectories of individual nuclei in Section 6.4. These simulations provide a basis to analyse whether the nonlinear model developed in Chapter 5 can also recapitulate the properties of individual

nuclear trajectories in addition to capturing the changes in the nuclear concentration profile over time. Furthermore, the results of our simulations enable us to discriminate between the two possible Langevin equations. By comparing the simulation outcome to the experimental data (see Chapter 4), we are able to make some predictions about possible microscopic mechanisms underlying the nuclear movements in IKNM.

6.2 Interpretation of the diffusion constant

In this Section we set out to tackle one of the questions raised at the end of Chapter 5 - interpreting the scale of the diffusion constant obtained there, $D^*_{\text{nonlin}} \sim 0.1\ \mu\text{m}^2/\text{min}$. In order to do so, we first examine the aforementioned correspondence between the two previously derived models for tissue level IKNM (compare Chapter 5) in closer detail in Subsection 6.2.1. This correspondence allows us to make use of the well known properties of diffusion (as described in Chapter 3) to interpret D^*. We first ask whether the value of D^* can be due to free (thermal) diffusion at all in Subsection 6.2.2. As this is not the case, we discuss possible properties of the retinal tissue which could influence the mobility of the nuclei independently of their own packing density in Subsection 6.2.3. We identify the slender geometry of each cell, with the cell membrane bulging around the nucleus (compare Chapter 2), as one of the possible reasons. The tight association between nucleus and cell membrane is likely to affect the mobility of the nucleus and we inspect this effect in Subsection 6.2.4. In doing so, we reveal that the movements of individual nuclei likely need to be driven by additional forces other than thermal motion throughout the whole cell cycle in the zebrafish retinal system. We estimate the strength of these additional forces in Subsection 6.2.5 before finally considering whether the origin of these forces might be cytoskeletal in Subsection 6.2.6.

6.2.1 Correspondence of the two tissue level models

In order to understand the exact value of the diffusion constant as obtained from the nonlinear model, $D^*_{\text{nonlin}} = (0.09 \pm 0.05)\ \mu\text{m}^2/\text{min}$, we reconsider the two models described in Chapter 5. In the linear model, we used the well-known equation for thermal diffusion (as introduced in Chapter 3)

$$\frac{\partial c}{\partial t} = D_{\text{lin}} \frac{1}{r^2} \frac{\partial}{\partial r} \left(r^2 \frac{\partial c}{\partial r} \right) = \frac{1}{r^2} \frac{\partial}{\partial r} \left(D_{\text{lin}} r^2 \frac{\partial c}{\partial r} \right) \tag{6.1}$$

while for the nonlinear model we derived

$$\frac{\partial c}{\partial t} = D_{\text{nonlin}} \frac{1}{r^2} \frac{\partial}{\partial r} \left(r^2 \frac{c_{\max}}{c_{\max} - c} \frac{\partial c}{\partial r} \right) = \frac{1}{r^2} \frac{\partial}{\partial r} \left(D_{\text{nonlin}} \frac{c_{\max}}{c_{\max} - c} r^2 \frac{\partial c}{\partial r} \right). \tag{6.2}$$

As can be seen by comparing the right hand sides of Equations 6.1 and 6.2, the diffusion constant D_{lin} in Equation 6.1 corresponds to the expression $D_{\text{nonlin}} c_{\max} / (c_{\max} - c)$ in Equation 6.2. This correspondence was already addressed in the discussion in Chapter 5, as it is likely to be the reason why we obtained different values for D^*_{lin} and D^*_{nonlin}.

At low nuclear densities, $c \to 0$, the term $c_{\max} / (c_{\max} - c)$ in Equation 6.2 tends to 1. Therefore, as $c \to 0$, we recover the (free) thermal diffusion equation 6.1 with $D^*_{\text{lin}} = D^*_{\text{nonlin}} = (0.09 \pm 0.05)$ µm^2/min and can thus make use of its well-known properties for further evaluation.

6.2.2 Are nuclei moving due to free thermal diffusion?

Assuming $c \to 0$ in the following, first of all we can assess whether nuclei in IKNM move due to thermal diffusion. If this was the case, and if they were moving freely without any constraints, the diffusion constant would obey the Stokes-Einstein Equation 3.2 [114], where η is the viscosity of the medium within which the nuclei move and R is the average radius of the nuclei now. Here we assume that the viscosity of the cytosol is equal to the viscosity of water. Thus, if the nuclei were spherical with a radius $R = 3.5$ µm, corresponding to the maximum nuclear concentration $c^*_{\max} = 4.12 \times 10^{-3}$ µm^{-3} obtained in Chapter 5, their (free) thermal diffusion constant would be $D_{\text{thermal}} \approx 4.20$ µm^2/min to 4.77 µm^2/min. This is about 50 times larger than the obtained value D^*_{nonlin}, meaning freely diffusing nuclei should be more mobile than seen during IKNM.

6.2.3 Factors restricting the nuclear movements within a cell

As D^*_{nonlin} is much smaller than D_{thermal}, there must be certain physical properties of the retinal tissue that are in fact restricting the mobility of the nuclei. Two possible properties restricting the nuclear movement might be the viscosity of the cytoplasm and the slender shape of the individual cells within pseudostratified epithelia (compare e.g. [84]). The former might in fact be much higher than the viscosity of water assumed above due to the high number of organelles and other components present in the cytosol, leading to a lower actual value of D_{thermal}. The latter might mean that a considerable amount of energy is required for

cell membrane deformations in line with the nuclear movements and for moving the cytosol past the moving nucleus, restricting the nuclear movements in IKNM.

6.2.4 Does the cell membrane presence explain nuclear mobility?

Recently, Daniels [147] considered effects similar to the second one addressed above and showed the thermal diffusion constant of a solid particle moving within a thin, fluid-filled membrane tube to be

$$D_{\text{tube}} = \frac{1}{32}\left(\frac{\kappa R^2 \sigma}{(k_{\text{B}}T)^2}\right)^{-2/3} D_{\text{thermal}} \tag{6.3}$$

where κ is the bending rigidity and σ the surface tension of the membrane.

Under the assumption that the PSE cells are locally approximately cylindrical, using typical values for κ and σ as given by Daniels [147] yields $D_{\text{tube}} \approx \left(9.5 \times 10^{-7}\right) D_{\text{thermal}}$ to $\left(4.5 \times 10^{-6}\right) D_{\text{thermal}}$. However, these values are now about 3 to 4 magnitudes smaller than D^*_{nonlin} without even considering deviations in the cytoplasmic viscosity from the viscosity of water, which would decrease the value of the nuclear diffusion constant even more. These results strongly suggest that the nuclear movements in IKNM cannot be due to thermal diffusion alone. Instead, nuclei appear to be actively driven, e.g. due to cytoskeletal transport.

6.2.5 Towards the strength of the driving force in IKNM

Further evaluation of the nuclear movements at low densities can be used to determine the (average) strength of the additional driving force implied above. In order to do so, we utilise the Langevin formalism describing the random movements of individual Brownian particles introduced in Chapter 3.

The integral in Equation 3.9 can be solved assuming that $\langle \mathscr{F}(t')\mathscr{F}(t'')\rangle$ is a fast decaying function $Q(t'-t'')$. With $q = t'-t''$ and $p = t'+t''$

$$\left\langle r^2(t)\right\rangle = \frac{1}{\gamma^2}\frac{1}{2}\int_0^{2t} dp \int_{-\infty}^{\infty} dq Q(q). \tag{6.4}$$

Now $\int_{-\infty}^{\infty} dq Q(q) = \Gamma$ is just a number and we obtain

$$\left\langle r^2(t)\right\rangle = \frac{1}{\gamma^2}\frac{1}{2}\int_0^{2t} dp\Gamma = \frac{1}{\gamma^2}\Gamma t. \tag{6.5}$$

For thermal diffusion in 3 dimensions we further know that $\left\langle r^2(t)\right\rangle = 6Dt$. Therefore we obtain

$$\Gamma = 6\gamma^2 D. \tag{6.6}$$

In the Stokes regime, where

$$F_{\text{friction}} = \gamma_{\text{Stokes}}\frac{\partial r}{\partial t} = 6\pi\eta R\frac{\partial r}{\partial t} \tag{6.7}$$

and knowing the Stokes-Einstein Equation 3.2 we thus deduce $\Gamma_{\text{thermal}} = 6\gamma_{\text{Stokes}}k_{\text{B}}T$.

This equation might not hold true for nuclear movements in IKNM. On the one hand, the friction a nucleus experiences during IKNM can be expected to be larger than the Stokes friction γ_{Stokes} due to the presence of the cell membrane (even when assuming the viscosity of water for the cytosol). According to Daniels [147] the friction coefficient of a rigid particle moving within a fluid-filled, narrow membrane tube is $\gamma_{\text{tube}} = 32\left(\kappa R^2\sigma/\left(k_{\text{B}}T\right)^2\right)^{2/3}\gamma_{\text{Stokes}}$. On the other hand, we already showed that $D^*_{\text{nonlin}} \neq D_{\text{tube}}$. However, we can make use of the expression for γ_{tube} and of the obtained value for D^*_{nonlin} to to estimate the value of Γ_{IKNM} and the average strength of the driving force. We modify Equation 6.6 accordingly

$$\Gamma_{\text{IKNM}} = 6\gamma^2_{\text{tube}}D^*_{\text{nonlin}} \tag{6.8}$$

and hence determine $\Gamma_{\text{IKNM}} \approx 1.25\times10^{-18}$ N^{2}s to 3.43×10^{-17} N^{2}s.

6.2.6 The characteristic stochastic force

Having obtained an estimate for Γ_{IKNM}, we finally divide Γ_{IKNM} by a characteristic time in the IKNM system and take the square-root of the result to obtain the typical (average) strength of the stochastic force. Assuming a characteristic time to be of the order of 10 ms to 1 s, corresponding to the time scale of many cytoskeletal molecular processes like the addition of monomers to a growing microtubule filament or the stepping of molecular motors [148], we obtain typical forces of approx. 1.12 nN to 58.56 nN. This result is compatible with cytoskeletal transport under the assumption that a single nucleus is transported by multiple molecular motors at once or alternatively is moved by polymerising cytoskeletal filaments,

as both processes exert forces that are of the order of a few pN [149] [150].

6.3 Langevin models for IKNM in a crowded environment

In the previous Section we have used of the correspondence between the nonlinear diffusion Equation 6.2 and thermal diffusion (Equation 6.1) to interpret the value of the diffusion constant D^*_{nonlin}. Accordingly, we have assumed $c \to 0$ so far. However, as mentioned before, the results from Chapter 5 indicate that the nuclear density also influences the individual nuclear movements. In this Section, we thus employ the results obtained in Section 6.2 to devise possible Langevin equations describing the dynamics of the movements of individual nuclei for high nuclear packing. We envisage two different possibilities (in Subsections 6.3.1 and 6.3.2, respectively, and a combination of both in Subsection 6.3.3) to generate a Langevin equation for nuclei moving according to the nonlinear model in Equation 6.2. The first possibility is to create a direct extension of the above described low-c-regime Langevin model. The second possibility is to incorporate the effects of the high nuclear concentration by including an additional external force, as in Equation 3.4. Based on these two approaches and the experimental data, simulations presented in Section 6.4 will probe the nature of the c-influence on the movements of individual nuclei in IKNM.

6.3.1 A direct extension of low concentration considerations

In the previous Section 6.2 we have discussed that nuclei moving during IKNM might be subject to much larger friction than freely diffusing nuclei due to the presence of the cell membranes, such that we assume the nuclear friction coefficient to be γ_{tube}, rather than γ_{Stokes}. Furthermore we have demonstrated that, in order to explain the obtained diffusion coefficient D^*_{nonlin}, we need to assume the stochastic forces acting on the nuclei to be different from those in thermal diffusion. We have obtained a possible expression for these stochastic forces, equation 6.8. Finally, at the beginning of Section 6.2, we have shown that the two expressions D_{lin} and $D_{\text{nonlin}} c_{\max} / (c_{\max} - c)$ correspond to each other and D_{lin} and D_{nonlin} are equal when $c \to 0$.

Here, we combine all these insights and envisage that the nonlinear model might correspond to the same Langevin equation as thermal diffusion (Equation 3.6) - and hence as the low-c-case - but with different expressions for D and Γ due to the high nuclear concentration.

Using γ_{tube}, Equation 6.6 and the correspondence of D_{lin} and $D_{\text{nonlin}} c_{\max}/(c_{\max}-c)$ we obtain the first possible Langevin model for the movements of individual nuclei

$$\begin{aligned} \gamma &= \gamma_{\text{tube}} = 32 \left(\frac{\kappa R^2 \sigma}{(k_{\text{B}}T)^2} \right)^{2/3} \gamma_{\text{Stokes}} \\ D &= D^*_{\text{nonlin}} \frac{c_{\max}}{c_{\max}-c} \\ \Gamma &= 6\gamma^2 D = 6\gamma^2_{\text{tube}} D^*_{\text{nonlin}} \frac{c_{\max}}{c_{\max}-c}. \end{aligned} \tag{6.9}$$

The advantage of this model is its smooth convergence to the low density model described in Section 6.2 as $c \to 0$. However, here Γ and thus $\mathscr{F}$ vary with c. Regarding the biological interpretation, it is not immediately clear why and how the stochastic noise should vary in strength depending on the nuclear concentration; although several possible explanations come to mind. For example, the stochastic forces exerted on each nucleus might result from cytoskeletal components transporting the nuclei back and forth. The strength of this transport could vary depending on the nuclear density within the tissue, e.g. due to more molecular motors being recruited with increasing nuclear density.

6.3.2 An external force based on the nuclear concentration

Focussing on the possibility of interactions between the individual nuclei as an influence factor, we can also devise a second, different Langevin model for the nuclear movements in IKNM. As pointed out in Chapter 3, an additional external force F_{external} can act on the moving particle (compare Equation 3.4). If F_{external} is a conservative force, than $F_{\text{external}} = -\nabla U_{\text{external}}$ where U_{external} is an external potential. Here U_{external} could be the chemical potential μ which the nuclei are subject to due to the presence and distribution of the other nuclei around them. As the concept of the lattice gas was underlying the derivation of the nonlinear diffusion model in Equation 6.2 (compare Chapter 5), we here choose the lattice gas chemical potential, given by Equation 3.15, as our expression for μ. Thus we obtain

$$-\nabla\mu = -\frac{\partial\mu}{\partial c}\frac{\partial c}{\partial r} = -k_{\text{B}}T \frac{1}{c}\frac{c_{\max}}{c_{\max}-c}\frac{\partial c}{\partial r} \tag{6.10}$$

and

$$\gamma\frac{\partial r}{\partial t} = -k_{\text{B}}T \frac{1}{c}\frac{c_{\max}}{c_{\max}-c}\frac{\partial c}{\partial r} + \mathscr{F}. \tag{6.11}$$

In this model, we keep the strength of the stochastic force, and thus Γ, independent of the nuclear concentration c and hence use Equation 6.6 with

$$\begin{aligned} \gamma &= \gamma_{\text{tube}} = 32 \left(\frac{\kappa R^2 \sigma}{(k_{\text{B}} T)^2} \right)^{2/3} \gamma_{\text{Stokes}} \\ D &= D^*_{\text{nonlin}} \\ \Gamma &= 6\gamma^2 D = 6\gamma^2_{\text{tube}} D^*_{\text{nonlin}}. \end{aligned} \tag{6.12}$$

Regarding the biological interpretation, this model might be seen as advantageous as the meaning of μ is clear and we keep Γ constant. A constant value of Γ would result for example if the stochastic force $\mathscr{F}$ was exerted on the nuclei by molecular motors transporting the nuclei along cytoskeletal components and this transport process itself was independent of the nuclear concentration c. However, for the model introduced here it is not immediately clear how it converges to the one described in Section 6.2 as $c \to 0$. Specifically, the term $(1/c)(c_{\max}/(c_{\max} - c)(\partial c)/(\partial r)$ would have to vanish. Since $(1/c)$ becomes large and $(c_{\max}/(c_{\max} - c)$ goes to 1 as $c \to 0$ we thus have to require that $(\partial c)/(\partial r)$ becomes zero at low nuclear concentrations to ensure correspondence between the high and low nuclear density cases.

6.3.3 A combination of both models

Finally, we can also imagine that the correct Langevin model corresponding to Equation 6.2 could be a combination of the above two models, Equations 6.9 and 6.12. This means a high nuclear concentration might lead to interactions between the nuclei in the sense of the second model but also change the number of molecular motors recruited to the nucleus, corresponding to an increase in Γ as in the first model.

However, it will become clear from the results presented in the following Section 6.4 that simulating this combined model would likely not be worthwhile when aiming to understand the possible mechanisms underlying IKNM, because we would not be able to distinguish it from the model in Equation 6.9.

6.4 Simulation of individual nuclear trajectories

Having developed Langevin models to describe the movements of individual nuclei during IKNM in the previous Sections 6.2 and 6.3, we now proceed to solve these equations numerically, i.e. to simulate the trajectories of individual nuclei. Here, we present simulations of three different models:

- the model with c-dependent Γ described in Equation 6.9
- the model with c-dependent external force F_{external} described in Equation 6.12
- the low concentration model derived in Section 6.2 with Γ as in Equation 6.8 for comparison.

As mentioned above, simulating a model that combines the two approaches used in Equations 6.9 and 6.12 will not be fruitful.

The simulations in this Section are based on the Euler-Maruyama method (compare Chapter 3), as detailed in Subsection 6.4.1. In addition to the underlying Langevin equations, the boundary conditions for these simulations also need to be specified (see Subsection 6.4.2). As the numerically produced nuclear trajectories are supposed to be as realistic as possible, we take the experiments into account when setting up the simulations. Therefore, we initialise nuclei in the simulations at the exact times their real counterparts came into being (due to cell divisions) in the experiment. Consequently, we focus only on nuclei for which tracking data is available beginning right from cell division. Additionally, we require nuclei to have occured early enough in the experiment that the tracking data covers a substantial part of the cell cycle while still lying within the first 200 min of experiments (corresponding to the time frame used for D-optimisation in Chapter 5). In Subsection 6.4.4 we further specify the selection of nuclei to be simulated. Creating the one-to-one correspondence between real and simulated nuclei allows us to simulate each nucleus in the exact environment, i.e. the exact concentration profile of surrounding nuclei, it would experience in the real tissue. To this end we utilise a spatially continuous approximation of the nuclear concentration profile obtained in Chapter 5 in most simulations, as outlined in Subsection 6.4.3. As the underlying equations are stochastic differential equations, any single run of the simulations cannot be expected to recreate the experimental nuclear trajectories. Hence we repeat the simulations multiple times, as described in Subsection 6.4.6, and use mean-squared-displacement (MSD) curves to compare simulation outcomes and experiments (compare Subsection 6.4.5). We further validate the numerical results by performing simulations with changed numbers of runs and time steps (see Subsection 6.4.7) and by employing a different method to adapt the nuclear concentration profile to the fact that nuclear trajectories are spatially continuous

(see Subsection 6.4.9). Comparing numerical and experimental results in Subsection 6.4.8, we find that we can distinguish between the three above mentioned models based on the generated MSD curves. Out of these models, only the one with c-dependent Γ matches the experimental curve from the main data set. This means the simulations and comparison to experiments allow us to predict microscopic mechanisms of IKNM on the basis of the most likely Langevin equation. Finally, we briefly address the case of the other data sets and the potential to study the time evolution of nuclear dynamics based on the simulations presetend here in Subsections 6.4.10 and 6.4.11, respectively.

Although we are taking the nuclear concentration profile surrounding each nucleus into account, the simulation only concerns a single nucleus at any given time. Therefore, we here assume a 1-dimensional geometry in which each nucleus moves along the apicobasal axis of its respective cell.

Unless stated otherwise, all simulations are performed using custom Python 3 [151] routines.

6.4.1 Time discretisation

In order to solve the three different Langevin models for nuclear movements during IKNM numerically, we employ the Euler-Maruyama method introduced in Chapter 3. Thus, in general terms, Equation 3.27 here becomes

$$Y_{n+1} = Y_n + \frac{F_{\text{external}}}{\gamma_{\text{tube}}}\Delta t + \frac{\sqrt{\Gamma}}{\gamma_{\text{tube}}}\sqrt{\Delta t}\widetilde{\Delta W_n} \tag{6.13}$$

where we define $\sqrt{\Delta t}\widetilde{\Delta W_n} = \Delta W_n$, i.e. $\widetilde{\Delta W_n}$ are normally distributed random variables with mean zero and variance 1.

More specifically speaking, we have

$$Y_{n+1} = Y_n + \sqrt{6D^*_{\text{nonlin}}}\sqrt{\Delta t}\widetilde{\Delta W_n} \tag{6.14}$$

in the low-c case,

$$Y_{n+1} = Y_n + \sqrt{6D^*_{\text{nonlin}} c_{\max}/\left(c_{\max} - c\right)}\sqrt{\Delta t}\widetilde{\Delta W_n} \tag{6.15}$$

in the case of c-dependent Γ and

$$Y_{n+1} = Y_n - \left(\frac{k_B T}{\gamma_{\text{tube}}} \frac{c_{\max}}{c\,(c_{\max} - c)} \frac{\partial c}{\partial r} \right) \Delta t + \sqrt{6 D^*_{\text{nonlin}}} \sqrt{\Delta t} \widetilde{\Delta W_n} \tag{6.16}$$

in the case of c-dependent F_{external}.

6.4.2 Boundary conditions

In addition to the mechanism of time-discretisation, a second, important point to consider for the simulations is the correct implementation of the boundary conditions. In Chapter 5 we found

$$D \frac{c_{\max}}{c_{\max} - c} \frac{\partial c}{\partial r}\bigg|_{r=a} = \frac{N_0}{S\tau} e^{t/\tau} \tag{6.17}$$

apically and

$$\frac{\partial c}{\partial r}\bigg|_{r=b} = 0 \tag{6.18}$$

basally.

Here, in contrast to the work presented in Chapter 5, we do not need to take the nuclear influx through the apical surface of the tissue into account, as each simulation only represents a single nucleus. The changes in the surrounding nuclear concentration are instead included via the c-dependent terms in Equations 6.15 and 6.16.

However, the simulations need to preserve the fact that nuclei cannot leave the tissue, i.e. the domain $b \leq r \leq a$. In fact, due to the nuclear size, the nuclear position (which describes the position of the centre of mass of a nucleus) should not get closer than a few µm to the tissue surfaces. In the simulations, we choose to encode this condition explicitely, as outlined in the following.

If a simulation step were to move a nucleus closer to a tissue boundary than 3 µm - corresponding roughly to the exclusion width of 3 to 4 µm established in Chapter 5, or the nuclear radius of $R = 3.5$ µm used for the calculations in Section 6.2 - or even outside the tissue, the simulation positions the nucleus back into the tissue before the next step. For this repositioning, we let the nucleus move as far as it can towards the tissue boundary (i.e. up to 3 µm away) and then, instead of moving it further, we let it move back away from

the boundary by the rest of the total distance it was supposed to migrate. In addition, we also start each nuclear simulation 3 µm away from the apical boundary, such that nuclei are actually created inside the tissue.

With regard to possible other choices for implementing the boundary conditions, we have to take biological, numerical and physical considerations into account.

From a biological point of view, we could have also chosen to move the nucleus only as far as possible towards a cell surface and then let it remain at this position. It is not *a priori* clear which one of these choices represents the actual biology inside a cell more acurately, or if either one does at all. We can envisage a nucleus being transported by a multitude of motor proteins walking simultaneously in different directions along the length of the cell and in doing so moving the nucleus in a tug-of-war like fashion. In this case, it might well be that the motors also reach the end of the cytoskeletal filaments to walk on when the nucleus cannot move further due to the presence of the cell surface. Then, motors attempting to move the nucleus in the oposite direction at the same time might take over and transport the nucleus away from the boundary again (although it would not clear by how much). On the contrary, we can also envisage the nucleus being pushed from the back by growing cytokeletal filaments (compare e.g. [149]). In this case, there doesn't seem to be a reason why the pushing force should cease to exist when the nucleus cannot move further; unless the cytoskeletal filaments were inhibited from growing longer or started shrinking once nuclear movements arrest.

However, while the microscopic biological situation might not be entirely clear, there are good physical and computational reasons for the procedure we choose.

Most importantly, by moving the nucleus back into the tissue by the exact distance it was supposed to migrate past the boundary, we realise the no-flux conditions at both tissue surfaces. Using the method of mirror images we imagine a 'mirror nucleus' with the exact same but mirrored trajectory as the nucleus of interest (note that we assume a locally 1-dimensional approximation of the tissue geometry as we consider nuclear trajectories along the apicobasal cell axis only). In this picture, if the nucleus of interest moves outside the allowed domain $b \leq r \leq a$, the mirror nucleus simultaneously moves into this domain. The mirror nucleus here reaches the exact distance for the tissue surface that the original nucleus were to migrate away from this boundary outside the cell.

Furthermore, by moving a nucleus back into the cell when it leaves the domain $b \leq r \leq a$ during a simulation step, we hope to ensure that nuclei do not artificially get stuck on the tissue surfaces. That is, if a nucleus is positioned away from a boundary, it can move in both directions in the next time step of the simulations. In contrast this nucleus would not be able to move at all in 50% of the cases if it were to remain directly on a simulation boundary.

Similarly, choosing to move a nucleus back away from the boundary by the exact distance it was to move outside the cell, as opposed to e.g. letting this nucleus move back to the exact position it last came from, shall avoid that nuclei get stuck at a specific distance away from the tissue surface.

Finally, from a biological point of view, the possibility of moving a nucleus back to the exact position it last came from leads to nuclei phenomenologically behaving like elastically bounced off the cell membrane. Given that cellular components are highly viscoelastic (compare e.g. [152] [18]) this appears unlikely to happen in a real biological system.

6.4.3 Adapting the nuclear concentration profile

As is apparent from the Equations 6.15 and 6.16, the nuclear concentration profile $c(r,t)$ and its gradient $\partial c(r,t)/\partial r$ are required for simulating nuclear trajectories at high nuclear density.

$c(r,t)$ and $\partial c(r,t)/\partial r$, together with D^*_{nonlin} and c^*_{max}, can be extracted from the nonlinear model presented in Chapter 5. However, as we have solved the nonlinear model (based on Equation 6.2) numerically, the values of $c(r,t)$ and $\partial c(r,t)/\partial r$ are only available at discrete values for r and t.

This is not a problem in the case of the time variable t, as the simulations presented here are discrete in time as well. Thus, we only need to extract the concentration profile $c(r,t)$ and its gradient for each value of t we wish to include in the simulations. Since the MATLAB solver pdepe chooses the steps for the time integration dynamically and the user provided time meshpoints only specify the values of t for which the concentration profile is being output [140], we expect the numerical solution of Equation 6.2 to be independent of the time step Δt we choose here.

In contrast, pdepe does not select the spatial meshpoints for the integration automatically [140]. Therefore, we have to be consistent in providing the spatial mesh to ensure the same

solution of Equation 6.2 is being output each time.

Even more importantly, in contrast to the time variable, the spatial coordinate r is actually continuous rather than discrete in the simulations of nuclear trajectories. This poses a challenge when wishing to utilise the (spatially discrete) solution $c(r,t)$ obtained in Chapter 5 for the simulations here. In order to minimise deviations of the simulated nuclear trajectories from real ones and to obtain an understanding of the potential effect of the descrete r in the $c(r,t)$ calculation on the simulated trajectories, we take the following approach:

- All simulations of nuclear trajectories are continuous in space in order to avoid the introduction of deviations from the true solution X of Equation 3.26 by introducing a spatial discretisation.
- For all simulations of nuclear trajectories performed in Python (i.e. the majority of the simulations presented here), we provide $c(r,t)$ and its gradient using the exact same spatial mesh as in Chapter 5, that is $\Delta r = 0.5$ µm. To this end, the solution of Equation 6.2 is obtained using the MATLAB [127] routine described in Chapter 5 with the exact time step Δt required for each given trajectory simulation. The resulting $c(r,t)$ and $\partial c(r,t)/\partial r$ are imported into the Python 3 routine at the start of a simulation. $c(r,t)$ and $\partial c(r,t)/\partial r$ are not being updated throughout the simulations.
- In the simulations described above, in case a nuclear position coincides with one of the spatial meshpoints for which $c(r,t)$ and its gradient have been provided, the provided values are being used to calculate the next step of the Markov chain, i.e. Y_{n+1} in Equation 6.13.
- In the simulations described above, in case a nuclear position does not coincide with any spatial meshpoint at which $c(r,t)$ and its gradient have been provided, the values of $c(r,t)$ and $\partial c(r,t)/\partial r$ are being averaged over the two nearest meshpoints and these averages are being used to calculate the next step of the Markov chain, i.e. Y_{n+1} in Equation 6.13.
- A control simulation is being performed using a custom MATLAB [127] routine which re-evaluates $c(r,t)$ and $\partial c(r,t)/\partial r$ based on a nucleus' actual position at each time step - in contrast to the Python 3 [151] routine described above. In this case, the solution of Equation 6.2 is being re-calculated each time using almost the same mesh as in Chapter 5 ($\Delta r = 0.5$ µm) but with the addition of the nucleus' actual position as an extra meshpoint. We compare the results to the simulations performed in Python in Subsection 6.4.9.

6.4.4 The nuclear birth time distribution

With the simulation of nuclear trajectories, we aim to reproduce the experimental situation as realistically as possible. Therefore, we wish to establish a one-to-one correspondence between simulated and real nuclei. In order to do so, we need to select those nuclei which are well-suited for simulations from the experimental data.

For the simulations presented here, we focus on nuclei for which tracking data is available beginning directly with cell division, because for those nuclei we know both the initial position (at the apical tissue surface) as well as the cell cycle phase. Knowing the cell cycle phase is particularly relevant as the nonlinear model in Chapter 5 does not include the seemingly directed movements of nuclei in G2 phase.

Furthermore, we only take nuclei into account for which individual tracks (between two consecutive divisions) were at least 150 min long, to cover a substantial part of the cell cycle.

Cell division times, and thus nuclear birth times, are extracted from the full experimental tracks (compare Chapter 4) and we obtain the birth time distribution exemplified in Table 6.1. As shown by the data presented in this table, cell divisions are not distributed evenly throughout the experiment. Instead, during some experimental time steps no cell divisions took place and thus no nuclear births can be observed in the corresponding microscopy frame (e.g. there are no cell divisions in frame 3), while at other times multiple cell divisions happened simultaneously (e.g. two divisions in frame 2 and three divisions in frame 15). This exact distribution is reflected in our simulations.

Finally, for the simulations, we only consider the 40 first-born nuclei (in the case of the main data set) because all of those nuclei came into being less than 50 min into the experiment. Thus the first 150 min of their corresponding individual tracks all fall within the first 200 min of the experiment, the time covered by the D-optimisation in Chapter 5. This selection ensures that we know the surrounding $c(r,t)$ and $\partial c(r,t)/\partial r$ for the entire length of simulation.

6.4.5 On the use of mean-squared-displacement curves

As the equations underlying our simulations are stochastic differential equations and each step in the Markov chain in Equation 6.13 requires to generate a random number, we cannot expect

Table 6.1 **Example of nuclear birth times**. This table provides example data of cell division times observed in the main data set. Only nuclei fulfilling the criteria laid out in the main text have been considered. The numbering of nuclei is arbitrary. Each cell division results in the birth of two nuclei. Cell divisions are not synchronised or evenly distributed in the developing zebrafish retina. Therefore, in some microscopy frames no cell division could be observed while other frames showed several simultaneous cell divisions.

nucleus number	1	2	3	4	5	6	7	8	...	21	22	23	24	25	26	...
birth time [frame]	1	1	2	2	2	2	4	4	...	15	15	15	15	15	15	...
birth time [min]	2	2	4	4	4	4	8	8	...	30	30	30	30	30	30	...

any run of these simulations to produce a nuclear trajectory that matches the corresponding experimental one exactly, even when using the correct nuclear birth time, concentration profile, boundary conditions and Langevin model. Therefore, in order to enable comparisons between the experimental and simulated results, we calculate mean-squared-displacement (MSD) curves.

However, based on the results presented in Chapter 5 the usage of MSD curves should be reviewed cautiously. If interactions between the nuclei really played a role for their distribution across the retinal tissue during IKNM, as our work suggested, then the nuclear mobility would be density- (and hence location- and time-) dependent. In this case, nuclei born early in the experiment are thus expected to behave fundamentally different from nuclei born later. Consequently, nuclei with different birth times should not be clustered together e.g. for the purpose of producing a MSD curve. Instead, only nuclei born at the same time and thus experiencing the same environment should be clustered to calculate such a curve.

On the other hand, only clustering nuclei with similar birth times might create a statistical difficulty, because - as cell divisions are not synchronised in the retinal PSE tissue - a very large number of experimental tracks is necessary to ensure that enough simultaneous cell divisions can be observed. The scale of this problem becomes apparent when considering the main data set. Although all nuclei within a considerable part of the retina have been tracked, we seldomly observe more than a few cell divisions during the same experimental time step (compare Table 6.1).

Because of the small number of available experimental tracks that fulfil the criteria in Subsection 6.4.4, we thus proceed to merge all these tracks into one MSD curve despite the presumed concentration dependence of the nuclear mobility.

In order to circumvent any downsides this procedure might have, we subsequently process the simulated nuclear tracks in exactly the same way. This means we simulate the exact set of 40 nuclei selected from the experimental data as in Subsection 6.4.4 and then calculate the MSD curve from the 40 simulated trajectories.

For doing so, we transform nuclear position as a function of experimental time into nuclear position as a funtion of time after birth (equivalent to time after cell division) for each nucleus (both simulated and experimental). That means we substract each nucleus' individual birth time from the experimental time for each step of this nucleus' tracking data. Based on the so transformed individual track we compute the MSD curves in the usual way. These curves now represent the nuclear MSD as a function of time after birth, or cell-intrinsic time.

6.4.6 The simulations

As mentioned above, the stochastic nature of the models underlying the trajectory simulations means that these simulations might never reproduce the exact experimental trajectories. Employing MSD curves, this would not be a problem if we were able to simulate a very large number of nuclei. However, the required correspondence between simulations and experiments means that we can only merge 40 trajectories to calculate each MSD curve. Because of this limited number we expect the resulting MSD curves to differ between two repeats of the same simulation of the 40 selected nuclei.

Unfortunately, it is probably not possible to generate good statistics from the experiments in the case of single cell level IKNM. On the one hand, the number of selectable nuclei is finite in each retina, as discussed before. On the other hand, even if we were able to experimentally observe IKNM in a large number of retinas, the distribution of nuclear birth times exemplified in Table 6.1 and the nuclear concentration profile would most likely be different in each organism. Therefore, we here avoid clustering data from multiple organisms.

However, we are able to create good statistics in the artificial, simulated system by simply repeating the simulation of the exact same 40 selected nuclei many times. In each such run, we compute a MSD curve that is equivalent to the curve obtained from the experiment. By repeating the simulation often enough, we can gain an understanding for the range of values that the simulated MSD curve might cover. In the results presented in the following, each set of 40 nuclei simulations was repeated 2500 times, resulting in 2500 MSD curves

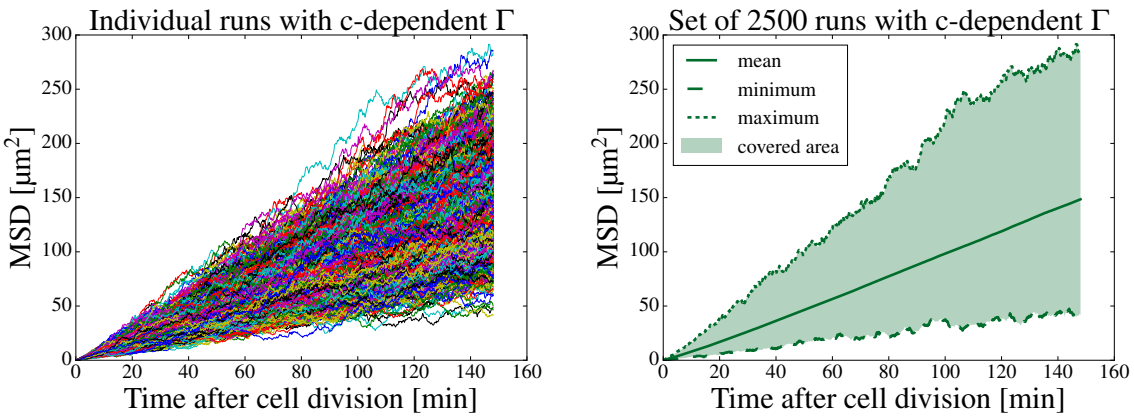

(a) (b)

Figure 6.1 **The distribution of simulated MSD curves.** This figure shows how we obtain the distribution of MSD curves used for comparisons between the models and between simulations and experiments in the following. (a) The 40 nuclei selected from the experiment are simulated and a MSD curve as a function of time after cell division, or cell-intrinsic time, is calculated from the resulting trajectories (compare Subsection 6.4.4). This procedure is repeated 2500 times. Each curve in this plot represents one such MSD curve. Here, the model with c-dependent Γ and a time step $\Delta t = 0.2$ min are used. (b) The distribution of the MSD curves shown in (a). The solid line represents the mean (as a function of time after cell division) of all the 2500 curves in (a), the dotted line their maximum and the dashed line their minimum. The shaded area represents the range of values covered by the curves in (a), i.e. the area in the plot between maximum and minimum curve. Mean, maximum and minimum have been calculated pointwise and thus do not represent actual MSD curves from the simulations.

as demonstrated in Figure 6.1 (a). Usually, the mean, minimum and maximum of all 2500 simulated MSD curves are extracted as functions of time (see Figure 6.1 (b)).

6.4.7 Robustness of simulation results

Before we compare the simulation results between different models or compare the simulations with the experiment, we first test the robustness of the simulation outcomes.

In order to do so, we repeat each 2500-runs-set using the same model and the same time step Δt three times. Each repeat results in a distribution of the respective 2500 MSD curves as shown in Figure 6.2 (a). We can thus compare these three distributions between each other. While we compare the distributions qualitatively based on their mean, maximum and minimum curves in Figure 6.2 (a), we can make a quantitative statement about

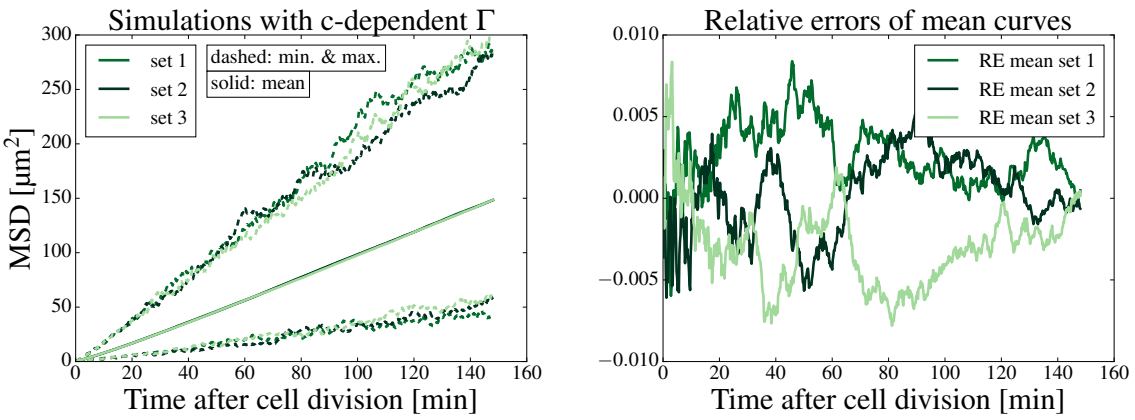

(a) (b)

Figure 6.2 **The robustness of simulation results.** We test the robustness of the simulation results by repeating a 2500-runs-set of the same simulation three times. Each repeat results in a distribution of MSD curves as presented before, with respective mean, maximum and minimum curves. (a) Comparison of the MSD curve distributions between the three repeats. The solid lines depict the means and the dashed lines the maxima and minima (as functions of time after cell division). Each colour represents one 2500-runs-set. Here, the model with c-dependent Γ and a time step $\Delta t = 0.2$ min are used. (b) Assuming the mean of all 7500 MSD curves from the three repeat sets to be the true mean curve, we calculate the relative errors (RE) of each individual 2500-runs mean with respect to the 7500-runs mean. Thus, $\mathrm{RE} = (\mathrm{mean}(2500\mathrm{runs}) - \mathrm{mean}(7500\mathrm{runs}))/\mathrm{mean}(7500\mathrm{runs})$. As the two plots show, 2500 runs of the simulation are sufficient to produce robust outcomes with respect to the distribution of MSD curves.

the robustness of the three mean curves. To this end, we calculate the mean curve of the total 7500 MSD curves and assume the result to be the true mean. This approach appears justified as the means of each of the three 2500-run-sets vary very little between each other. Then we calculate the error of each 2500-runs-mean relative to the 7500-runs-mean. The resulting relative error curves are shown in Figure 6.2 (b). As this figure shows, the relative errors are smaller than approx. 0.01 for the whole duration of simulations in each case. Based on this result, and the qualitative comparison of MSD curve distributions in Figure 6.2 (a), we are confident that a set of 2500 runs is enough to capture the behaviour of each of the three described models when simulating the 40 nuclei chosen from the experiment.

In addition to testing the robustness of the simulation outcomes, we also need to ensure that we choose the time steps for our simulations small enough. Therefore, using the model with c-dependent Γ, we repeat a 2500-runs-set of simulations with two different time steps, $\Delta t = 0.2$ min and $\Delta t = 0.02$ min. The results of these simulations are shown in Figure 6.3.

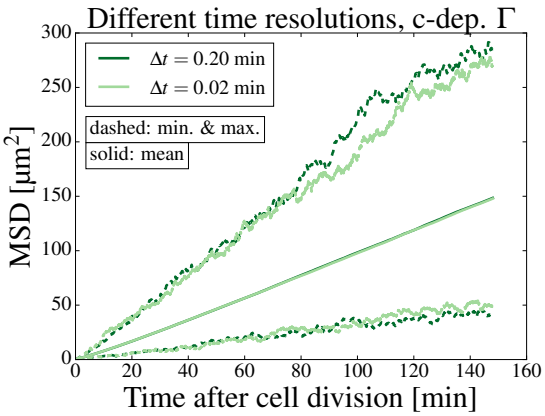

Figure 6.3 **Choice of time step for the simulations.** We verify our choice of time step Δt by repeating a 2500-runs-set of simulations using two different Δt values. As before, each of the two sets results in a distribution of MSD curves, with respective mean, maximum and minimum curves. The solid lines depict the means and the dashed lines the maxima and minima (as functions of time after cell division). Dark green represents simulations with $\Delta t = 0.20$ min, light green those with $\Delta t = 0.02$ min. Here, the model with c-dependent Γ is used. As the two plot shows, the choice of Δt does not change the MSD curve distribution.

Again we find a good qualitative agreement between the individual resulting distributions. As the simulation results using $\Delta t = 0.2$ min match up with those from simulations with a 10-times smaller time step, we continued to use $\Delta t = 0.2$ min for the rest of the simulations presented in the following for efficiency.

6.4.8 Only one model is compatible with the experiments

After testing our simulation results for robustness and validating the choice of Δt, we now compare the results obtained from different models with each other. Figure 6.4 (a) shows one 2500-runs distribution for each of the three models described by Equations 6.14, 6.15 and 6.16. We observe that the mean curve obtained using the c-dependent Γ model has a much larger slope than the other two mean curves and that the MSD curves from this model cover a different range of values than the MSD curves of the other two models. Furthermore, the distribution of the c-dependent F_{external} model is nearly identical to the one of the low density model. This indicates that the two possible high-concentration extensions to the low density model introduced in Section 6.3 have different effects. While the introduction of a concentration-dependance in Γ changes the dynamics of the simulated nuclei considerably in comparison to the low-c model, the introduction of an external force F_{external} based on the chemical potential of the nuclei appears to barely change the nuclear dynamics at all.

This justifies why we omit simulations that combine the effects of both a c-dependent Γ and F_{external}. As the effect of introducing F_{external} appears to be small in comparison to the effect of introducing a c-dependance in Γ, we do not expect to observe a difference between the results of including the c-dependance in Γ only and the combination model.

Adding the experimental MSD curve to simulation results, as shown in Figure 6.4 (b), reveals which of the models best reproduces the experiments. As Figure 6.4 (b) shows, the experimental MSD curve falls within the MSD curve distribution obtained from the model with c-dependent Γ, but neither agrees with the low-c model, nor the model that assumes the additional external force.

To confirm that the missing match between the experimental curve and the model with c-dependent external force did not simply result from the chosen values for the temperature T (also influencing the viscosity η) and the surface tension σ, we also repeat the simulations of this model with different parameter values. However, Figure 6.5 shows that changing T and σ does not change the distibution of simulated MSD curves. Thus, the mismatch between the experimental MSD curve and this particular model remains.

The results presented here provide justification and add weight to the nonlinear model described in Chapter 5 because they show that it is indeed possible to reproduce an important feature of individual nuclear movements, the MSD curve, under the assumption of interacting nuclei. This emphasises that IKNM can most likely not be understood as a single-cell phenomenon, even though we did not find any correlations between the trajectories of adjacent nuclei. Furthermore, the result shown in Figure 6.4 (b) actually enables us to distinguish between the possible different ways in which high nuclear density might influence the movements of individual nuclei suggested in Section 6.3. As only the range of MSD curves produced by the c-dependent Γ model matches the experimental MSD curve, this model occurs to be the one most likely to describe the actual nuclear dynamics in IKNM.

6.4.9 Comparison between numerical routines

To verify the above results that only the model with c-dependent Γ is consistent with the experimental MSD curve, we analyse simuation results using the alternative c-calculation in MATLAB as introduced in Subsection 6.4.3. Due to the repeated re-calculation of the nuclear concentration profile, this type of simulation is more time-consuming than the one used so far. Therefore, we only perfom one 2500-runs-set using the model with c-dependent

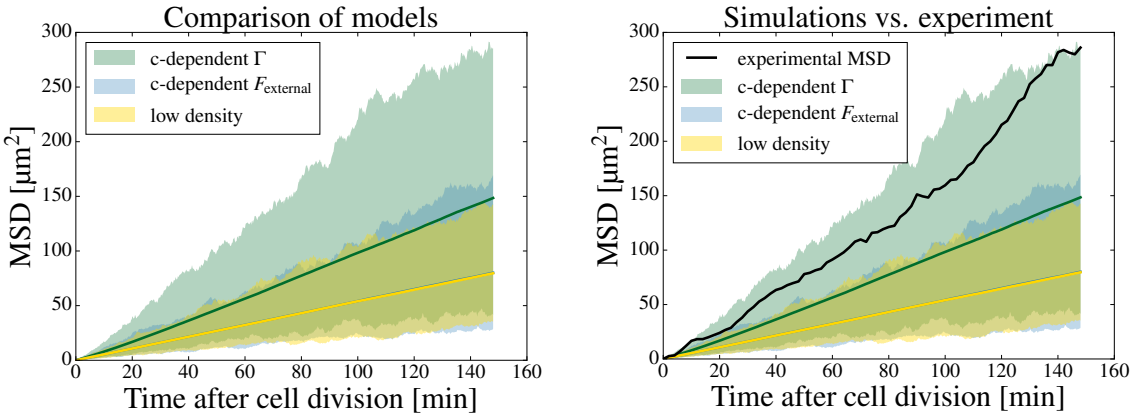

(a) (b)

Figure 6.4 **Comparison of simulation results and experiment.** (a) This figure shows the distribution of MSD curves of one 2500-runs-set for each of the three studied Langevin models. The solid lines depict the mean curves (as a function of time after cell division) and the shaded areas the range of values covered by the MSD curves of each model. Green colour represents the model with c-dependent Γ, blue colour the model with c-dependent F_{external} and yellow colour the low density model for comparison. This plot shows that the results obtained using the model with c-dependent F_{external} are nearly identical to the low density model. In contrast, the model with c-dependent Γ clearly produces a different distribution of MSD curves with a much larger mean slope. (b) The same plot as in (a) but with the experimental MSD curve added (black solid line). This plot shows that only the model with c-dependent Γ is compatible with the experimental results, as the experimental MSD curve lies within an area of the plot that is only covered by the distribution of MSD curves obtained using this c-dependent Γ model.

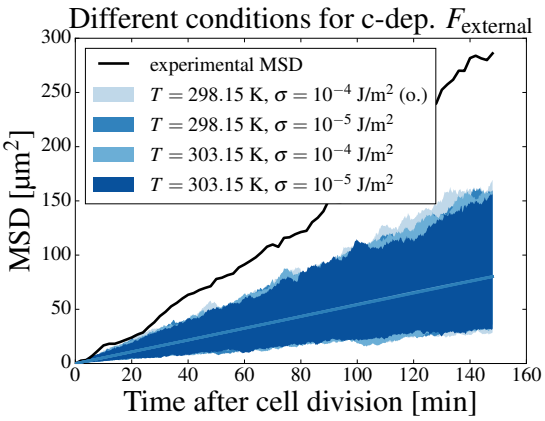

Figure 6.5 **Effect of different parameter values on the c-dependent F_{external} model.** This plot shows the distribution of MSD curves of one 2500-runs-set each for four different combinations of parameter values for T (and thus η) and σ in the model with c-dependent F_{external}. The blue solid lines depict the mean curves (as a function of time after cell division) and the shaded areas the range of values covered by the MSD curves in each case. The different shades of blue represent the different parameter sets as specified in the legend. The set of parameters labelled with (o.) is the one also used for Figure 6.4. For comparison, the experimental MSD curve is shown (black solid line). As this plot shows, the changes in parameter values do not change the distribution of MSD curves obtained using this model. Hence the model with c-dependent F_{external} is not consistent with the experimental results.

Γ. Figure 6.6 compares the resulting MSD curve distribution of this set with the one obtained from the previous simulations using the same Langevin model but the simulation routine in Python. The figure shows that there is a good agreement between the maximum curves obtained with the two different simulation methods but the minimum curves differ from each other, resulting also in different mean curves.

This finding raises the question whether the simulation results of all three Langevin model using the MATLAB routine would differ between each other in the same way as the simulation results using the Python routine do (compare Figure 6.4 (a)). More importantly, would one obtain the same outcome when comparing the simulation results to the experimental MSD curve?

For time constraint reasons, we are not able to perform 2500 runs for each of the three Langevin models using the MATLAB routine. However, based on the data obtained for the c-dependent Γ model we evaluate how many or few runs we need for each model to still obtain a meaningful result. Figure 6.7 (a) provides a comparison of mean curves and distributions of subsets of 250 MSD curves each of the total 2500 MSD curves of this model. In Figure 6.7 (b) the errors of these subset curves relative to the mean curve of the whole 2500-runs-set are shown. These plots indicate that even the small subsets still provide a robust outcome of simulation results, although the relative errors calculated here are slightly larger than those of previous simulations (here: relative errors smaller than approx. 0.05, previously: smaller than approx. 0.01).

Therefore, using the MATLAB routine, we perform 250-run-sets of the other two Langevin models and compare the outcomes of all those simulations with the experimental data. As is evident from the plot in Figure 6.8, although the results using the MATLAB routine differ from the results using the Python routine, the dissimilarity between the three Langevin models remains. Again, only the distribution of MSD curves obtained using the c-dependent Γ model is consistent with the experimental MSD curve. Therefore, we are confident that this model is indeed the one most likely to describe the dynamics of nuclear movements in IKNM.

6.4.10 A note on the other data sets

We perform a similar analysis as presented in Subsection 6.4.8 based on the data from the second normal condition experiment (see Chapter 4). That means we select those nuclei from the experimental data that were born early enough and had tracking data available long

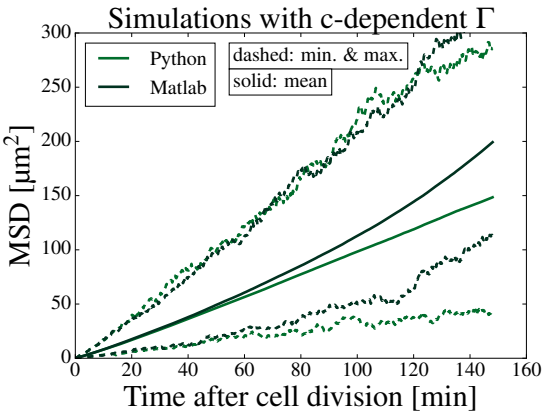

Figure 6.6 **Comparison between simulation results using the two different routines.** We test the simulation results by repeating a 2500-runs-set of the c-dependent Γ model simulation using the alternative numerical routine coded in MATLAB (compare Subsection 6.4.3). Here, the mean curves (solid lines) and maximum and minimum curves (dashed lines) of the distributions obtained using the MATLAB and Python routines are shown. Dark green colour represents the results obtained using the Matlap routine and medium green colour the results obtained using the Python routine (same results as shown in Subsection 6.4.8). There is a good agreement between the two maximum curves, but the minimum curves differ from each other, resulting in different mean curves as well.

enough to be of interest for simulations, as specified in Subsection 6.4.4. In the case of the second normal condition data set - which is much smaller than the first - this amounts to 16 (instead of 40) nuclei. We simulate those exact 16 nuclei under the assumption of the three possible models specified by Equations 6.14, 6.15 and 6.16. For these simulations, we use the nuclear concentration profile $c(r,t)$, its gradient $\partial c(r,t)/\partial r$ and the values for D^*_{nonlin} and c^*_{max} that we obtained for this exact data set in Chapter 5. As the number of nuclei is lower in these simulations, we perform more runs of each simulation to ensure sufficient statistics. In the case of our main data set we repeated each simulation 2500 times, resulting in a total of 100000 simulated nuclei. Here, as we only simulate 16 nuclei per run, we increase the number of runs to 6250 to obtain the same total number of nuclei simulations.

In principle, the simulation results between the two data sets might not be completely equivalent. This becomes apparent, for example, when considering the effect of nuclear trajectories that deviate extremely from the mean over all trajectories. While there is no reason that such trajectories should be expected in simulations based on one sample more often than in simulations based on the other sample, we should expect them to make a difference in the type of plots shown in Figure 6.1. If, for example, one such trajectory can be expected on average for every i-th simulated nucleus and we cluster approx. i trajectories

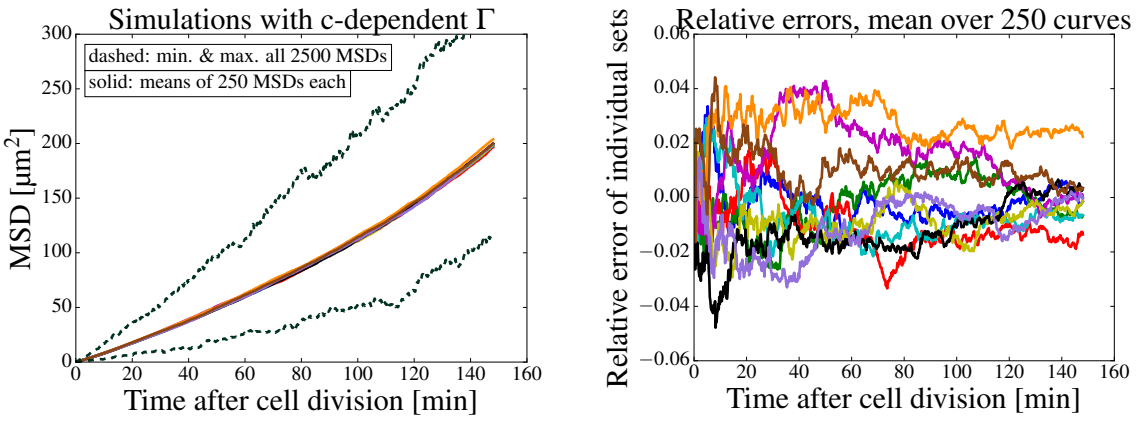

(a) (b)

Figure 6.7 **The robustness of simulation results using the MATLAB routine.** We assess whether sets with a small number of runs of the MATLAB routine still provide robust outcomes. To this end, we subdivide the 2500-runs-set presented in Figure 6.6 into subsets of 250 runs each. Plot (a) shows the mean curves of these subsets (solid lines) and the maximum and minimum curves of the full 2500-runs-set for comparison (dashed lines). In (b) the errors of the 250-runs means in (a) relative to the mean of the full 2500-runs-set are plotted. That is, $\mathrm{RE} = (\mathrm{mean}(250\mathrm{runs}) - \mathrm{mean}(2500\mathrm{runs}))/\mathrm{mean}(2500\mathrm{runs})$. The colours represent the individual subsets of 250 runs. Although the differences between individual subsets are larger here than previously, with relative errors up to approx. 0.05 instead of 0.01, the simulation outcome is still robust when using 250-runs-subsets.

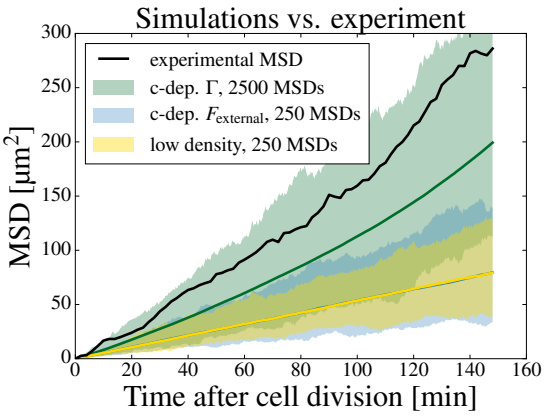

Figure 6.8 **Comparison between MATLAB simulation results and experiment.** This figure shows the distribution of MSD curves obtained using the routine coded in MATLAB (compare Subsection 6.4.3) for each of the three studied Langevin models in comparison to the experimental MSD curve. The distribution for the model with c-dependent Γ (in green) is the same as shown in Figure 6.6 and contains 2500 simulated MSD curves. The distributions for the model with with c-dependent F_{external} (in blue) and the distribution for the low density model (in yellow) contain 250 MSD curves each. Green, blue and yellow solid lines represent the mean curves of each distribution. The black solid line depicts the experimental MSD curve. Although the mean curves for the MATLAB simulation results quantitatively differ from the Python results (compare Figure 6.6), the main result in relation to the experiments still holds: the experimental MSD curve lies within an area of the plot that is only covered by the distribution of MSD curves obtained using the c-dependent Γ model. Thus, this model is the only one compatible with the experiment.

when calculating a MSD curve, the other trajectories will counterbalance the extreme one. However, if we cluster only a number of trajectories $\ll i$ into each MSD curve, the effect of the extreme trajectory will be very strong in one MSD curve and non-existent in some of the others. Therefore, we expect that the distribution of the MSD curves becomes wider if we cluster fewer trajectories into each one of them.

But given the very different sizes of the experimental data sets, the approach of simulating 40 nuclei per run for the first data set and 16 nuclei for the second data set seems sensible. Else, if we were to make the simulations entirely comparable between the two, we would have to considerably cut down on the size and probably on the informative value of the main data set. Only comparing the MSD curve from each experiment with simulations based on that exact experiment should at least mitigate inter-data-set differences at best possible.

For the second normal data set, repeating each 6250-runs-set of simulations three times and plotting the relative errors as described in Subsection 6.4.7, we again verify that those relative errors are smaller than approx. 0.01. We then compare the experimental MSD from this second data set with the three model results. Unfortunately, in this case no clear distinction between the three models emerges, as the experimental MSD curve falls within an area of the plot that is covered by the distributions of MSD curves from all three models.

However, this result does not contradict the statements made in Subsections 6.4.8 and 6.4.9 based on the results of the main data set, as the experimental MSD curve from the second data set can similarly be explained by the model assuming a c-dependent Γ. The second data set simply provides a weaker statement than the first data set because it does not rule out any of the three models.

Possibly the reason for the difference in informative value between the simulations based on the first and second normal data sets is to be found in the effect described above, namely the different numbers of nuclei available for simulation.

We forewent performing simulations based on the high-T and low-T data sets because it appears questionable whether we would be able to select a large enough number of nuclei from the experiment to draw conclusions when evaluating the simulation results. In the case of the high-T data set, although the cell cycle time is shorter and thus cell divisions occur at a higher rate, the experiment starts out tracking even fewer nuclei than for the second normal condition data set. In the case of the low-T data set, although the experimental data starts out

with more nuclei being tracked, only very few cell division were observed at all due to the prolonged cell cycle time. Therefore, in both cases we do not expect to be able to simulate a sufficient number of nuclei and thus do not present any such simulations here.

6.4.11 On the time evolution of mean-squared-displacement curves

Lastly, we employ the simulations of individual nuclear trajectories to provide evidence that nuclei indeed exhibit different dynamics depending on their packing density. In order to do so, we split the set of nuclei we have been simulating so far into subsets. In one case, we produce subsets of 5 nuclei each without taking their birth times into account. In the other case, we cluster nuclei by birth times (separating sets of 4 min each), resulting in subsets of varying sizes. For each subset, we adapt the number of runs of the simulations such that we obtain a total of 100000 simulated nuclei (compare Subsection 6.4.10).

As these subsets are very small, we do not expect to be able to draw meaningful conclusions when comparing with the experiments, as discussed in Subsection 6.4.10. Nevertheless, we can compare the results obtained for the different subsets with each other and with the simulation results for the full set of nuclei.

Figure 6.9 shows mean curves of MSDs from either the simulations of the total 40 nuclei or the different subsets. The mean curves of the subsets vary much more between each other than the mean curves of the three 2500-runs-sets of the total 40 nuclei simulations. Furthermore, later nuclear birth time tends to increase the MSD for any give time point. This hold true early in the simulation, when nuclei are in areas of the tissue with high nuclear packing, but is even visible later in the simulation, when nuclei have (on average) moved to areas of lower nuclear concentration. This result underlines our earlier discussion in Subsection 6.4.5 that nuclear dynamics might be concentration- and thus time-dependent and therefore clustering nuclear trajectories obtained at different times of the experiment should be performed cautiously.

6.5 Discussion

In this Chapter, we have extended the study of IKNM to the level of single cells. Based on the results in Chapter 5, we first sought to obtain a microscopic interpretation of the previously

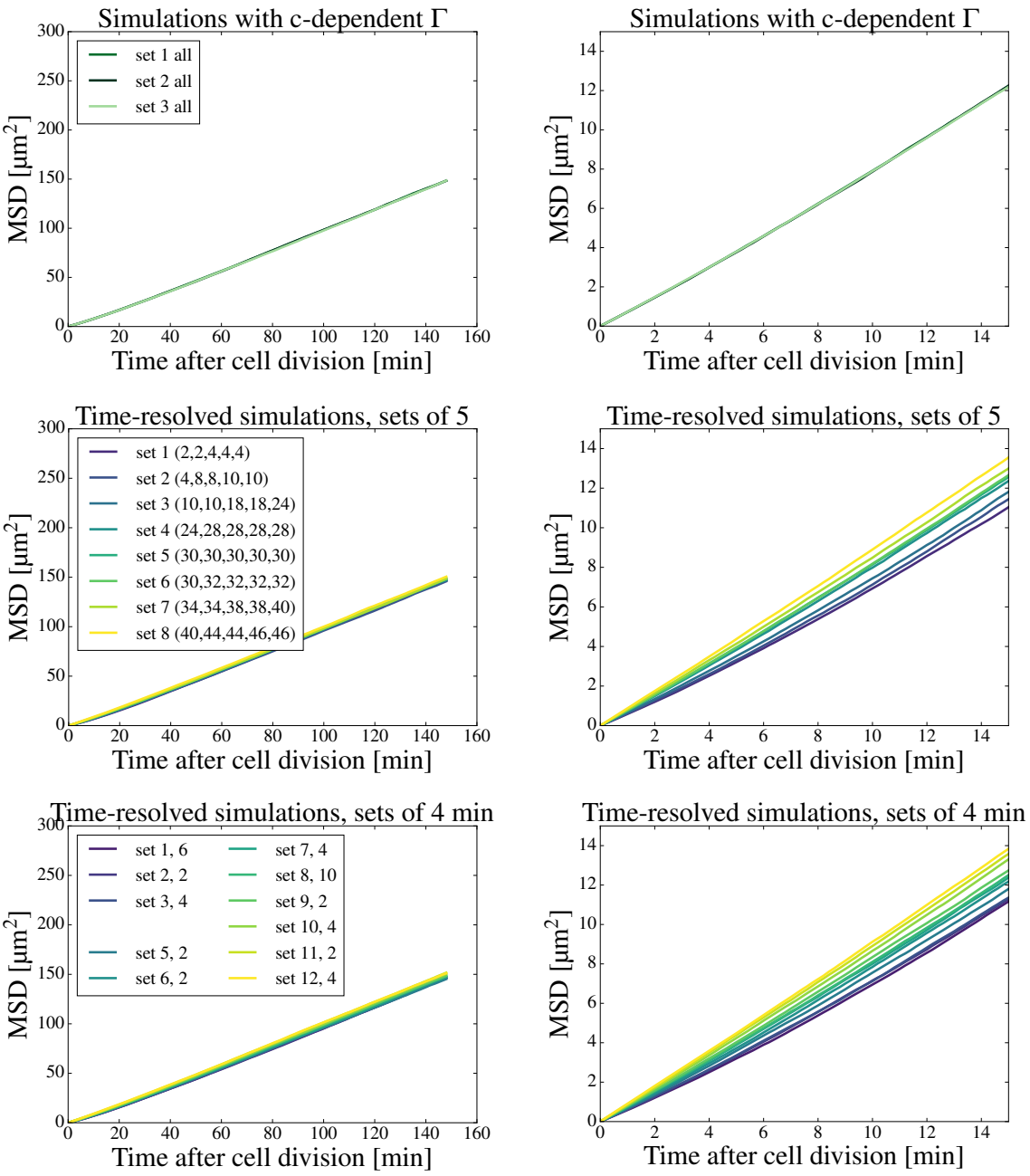

Figure 6.9 **Changing dynamics of nuclei based on birth time.** This figure shows mean curves of MSDs (main data set, Python routine). In the top row, three 2500-runs-sets of 40 nuclei are shown (same as in Figure 6.2). For the second row, these 40 nuclei are clustered into subsets of 5 nuclei each, with birth times given in the legend in min. For the third row, these 40 nuclei (and the 2 next-born ones) are clustered by birth time (subsets of 4 min each), with the number of nuclei per subset given in the legend. The first column of plots depicts the whole MSD curves, the second column enlarges the first 15 min after cell division and the third column (second part of this figure) enlarges the last simulated 15 min. For the subsets, the number of runs is adapted, so each MSD curve includes a total of 100000 simulated nuclei. This figure indicates that nuclei with different birth times exhibit different dynamics.

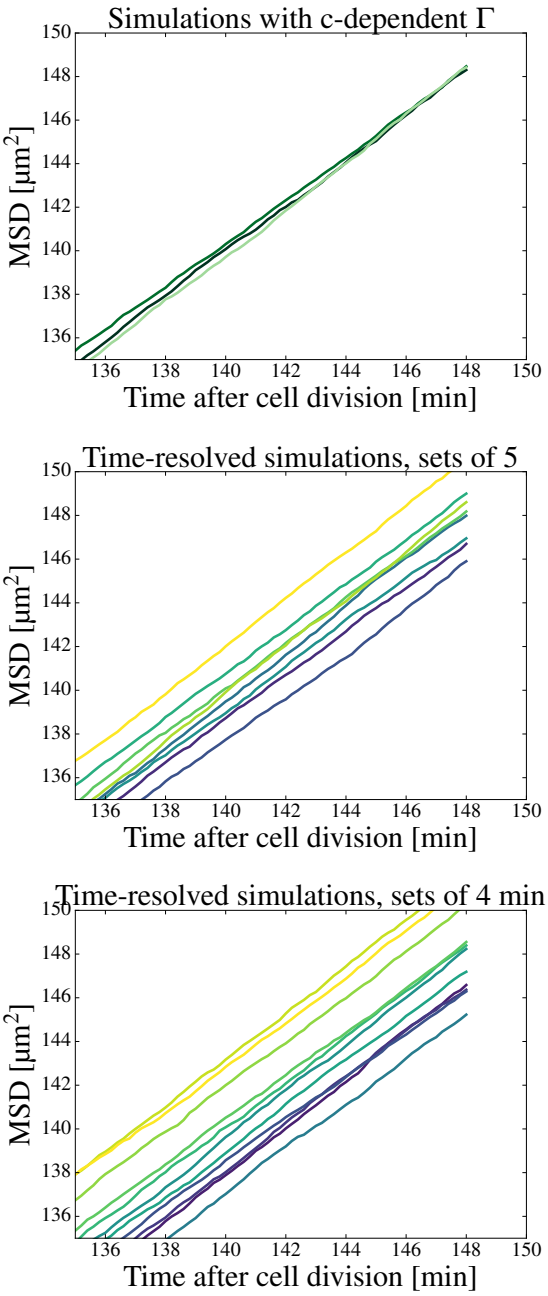

Figure 6.9 **Changing dynamics of nuclei based on birth time** (continued).

established value for D^*_{nonlin}. To this end, we made use of the fact that the nonlinear model for IKNM on the tissue level converges to the linear one as $c \to 0$. We were thus able to employ the well-known properties of thermal diffusion to evaluate D^*_{nonlin} at small c. We found that the value of D^*_{nonlin} can neither be understood by assuming free thermal diffusion of the nuclei nor by simply including effects of membrane-hindered diffusion. Instead, our calculations suggest that both hindering and driving forces have to be included, with nuclear mobility slowed-down due to the presence of the membrane and cytosolic composition and speeded-up due to active transport. Assuming membrane effects and active transport in a Langevin model for nuclear dynamics at low densities provided an estimate for the strength of the required transport forces, which is consistent with the existence of cytoskeletal transport throughout the whole cell cycle.

Next, we extended the Langevin formalism for individual nuclear dynamics to include the effects of high nuclear packing densities. Here, we mainly considered two possible models. The first one, a direct application of the correspondence between linear and nonlinear diffusion model for tissue level IKNM, included concentration-dependent effects via a c-dependent stochastic force, i.e. a c-dependent value of Γ. In contrast, the second model included concentration-dependent effects as an additional, conservative force derived from the chemical potential of the nuclear concentration field. As it emerged later, studying a combination of the two models would not be fruitful. The resulting models provided a possibility to explore the properties of individual nuclear trajectories under conditions similar to those found in the experiments. Simulations of nuclear trajectories using both models and the low concentration model for comparison as well as two different numerical routines revealed that the models can be distinguished based on resulting mean-squared-displacement curves. While the model with c-dependent F_{external} produces MSD curves similar to those obtained in the low-c case, the MSD curves produced by the model with c-dependent Γ are on average much steeper than those of the other two models.

Furthermore, this last result also enabled us to identify the model the most likely to describe the nuclear dynamics in the real retinal tissue. When comparing the distributions of MSD curves obtained from the simulations to the experimental MSD curve, we found that only the MSD curves of the c-dependent Γ model matched the experimental one. This finding could be reproduced using both numerical routines, although the exact distribution of MSD curves varied between the two. While we were not able to recreate the same result when simulating nuclei of other data sets, this is presumably due to their small size. Therefore, we conclude that the effects of dense nuclear packing influence the nuclear mobility by locally

increasing the strength of the stochastic force.

When estimating the movement-inhibiting effect of the tight cellular wrapping aroung the nucleus, we here only took the presence of the plasma membrane into account. However, in cells, an actin network lies immediately underneath this membrane. This network, called the cell cortex, plays a crucial role in determining the mechanical properties of cells including cell surface tension and cell shape [153] [154]. Therefore, the movement-inhibiting effects of the cellular geometry are probably not only due to the plasma mebrane, but rather result from an interplay between membrane and cortex. However, the exact properties of the cortical actin network seem to vary greatly between cell types, with reported cortex tension values differing by at least two order of magnitude [153]. In addition, the coupling of membrane and cortex might further tune the overall cell contractility in a non-trivial way [154]. Therefore, it might be difficult to determine the exact resulting cell surface tension acting on the nucleus within. Nevertheless, given that the cortex is usually contractile [153] [154], we can deduce that the presence of the cortex might increase the overall cell surface tension as compared to the membrane tension alone. As such, the tension values assumed here might represent a lower bound to the true surface tension in RPCs. Thus, as an increase in σ results in an increase of the friction coefficient γ_{tube} and a further decrease of the diffusion constant D_{tube}, including the presence of the cortex would likely reinforce our conclusions. This is, an even smaller value of D_{tube} only the more suggests that nuclei might be actively driven throughout the entire cell cycle. Furthermore, while the value of Γ itself is tension-dependent, the stochastic terms in the different Langevin models are actually not, because they are proportional to $\sqrt{\Gamma}/\gamma_{\text{tube}}$ as shown in the equations for the Euler-Maruyama method. Hence, an increase in σ should lead to an even larger difference between the distributions of mean-squared-displacement curves resulting from the two high-c models because the only tension-dependent term in these models, $F_{\text{external}}/\gamma_{\text{tube}}$, decreases with increasing σ. The only point that remains to be determined based on a potentially revised value of the overall surface tension is whether the resulting stochastic force is still compatible with cytoskeletal transport as inferred above.

Regarding the connection between the models presented here and in Chapter 5 it is clear that the results of the Langevin models depend on the correctness of the previously obtained nuclear concentration profile. To disentangle this interdependence, in principle one could imagine a numerical approach where one simulates many nuclei simultaneously and after each time step evaluates the current distribution of the nuclei to obtain their concentration profile at this time step. This concentration profile could then be used as an input for the next step of the simulation. In this way, the simulations of nuclear trajectories in this Chapter

could be made independent of the previous concentration profile. If one were to run a large number of simulations of this type it might even be possible to obtain a rough estimate for the value of D independently of the results in Chapter 5. However, there are several major reasons why we have chosen not to utilise this independent numerical approach here. Firstly, compared to the approach presented in this Chapter, the independent approach would require simulations on a much larger scale. For example, most of the shown mean-squared-displacement curve distributions contained 2500 individual MSD curves, each of which was calculated from 40 individual nuclear trajectories, resulting in 100000 simulated nuclei per MSD curve distribution. If such distributions were to be extracted for a number of different values of D, many millions of nuclear trajectories would need to be computed. In addition, the repeated new calculation of the concentration profile after each time step would lead to a considerably slower numerical routine compared to the one mainly employed here. Together, these factors might make high-performance computing methods inevitable. Whether these increased numerical efforts would be fruitful in extracting the value of D independently, however, is not clear. For example, in Chapter 5 the analysis of data from zebrafish grown at different temperatures indicated that T has statistically significant effects on D, but the extracted D-values differed only by about a factor of 2 even between the high and low temperature experiments. Given the relatively broad distributions of MSD curves shown here, it is not *a priori* clear whether the independent numerical approach would be able to distinguish between different D-values at this level of resolution, as MSD curve distributions for various D-values might match the experimental curve. Unfortunately, given the size of the experimental data sets, it is not possible to simulate more nuclei per MSD curve to narrow the resulting MSD curve distributions. Therefore, the potential outcome of an independent numerical approach might not justify the elevated numerical costs. Secondly, varying the diffusion constant in such an independent approach might actually remove the possibility of distinguishing between the different high-c Langevin models, because large enough variations in D might lead to any model being compatible with the experimental mean-squared-displacement curve. Finally, and most importantly, there is an underlying consideration regarding the concentration profile itself that needs to be recognised when wishing to simulate nuclear trajectories independently of the results in Chapter 5. This is the fact that the nuclei simulated here only represent a subset of the total number of nuclei in the retinal tissue. This subset was chosen based on various practical aspects, like sufficient length of the experimental track, as outlined throughout this Chapter. If one were to calculate the nuclear concentration profile directly from the simulated nuclear trajectories, a way would have to be devised in which the other nuclei can be taken into account as well. Simply simulation all nuclei in the tissue from their birth until their eventual division does not appear to be possible

because even at the start of the experiment the tissue already contains a large number of cells in various stages of the cell cycle. On the other hand, extrapolating the nuclear concentration profile directly from the experimental data is probably equivalent to the approach we have taken here, as any extrapolation also assumes an underlying functional relationship. Here, we merely chose the relationship given by our previously devised diffusion model.

Although we based a considerable amount our analysis in this Chapter on the calculation of mean-squared-displacement curves, we also indicated that these curves should be used cautiously. As aforementioned, the supposed concentration dependence of IKNM results in early born nuclei displaying different dynamics than nuclei born later in development, when the nuclear density is high. Therefore, the trajectories of nuclei occuring at different experimental times should not be clustered. However, this was unknown in previous studies [92] [96] [87] [98]. If the concentration dependence of IKNM proves to be genuine, the data obtained in these previous studies might need to be re-evaluated.

Here, for statistical reasons, we clustered the trajectories of nuclei with varying birth times nevertheless. However, we alleviated the difficulty arising from this clustering by ensuring that all performed numerics simulated nuclei with the exact same birth time distribution as found experimentally.

A second problem to be carefully considered arises with the interpretation of nuclear mean-squared displacement curves. In the biological literature, the practice of determining the mode of nuclear mobility (i.e. random motion versus ballistic motion) solely based on the mean-squared-displacement curve can be found. However, the notion that $\langle x^2 \rangle \propto t$ for diffusive movement (as opposed to $\langle x^2 \rangle \propto t^2$ for ballistic movement) is specific to thermal diffusion (i.e. Brownian motion). More general classes of random walk processes can have a different mean-squared-displacement relationship, e.g. $\langle x^2 \rangle \propto t^\alpha$ with $\alpha > 1$ for superdiffusive processes like Lévy walks [15]. On the other hand, experiments have uncovered the existence of systems with the same mean-squared-displacement relationship as Brownian motion but a non-Gaussian underlying probability distribution [155] [156]. As it is not *a priori* clear that IKNM can be described using the model of Brownian motion - and our results presented in this Chapter and Chapter 5 suggest that this is not the case - interpreting MSD curves based on the properties of this particular random walk process should be performed cautiously.

In fact, we have also made use of the properties of Brownian motion to make progress in this Chapter, most notably in Section 6.2 where we explored the possible interpretation of the exact value of D^*_{nonlin} and estimated the strength of the stochastic force. We specifically noted that the derivations in that Section are only valid in the case of low nuclear concentration $c \to 0$, when nuclei are expected not to interact and Equation 6.2 converges into Equation 6.1 describing Brownian motion. However, we can not guarantee that Equation 6.2 is the correct equation to describe IKNM to begin with. We exclusively base our work on the fact that the model based on Equation 6.2 resulted in a very good fit of the experimental data in Chapter 5. Nonetheless, since the model based on Equation 6.2 is the best available model to describe IKNM at this point, we continued to use its properties (and the properties of Brownian motion) to decipher the physical mechanisms underlying IKNM.

The results of our microscopic interpretation of D^*_{nonlin} and of the simulations of individual nuclear trajectories based on Langevin equations so far strongly suggest that nuclei are moved by means of cytoskeletal transport throughout the entirety of the cell cycle. This transport appears not to be unidirectional but highly stochastic during IKNM. Possibly, a tug-of-war mechanism with various components attempting to move the nucleus in different directions simultaneously might be at play. However, in order to document the underlying molecules responsible for this mechanism in detail, an experimental approach - maybe similar to the one used to study the apicalward movement of nuclei in G2 recently employed by Yanakieva et al. [109] - appears inevitable.

Such an experimental approach would also be beneficial when aiming to confirm the mode of c-dependence of the nuclear dynamics suggested by the comparison between simulated and experimental MSD curves. This comparison indicated that the stochastic forcing itself might dependent on the surrounding nuclear concentration. Given the probable involvement of cytoskeletal components in IKNM throughout the cell cycle, the c-dependence of Γ can be understood under the assumption that cells can sense the nuclear packing density. If the cells then recruited more molecular motors to areas where nuclei are particularly densely packed, the strength of the stochastic transport forces would be dependent on c. Nuclei would thus be transported away from areas of high nuclear packing faster.

Finally, the calculations to interpret D^*_{nonlin} implied a strong involvement of the cell membrane in determining the nuclear mobility during IKNM. This involvement is based on the understanding that PSE cells tightly enclose their nuclei and that their cell membranes have to be deformed for the nuclei to move. Although we have referred to a previous study

deriving a mathematical formalism for such conditions, we have not examined the cellular geometry in the zebrafish retina in detail so far. Therefore, in the following Chapter, we will divert our attention towards the shape of RPCs.

a	index denoting apical
b	index denoting basal
c_0, c_1, c_2	intrinsic and principal curvatures of cell membrane
E	shape energy of the lipid membrane
g^{ij}	metric tensor
H	mean curvature
H_{circle}	mean curvature of a circle
K	Gaussian curvature
k_{B}	Boltzmann constant, 1.38×10^{-23} m^{2}kg/s^{2}K
L	tissue thickness
p	pressure
R	(average) nuclear radius
$\vec{R}$	positional vector
R_m	radius of the membrane tube around the nucleus
R_0, r_0	fixed values of r at the centre of nucleus and tissue surface
r	radius of the cell
r_{contact}	membrane radius where membrane becomes arc around nucleus
r_{tube}	equilibrium radius of a membrane tube
S_a, S_b	apical and basal tissue surface area
$\mathscr{S}_a$, $\mathscr{S}_b$	apical and basal cell surface area
T	temperature
x, y, z	spatial coordinates, where z is the axis along the cell
z_{contact}	z-coordinate where membrane becomes arc around nucleus
Δ	Laplace-Beltrami operator
δ_a, δ_b	apical and basal cell radii
δ_m	average cell radius
θ	opening angle of membrane tube
κ	bending rigidity of the cell membrane
ρ_a, ρ_b	radial coordinates of apical and basal tissue surface
σ	surface tension of the cell membrane
ϕ	angle of rotation around z-axis

Chapter 7

Wrapping it up - cell membrane geometry in pseudostratified epithelia

William A. Harris (Department of Physiology, Development and Neuroscience, University of Cambridge) provided a video by Tilak Das (a graduate student in his group at the time of data acquisition) showing the shape and cell division of individual retinal progenitor cells. A cropped frame of this video is shown in Figure 7.7 (b). Except for collaborations with my Supervisor Raymond E. Goldstein, who suggested to study the geometry of RPCs, employ the Helfrich elastic model for lipid bilayers and consider the thermal fluctuations of the membrane around the nucleus, the remainder of the work presented in this Chapter is my own.

7.1 Introduction

After having assessed the details of nuclear movements during IKNM on both the tissue and single cell level, we now examine the geometry of the individual cells in the retinal pseudostratified epithelium. This cell geometry might be a crucial factor in development. Most importantly in the light of the hitherto presented results, the slender shape of RPCs implies a role of the cell membrane in determining the mobility of individual nuclei in IKNM (compare Chapter 6). In addition, studying the specific shape of RPCs might lead to valuable conclusions in their own right. For example, the results presented in this Chapter might also be relevant for understanding the shapes of a broader class of cells, such as neurons.

In Section 7.2, we first use our own experimental data and information available in the literature to retrieve geometric parameters of zebrafish retinal progenitor cells. Using these rough estimates we proceed to study the cell membrane as a proxy for RPC shape in closer

detail. To this end, we employ the Helfrich elastic model for lipid bilayers, introduced in Chapter 3. We adapt this model to the specific case of PSE cells in Section 7.3 and present numerical solutions thereof in Section 7.4. These numerical solutions are capable of producing shapes not unlike those of real RPCs for a range of physiologically relevant parameters. Furthermore, we find a possible link between the geometry of RPCs and the previously investigated geometry of membrane tethers. Finally, we demonstrate *a posteriori* that the RPCs fulfil the assumptions underlying the calculations by Daniels [147], which we have previously used to obtain the membrane's influence on the diffusion constant.

7.2 The cellular geometry of RPCs

In this Section we aim to obtain a rough understanding of the shape of PSE cells based on our experimental data (although we did not image cell membranes directly) and the available literature. First, in Subsection 7.2.1, we calculate the radii of RPCs at various points along the apicobasal axis. Then, in Subsection 7.2.2 we estimate the size of the gap between the nucleus and the cell membrane enveloping it. These measures inform the more detailed investigation throughout the remainder of this Chapter.

7.2.1 The apical and basal cell radii

It is well-known from the biological literature that RPCs are very slender and bulge around the nuclei (compare e.g. [84]). Additionally, each cell stretches the entire radial dimension of the retina, and thus has length L in the apicobasal dimension. Here, we use $L = 55$ µm, as given from our main data set.

As the retina is a curved tissue, its apical surface has a much larger surface area than its basal surface. Therefore, we expect the retinal progenitor cells to have a larger radius apically than basally (compare Figure 7.1 (a)). For now, we can further neglect any lateral membrane deformations - which we will study in detail in the following Sections - and assume that the cells are approximately shaped like right circular conical frusta, similar to Figure 7.1 (b). Then the apical and basal cell radii, δ_a and δ_b, can be approximated from data available in the literature.

Matejčić, Salbreux and Norden [136] provided data for the aspect ratio of zebrafish retina tissue and progenitor cells as a function of developmental stage. In this study, the tissue aspect ratio was calculated as tissue aspect ratio = tissue thickness/$\sqrt{\text{tissue area}}$, where the value used for the tissue area was the average of the apical and basal tissue areas. The cell aspect ratio was similarly calculated as cell aspect ratio = tissue thickness/$\sqrt{\text{cell area}}$, where the cell area was taken to be the average tissue area (as before) divided by the number of RPCs within the tissue. Reversing the calculation by Matejčić, Salbreux and Norden [136] based on the aspect ratio provided for the developmental stage we examined in our project and using the tissue thickness from our main experiment ($L = 55$ µm) we obtain an estimate for δ_a and δ_b under the assumption that RPCs are right circular conical frusta. We use

$$\text{cell area} = \left(\frac{\text{tissue thickness}}{\text{aspect ratio}}\right)^2 = \left(\frac{L}{\text{aspect ratio}}\right)^2 \tag{7.1}$$

$$S_a = 4\pi\rho_a^2 \qquad \text{and} \qquad S_b = 4\pi\rho_b^2 \tag{7.2}$$

$$\Rightarrow \frac{S_a}{S_b} = \frac{\rho_a^2}{\rho_b^2} = \frac{\mathscr{S}_a}{\mathscr{S}_b} \tag{7.3}$$

$$\text{cell area} = \frac{1}{2}(\mathscr{S}_a + \mathscr{S}_b) = \frac{1}{2}\left(\frac{\rho_a^2}{\rho_b^2}\mathscr{S}_b + \mathscr{S}_b\right) \tag{7.4}$$

$$\Rightarrow \mathscr{S}_b = \frac{\text{cell area}}{\frac{\rho_a^2}{\rho_b^2} + 1}. \tag{7.5}$$

Here, S_a and S_b are the the apical and basal tissue surface areas and ρ_a and ρ_b the apical and basal tissue radii (i.e. the distances of these surfaces from the centre of the lens). Further, $\mathscr{S}_a$ and $\mathscr{S}_b$ are the apical and basal cell surface areas. For the developmental stage we study (imaging for several hours beginning at approximately 30 hpf for our main sample, see Chapter 4), Matejčić, Salbreux and Norden [136] report a cell aspect ratio between 15 and 20. Thus, we obtain the values listed in Table 7.1 for the cell surface areas and cell surface radii δ_a and δ_b.

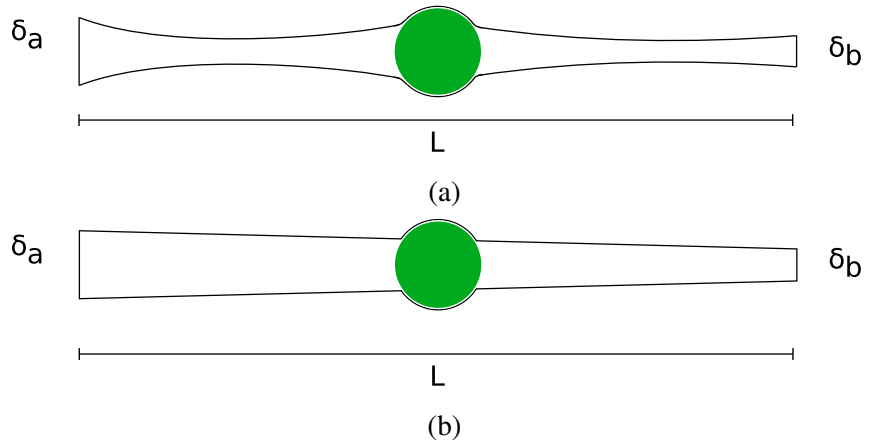

Figure 7.1 **Approximate cell geometry for parameter estimation.** This figure shows how the geometry of RPCs is approximated in order to calculate the parameters used in the following. While it is well-known that RPCs bulge around their nuclei (compare e.g. [84]), as shown schematically in (a), we here neglect lateral membrane deformations (which we study in detail later) and assume that the cells are right circular conical frusta, as shown in (b). As the zebrafish retina is a curved tissue, we expect the apical cell radius δ_a to be larger than the basal cell radius δ_b.

Table 7.1 **Cell geometry parameters.** The parameters listed here for the apical and basal cell surface areas, $\mathscr{S}_a$ and $\mathscr{S}_b$, as well as the apical and basal radii, δ_a and δ_b, are calculated based on the assumption that cells are shaped approximately like right circular conical frusta and using the cell aspect ratios given in Matejčić, Salbreux and Norden [136].

	aspect ratio = 15	aspect ratio = 20
$\mathscr{S}_a$	22.0043 μm^2	12.3774 μm^2
$\mathscr{S}_b$	4.8846 μm^2	2.7476 μm^2
δ_a	2.65 μm	1.98 μm
δ_b	1.25 μm	0.94 μm

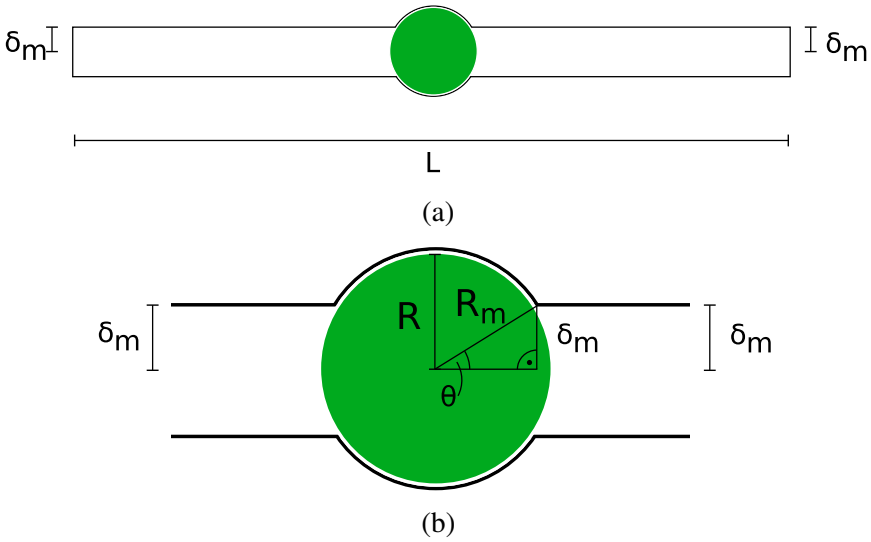

Figure 7.2 **Approximate cell geometry for calculating membrane deformation.** This figure shows how the geometry of RPCs is approximated in order to estimate the membrane deformation around the nucleus. While we have assumed a right circular conical frustum shape for RPCs in the previous Subsection 7.2.1, we here simplify the cell shape even more and assume it to be cylindrical with an average tube radius, δ_m, as depicted in (a). (b) Enlarged section of the picture in (a), focussing on the nucleus. R is the nuclear radius and R_m the radius of the membrane tube wrapping around it. The opening angle of the tube is called θ.

7.2.2 The gap size between nucleus and membrane

If the cell shape is approximately cylindrical locally, we recover the situation studied by Daniels [147], as shown in Figures 7.2 (a) and (b). In this case, we can calculate the radius R_m as a correction to the nuclear radius R using the formula derived by this author to be

$$R_m = R + \left(\frac{R\,(k_{\mathrm{B}}T)^2}{64\kappa\sigma} \right)^{1/3} . \tag{7.6}$$

We obtain $R_m \approx R + \left(4.8 \times 10^{-3}\right)$ to $R + \left(1.0 \times 10^{-2}\right)$ µm. Thus, R_m only constitutes a very small correction to the nuclear radius R.

7.3 Applying the Helfrich model to PSE cells

After having obtained estimates for the apical and basal cell radii δ_a and δ_b, as well as the deformed tube radius R_m in the previous Section, we now proceed to calculate more realistic

cell shapes, taking the membrane geometry along the whole apicobasal dimension of the RPCs into account. To this end, we employ the Helfrich elastic model for lipid bilayers, introduced in Chapter 3. In this Section, we adapt this model to the specific case of retinal progenitor cells. First, in Subsection 7.3.1, we specify a parameterisation adequate to the geometry of RPCs. Afterwards, in Subsection 7.3.2 we derive an ordinary differential equation for the membrane shape. We will solve this equation numerically in the following Section.

7.3.1 Specific parameterisation for RPCs

Using Equations 3.23 and 3.24, we are able to calculate all the terms in Equation 3.19 without knowing the principal curvatures c_1 and c_2 at every given point of the cell surface. Therefore, we can apply the Helfrich model to our specific system, the cells in a pseudostratified epithelium undergoing IKNM.

Given the geometry of these cells, we parameterise a single cell surface as a surface of revolution around its z-axis, where we define z to be the direction along the longest dimension of the cell, i.e. the apicobasal dimension. In this parameterisation, $\vec{R}$ becomes

$$\vec{R}(\phi,z) = \begin{pmatrix} x \\ y \\ z \end{pmatrix} = \begin{pmatrix} r(z)\cos\phi \\ r(z)\sin\phi \\ z \end{pmatrix} \tag{7.7}$$

where $r(z)$ is the radius of the cell at a given point z along its length and ϕ is the angle of rotation around the z-axis. Thus, we obtain

$$H = \frac{rr'' - \left(r'^2+1\right)}{2r\left(r'^2+1\right)^{3/2}} \tag{7.8}$$

$$K = -\frac{r''}{r\left(r'^2+1\right)^2} \tag{7.9}$$

$$\Delta = \frac{1}{r\left(r'^2+1\right)^{1/2}}\partial_\phi\left(\frac{\left(r'^2+1\right)^{1/2}}{r}\partial_\phi\right) + \frac{1}{r\left(r'^2+1\right)^{1/2}}\partial_z\left(\frac{r}{\left(r'^2+1\right)^{1/2}}\partial_z\right) \tag{7.10}$$

where $r' = \partial r/\partial z$ and $r'' = \partial^2 r/\partial z^2$. Note that there are no mixed terms (i.e. terms mixing derivatives ∂_ϕ and ∂_z) in the expression for Δ because the respective entries in g^{ij} are zero. Further note that H and K are independent of ϕ as we have parameterised the cell

surface as a surface of revolution. Therefore, we only need to take the second term of Δ into account for further calculations.

7.3.2 Obtaining the differential equation for $r(z)$

Based on the expressions above for H, K and Δ, we calculate the individual terms in Equation 3.19. We assume that there is no pressure difference between the inside and the outside of a cell, $\Delta p = 0$, because (neglecting the small apical and basal surfaces) each cell is surrounded only by other RPCs. Further, we assume that the membrane does not have an intrinsic curvature, c_0, and thus

$$-\sigma H + \kappa\left(2H^3 - 2KH\right) + \kappa\Delta H = 0. \tag{7.11}$$

Substituting H, K and Δ, we obtain a fourth order ordinary differential equation for the cell radius r as a function of the apocibasal distance z

$$\begin{aligned} r'''' = \frac{\partial^4 r}{\partial z^4} =& \frac{\sigma}{\kappa}\frac{1}{r}\left(rr'' - \left(r'^2+1\right)\right)\left(r'^2+1\right) \\ &- \frac{1}{2r^3\left(r'^2+1\right)^2}\left(rr'' - \left(r'^2+1\right)\right)^3 \\ &- \frac{1}{r}\left(2r'r'''\right) \\ &+ \frac{1}{r\left(r'^2+1\right)}\left(3r''^2\left(2r'^2-1\right)\right) \\ &+ \frac{1}{\left(r'^2+1\right)}\left(10r'r''r'''\right) \\ &- \frac{1}{\left(r'^2+1\right)^2}\left(3r''^3\left(5r'^2-1\right)\right) \\ &+ \frac{1}{r^2}\left(r''\left(r'^2+1\right)\right) \\ &+ \frac{1}{r^3}\left(r'^2\left(r'^2+1\right)\right) \end{aligned} \tag{7.12}$$

with $r' = \partial r/\partial z$, $r'' = \partial^2 r/\partial z^2$ and $r''' = \partial^3 r/\partial z^3$. This equation can now be solved numerically to obtain the equilibrium shape of RPC membranes.

7.4 Numerical determination of cell shapes

After having obtained the differential Equation 7.12 describing the shape of the cell membrane according to the Helfrich model, we now numerically solve for this shape. First, in Subsection 7.4.1, we specify the boundary conditions suitable for PSE cells. Then, we outline the numerical procedure in Subsection 7.4.2. Solving for the cell membrane shape involves several steps that build upon each other. First, in Subsection 7.4.3 we determine the shape only considering the existence of the nucleus in one single point; the point of the largest nuclear radius perpendicular to the z-axis. Then, we add the full size of the nucleus to our consideration in Subsection 7.4.4. This gives rise to multiple possible solutions of which we find the most likely one by energy minimisation in Subsection 7.4.5. Comparing theoretical cell shapes to a microscopy image of a real retinal progenitor cell, we conclude that the model employed here gives rise to qualitatively realistic solutions. As we utilize a range of values for the parameters in this model, our results might also be relevant for the study of other cell types with geometries similar to the one of RPCs. Finally, our calculated cell shapes enable us to assess the validity of the theory derived by Daniels [147] (used previously in Chapter 6) for the case of zebrafish retinal IKNM in Subsection 7.4.6.

7.4.1 Boundary conditions

Aiming to solve Equation 7.12 numerically, we first specify the boundary conditions determining the shape of the cell membrane in pseudostratified epithelia. Here, we opt to place the nucleus in the middle of the cell along the apicobasal axis, i.e. with its centre at $(z = L/2, r = 0)$. We then only solve for the apical half of the cell shape, i.e. for $0 \leq z \leq L/2$ where $z = 0$ denotes the apical tissue surface.

1. At the apical tissue surface, the cells should have an average radius given by the tissue surface area and the number of cells. Thus we fix $r = r_0$ at $z = 0$ (and later set $r_0 = \delta_a$ for the apical side of the tissue).
2. At the apical tissue surface, the lateral cell surface should be perpendicular to the tissue surface to ensure integrity of the tissue, its surface and the possibility of junctions between the cells. Therefore, $\partial r/\partial z = 0$ at $z = 0$.
3. We expect the cell membrane to enclose the nucleus tightly, as indicated e.g. by Norden [84] and theoretically predicted by Daniels [147] (compare Section 7.2). Therefore, we set $\partial r/\partial z = 0$ at $z = L/2$.

4. Finally, we expect the gap size between the nucleus and the membrane to be small around the nucleus and set $r = R_0$ with $R_0 = R$ or $R_0 = R_m$ at $z = L/2$.

These boundary conditions, together with Equation 7.12 fully specify the problem in the apical part of the cell $z \in [0, L/2]$.

In order to solve for the membrane shape in the basal part of the cell, we only need to exchange $r_0 = \delta_a$ with $r_0 = \delta_b$ in the first boundary condition and then mirror the numerical solution onto $z \in [L/2, L]$. Finally, to obtain the cell shape in cases in which the nucleus is not located exactly in the middle of the cell, we can use results for different values of L and simply combine a longer and a shorter piece.

7.4.2 Sequence of steps

As we have specified boundary conditions at two different positions, namely $z = 0$ and $z = L/2$, our problem becomes a two point boundary value problem (compare [157]). In MATLAB [127], different solvers already exist to handle such problems [158]. Here, we choose the solver bvp5c (because of its direct error control) [159]. This solver handles systems of first order ordinary differential equations, and the transformation of Equation 7.12 and the specified boundary conditions into such a system is straight forward.

bvp5c further requires an initial mesh as well as an initial guess of the solution. For the mesh, we use 2500 equally spaced points within $z \in [0, L/2]$. For the initial guess of the solution, it is recommended that the guess satisfies the boundary conditions [158]. A simple guess given our boundary conditions are a modified cosine function with its minimum at $(z = 0, r = r_0)$, its maximum at $(z = 0, r = R_0)$ and period L, and its derivatives. However, as it turns out, this guess is sometimes, but not always, good enough. Therefore, we often use previously obtained solutions and provide these as initial guesses for the next run of the solver. For example, when solving the problem for different lengths of the cell L, we map the solution obtained in a run with $L = L_1$ onto the mesh with $L = L_2$ to be used in the following run, and thus obtain an improved initial guess compared to the cosine function and its derivatives.

In general, we can expect the cell shape to depend on three different parameters, as there are four different length scales in our problem: the length of the cell L, the fixed radius of the membrane at the tissue boundary r_0, the fixed radius of the membrane around the centre of

the nucleus R_0, as well as $\sqrt{\kappa/\sigma}$, related to the prefactor in the first term of equation 7.12. Based on the biological situation, we have already established that we need to vary r_0 and L. Furthermore, we do not *a priori* know the exact value of the mebrane's bending rigidity κ and surface tension σ while we do know the average radius of membrane around the nuclei ($R_0 = R$ or $R_0 = R_m \approx R$) from our previous work (compare Chapters 5 and 6). Hence, in accord with the biological situation, we keep the radius of the membrane around the centre of the nucleus fixed and find solutions to the cell shape problem depending on r_0, L and σ.

We resolve the cell shape in three steps:

1. We solve the problem specified in Subsection 7.4.1 and analyse the resulting shapes.
2. If we find that all or some of the resulting shapes are incompatible with the presence of the nucleus inside the cell, which might affect the membrane in an entire region rather than just at $z = L/2$ (compare e.g. Figure 7.2 (b)), we run a second round of simulations. In those, we systematically vary the contact point between the membrane and nucleus and adapt the third and fourth boundary conditions accordingly.
3. Amongst the possible solutions for each set of parameters r_0, L and σ that are compatible with the presence of the nucleus, we identify the cell shape as the solution with the minimal energy, computable from Equation 3.18 with $c_0 = 0$, $\Delta p = 0$ and $c_1 + c_2 = -2H$.

7.4.3 Considering the nucleus in one point only

As described above, we first obtain the equilibrium shapes of the cell membrane solely based on Equation 7.12 with the boundary conditions specified in Subsection 7.4.1. Here, we use the following values for the occurring parameters:

- As the gap between nucleus and enclosing membrane is generally much smaller than the radius of the nucleus, as estimated in Subsection 7.4.6, we for now neglect the gap size and set $r(z = L/2) = R_0 = R$ with $R = 3.5$ µm as obtained previously (compare Chapters 5 and 6).
- We choose two different values for $r(z = 0) = r_0$, namely $r_0 = R_0$ and $r(z = 0) = 0.1R_0$ corresponding to a symmetrical and a strongly asymmetrical membrane shape. All possible cell surface radii determined earlier (see Table 7.1) lie in between these two extreme cases.
- We vary the length of the cell L in small steps between $L = 1$ µm and $L = 55$ µm, where the latter corresponds to the length of the actual RPCs in our main normal condition data set (compare Chapters 4, 5, and 6). Note that values of $L \leq 7$ µm are only used for

comparison as such cells would be shorter than the nuclei therein, given that $R = 3.5$ µm.

- For the temperature T we choose the incubation temperature of our experimental normal condition, i.e. $T = 301.65$ K equivalent to $T = 28.5$ °C.
- The Boltzmann constant is $k_B = 1.38 \times 10^{-23}$ m^{2}kg/s^{2}K, thus in the units used here it reads $k_B = 1.38 \times 10^{-11}$ µm^{2}kg/s^{2}K.
- For the bending rigidity of the cell membrane we choose $\kappa \approx 20 k_B T$, as in [147].
- For the surface tension Daniels [147] states $\sigma \approx 10^{-5}$ J/m^2 to 10^{-4} J/m^2, i.e. $\sigma \approx 10^{-5}$ kg/s^2 to 10^{-4} kg/s^2, and we have used this range of values previously for the calculations in Chapter 6 and Section 7.2. However, we find that this high tension regime is hard to resolve numerically. Therefore, we here vary σ between 10^{-10} kg/s^2 and 10^{-6} kg/s^2 and only discuss the regime of even higher tension qualitatively.

The resulting shape solutions are shown in Figure 7.3, with the left column of subfigures showing results for $r_0 = R_0$, the right column of subfigures showing results for $r_0 = 0.1R_0$, each line of subfigures showing results for a different value of σ and the differently coloured graphs in each panel representing the resulting shape for the various cell lengths L. For comparison all shapes are shown aligned at the centre of the nucleus. The area shaded in grey depicts the nucleus. This means, graphs intersecting the grey area are solutions incompatible with the presence of the nucleus, while graphs not intersecting the grey area belong to solutions describing possible cell shapes.

As the results in Figure 7.3 show, the relaxed membrane shape indeed depends on all three parameters varied here, r_0, L and σ.

Firstly, as is well-known and can easily be derived from Equation 7.12, the equilibrium radius of a cylindrical membrane tube r_{tube} changes depending on σ as $r_{\text{tube}} = \sqrt{\kappa/(2\sigma)}$. Comparing to the size of the nucleus, this means that for $\sigma \approx 3.4 \times 10^{-9}$ kg/s^2 the equilibrium tube radius is equal to the nuclear radius. For any σ smaller than this value the equilibrium tube radius becomes larger than the nucleus and hence the mebrane bulges outward while for any larger σ the membrane contracts.

Similarly, the distance over which the membrane radius changes from R_0 to r_{tube} depends on σ. Although larger values of σ correspond to smaller r_{tube} and thus to larger changes in membrane radius, the length scale of these changes decreases with increasing σ. Additionally, the length scale of radius changes also depends on the magnitude of the change, which is ap-

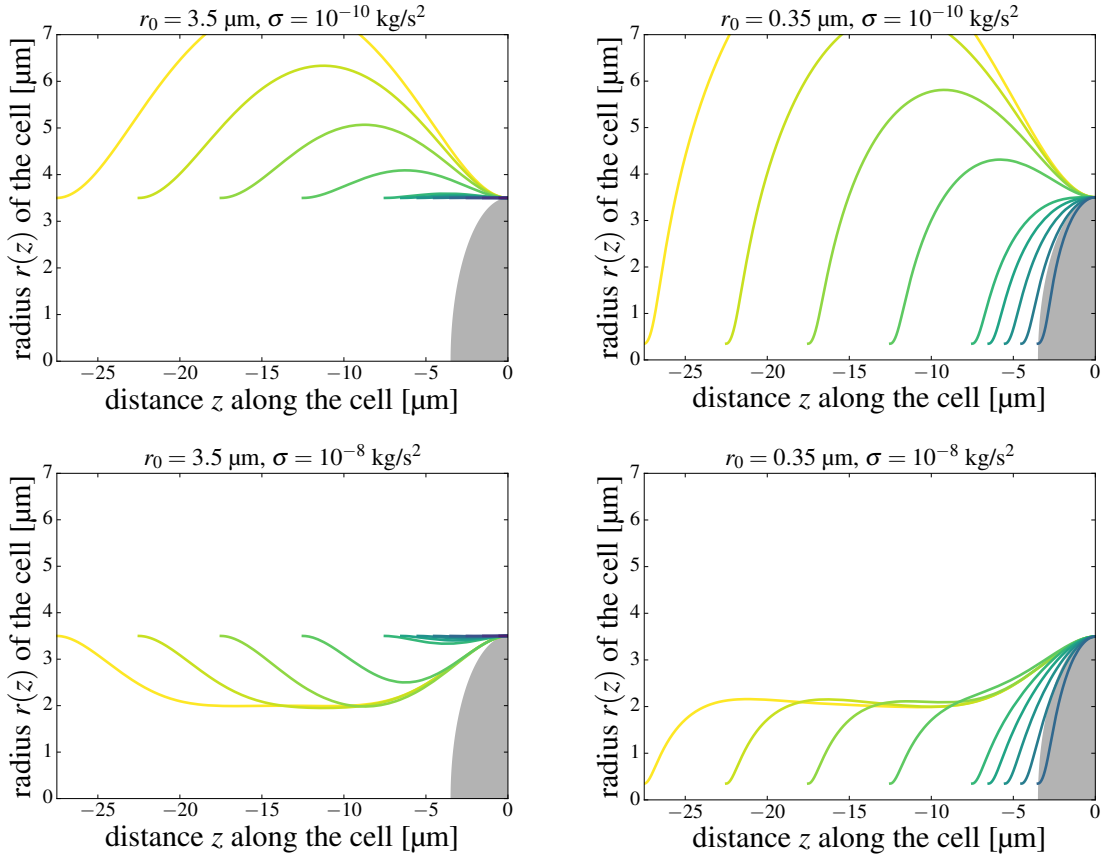

Figure 7.3 **Theoretical cell shapes with nuclear influence in one point only.** This figure shows the calculated cell shapes if the presence of the nucleus is only taken into account in the point $(z = L/2, r(z = L/2))$. The left column of plots represents the symmetric case $r_0 = R_0$ and the right column of plots the asymmetric case $r_0 = 0.1R_0$. Each line of plots shows results for a different value of the surface tension σ, with $\sigma = 10^{-10}$ kg/s^2, $\sigma = 10^{-8}$ kg/s^2, $\sigma = 10^{-7}$ kg/s^2 and $\sigma = 10^{-6}$ kg/s^2 from top to bottom (see also second part of this figure). The differently coloured lines depcit the respective solutions for various values of the cell length L from $L = 1$ µm (dark blue) to $L = 55$ µm (yellow) as indicated in the second part of this figure. The grey shaded area represents the size of the nucleus. Only solutions with graphs not intersecting this area are realistic.

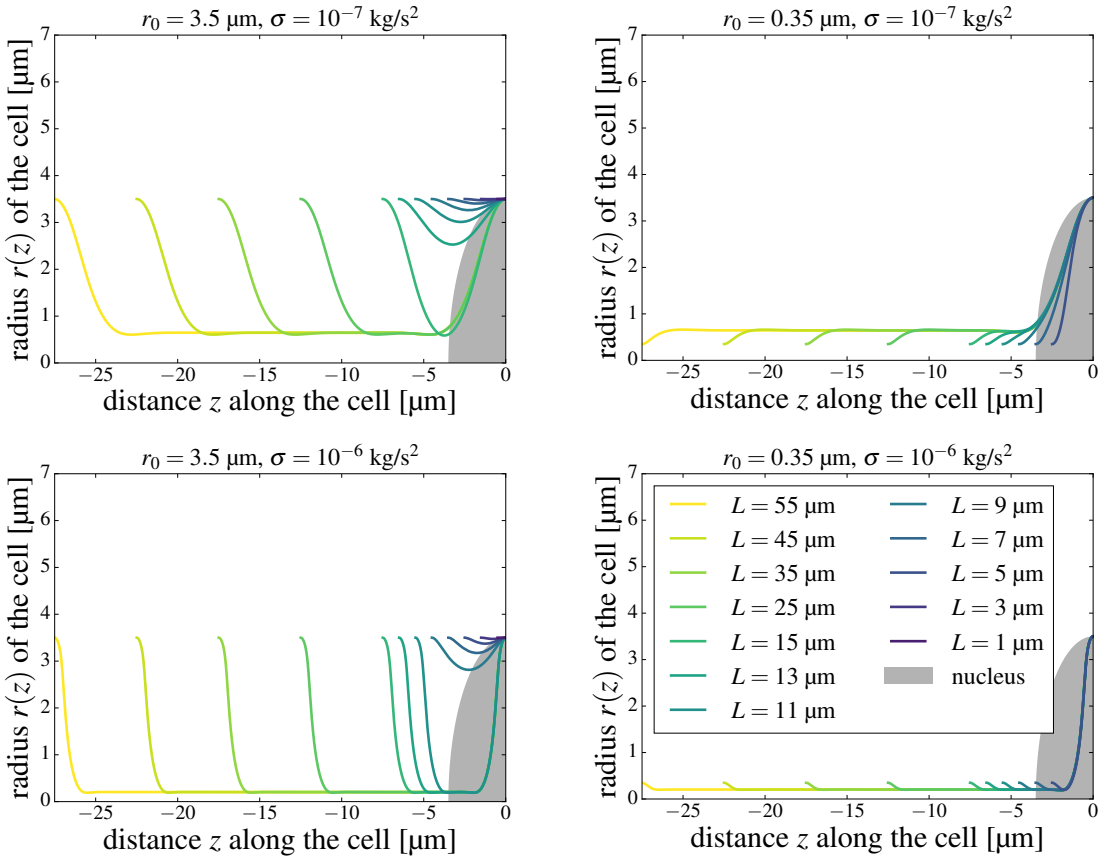

Figure 7.3 **Theoretical cell shapes with nuclear influence in one point only** (continued).

parent when comparing the two sides of the membrane in the asymmetric case where $r_0 \ll R_0$.

Furthermore, whether or not the membrane radius reaches r_{tube} depends on both r_0 and L. If $L/2$ is larger than the sum of the length scales needed for the membrane radius to make both transitions from R_0 to r_{tube} and from r_{tube} to r_0 then these transitions will take place. Else, the membrane radius will transitions fairly directly from R_0 to r_0 (both in the shortest asymmetric and symmetric cases, where in the latter the cells are approximately cylindrical) or change without reaching r_{tube} completely (e.g. for $L = 5$ µm to 13 µm in the case of $r_0 = 3.5$ µm and $\sigma = 10^{-7}$ kg/s^2).

In addition to the dependency of the membrane shape on r_0, L and σ, we can make another important observation from the graphs in Figure 7.3 (clearly visible especially for $\sigma = 10^{-6}$ kg/s^2). For cases with L large enough for the membrane to reach r_{tube}, a necking region can be observed at both ends of the tubular membrane part. This is analogous to the necking of membrane tethers described by Powers, Huber and Goldstein [160].

Finally, and most importantly in the context of finding actual possible cell shapes, Figure 7.3 provides a direct comparison between the relaxed membrane shapes and the size of the nucleus. As the different panels show, the plotted graphs intersect the area shaded in grey in many cases. Because the grey area depicts the size of the nucleus, these solutions cannot possibly represent realistic cell shapes. We therefore in the following select a number of cases for which we perform a second round of simulations as described in Subsection 7.4.2.

7.4.4 Fully considering the presence of the nucleus

So far, the presence of the nucleus was included in calculating the membrane shape only in one point, namely in $(z = L/2, r(z = L/2))$. However, as indicated above, in reality the nucleus might deform an entire region of the cell membrane (e.g. compare Figure 7.2 (b)).

Following Daniels [147], we assume that a region exists around the centre of the nucleus in which the membrane shape is determined by thermal fluctuations of the membrane. These fluctuations maintain a finite gap with constant average gap size between the membrane and the enclosed nucleus. We further assume that at some point $z_{\text{contact}} < L/2$ to be determined, the membrane looses its tight association with the nucleus and the gap between the two increases. In the following, in the region $z < z_{\text{contact}}$ the membrane shape is considered to be determined only by Equation 7.12 as previously, while in the region $z_{\text{contact}} \leq z \leq L/2$ the

membrane is considered to form a circular arc with radius R_m around the nucleus.

At the point $z = z_{\text{contact}}$ both parts of the membrane have to join together smoothly. Therefore, we change our boundary conditions and numerics to reflect this fact. For solving Equation 7.12 we now consider the region $z \in [0, z_{\text{contact}}]$ only. We vary z_{contact} (or rather, the corresponding radius r_{contact}) for each chosen combination of r_0, L and σ. Again, we subdivide our domain of interest, i.e. $z \in [0, z_{\text{contact}}]$, into 2500 equally spaced points for each run. At the new boundary $z = z_{\text{contact}}$ the boundary conditions become:

- $r = r_{\text{contact}}$ at $z = z_{\text{contact}}$ with $r_{\text{contact}}^2 + z_{\text{contact}}^2 = R_m^2$.
- $\partial r/\partial z = -(z_{\text{contact}} - L/2)/\sqrt{R_m^2 - (z_{\text{contact}} - L/2)^2}$ at $z = z_{\text{contact}}$, i.e. the derivative of $r(z)$ must be the same as the derivative of the circle with radius R_m at the contact point.

The boundary conditions at the cell surface stay the same as before, i.e. $r = r_0$ and $\partial r/\partial z = 0$ at $z = 0$.

Note that in this case, we take the gap size between the membrane and the nucleus into account by setting the radius of the membrane arc to R_m, while previously we have used $R_0 = R$. However, as $R_m \approx R_0$, this change does not have a significant effect on the membrane shape.

Figures 7.4 and 7.5 show the resulting membrane shapes depending on the choice of r_{contact} for a collection of different sets of parameters r_0, L and σ. In Figure 7.4 the results for $\sigma = 10^{-7}$ kg/s^2 and in Figure 7.5 the results for $\sigma = 10^{-6}$ kg/s^2 are shown. In both figures, the left column of subfigures contains plots with $r_0 = R_0$ and the right column of subfigures those with $r_0 = 0.1R_0$, while each line of subfigures represents a different value of L. The differently coloured graphs in each panel depict the membrane shapes for various chosen values of r_{contact}.

7.4.5 Energy minimisation determines final cell shapes

For each of these resulting cell shapes, we now calculate the total energy of the membrane. In order to be able to compare the energies of each individual membrane subsequently, we have to take both the shapes presented in Figures 7.4 and 7.5 and the corresponding membrane arcs around the nucleus into account. For the circular arc the negative mean curvature is simply $H_{\text{circle}} = -1/R_m$. Thus, including the rotational symmetry around the z-axis, the total energy of each membrane (with $z \in [0, L/2]$) becomes:

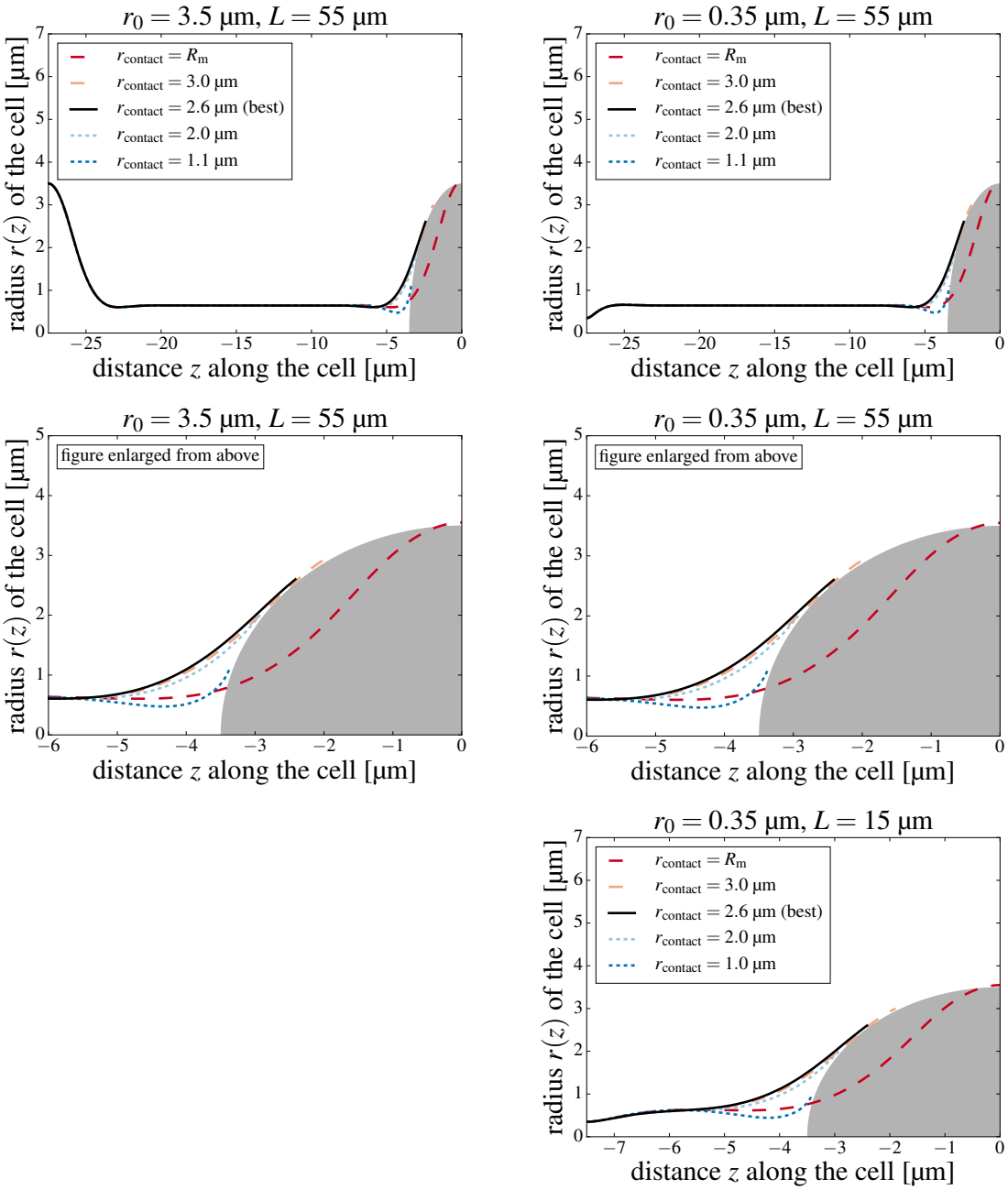

Figure 7.4 **Theoretical cell shapes for $\sigma = 10^{-7}$ kg/s^2 and various contact points.** This figure shows the calculated cell shapes within $z \in [0, z_{\text{contact}}]$ for $\sigma = 10^{-7}$ kg/s^2 if the presence of the nucleus is taken into account in a whole region $z \in [z_{\text{contact}}, L/2]$. The left column of plots represents the case $r_0 = R_0$ and the right column of plots the case $r_0 = 0.1R_0$. Each line of plots shows results for a different value of L, with the exception of the second line which shows an enlarged section of the plots directly above. The solutions for the missing plot could not be resolved numerically. The differently coloured lines depict the respective solutions for various values of the contact radius r_{contact} as indicated, with the respective best solution (as determined in Subsection 7.4.5) in black. The grey shaded area represents the size of the nucleus.

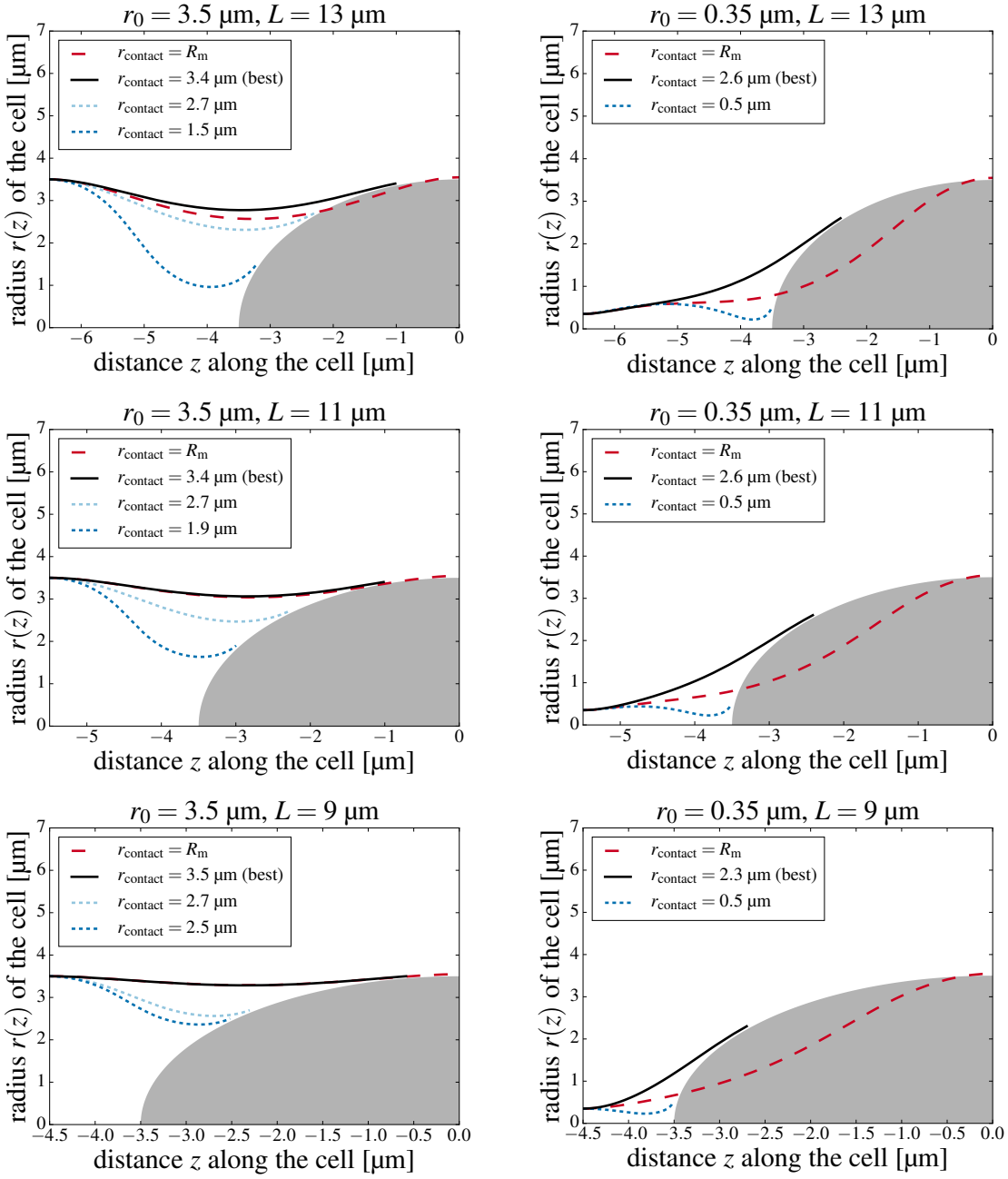

Figure 7.4 **Theoretical cell shapes for $\sigma = 10^{-7}$ kg/s^2 and various contact points** (continued).

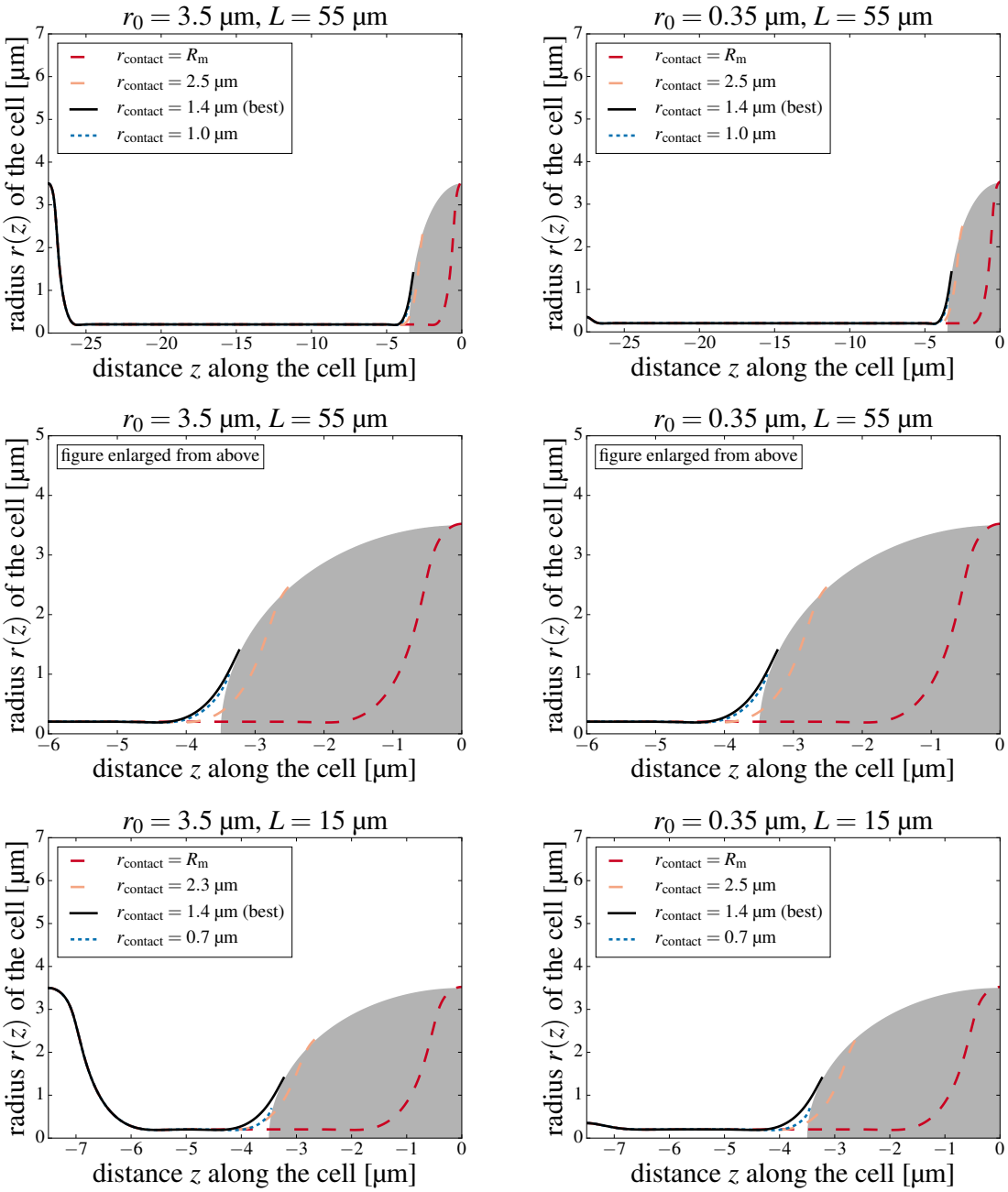

Figure 7.5 **Theoretical cell shapes for $\sigma = 10^{-6}$ kg/s^2 and various contact points.** This figure shows the calculated cell shapes within $z \in [0, z_{\text{contact}}]$ for $\sigma = 10^{-7}$ kg/s^2 if the presence of the nucleus is taken into account in a whole region $z \in [z_{\text{contact}}, L/2]$. The left column of plots represents the case $r_0 = R_0$ and the right column of plots the case $r_0 = 0.1R_0$. Each line of plots shows results for a different value of L, with the exception of the second line which shows an enlarged section of the plots directly above. The solutions for the missing plot (second part of figure) could not be resolved numerically. Differently coloured lines depict the respective solutions for various values of the contact radius r_{contact} as indicated, with the respective best solution (determined in Subsection 7.4.5) in black. The grey shaded area represents the size of the nucleus.

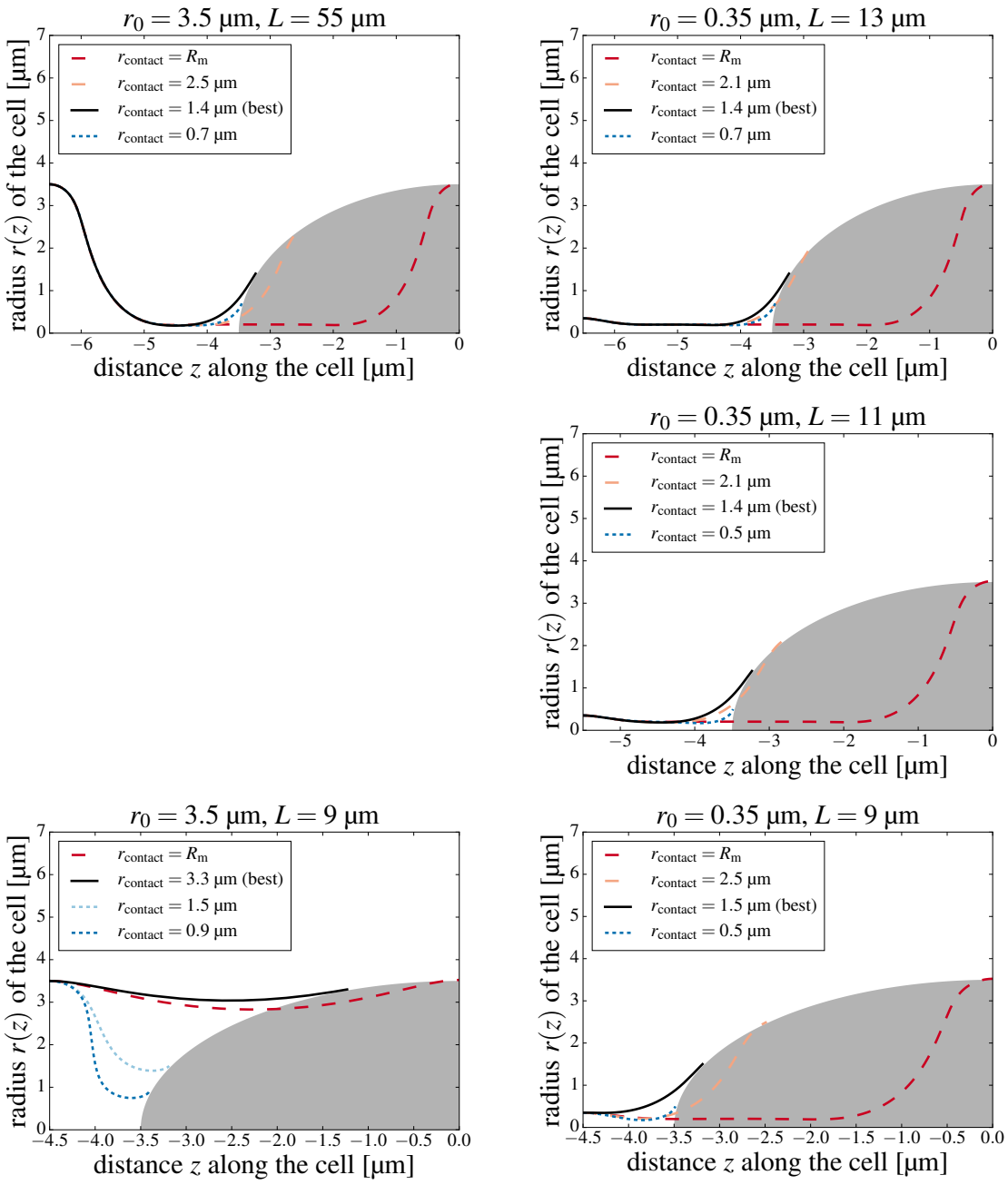

Figure 7.5 **Theoretical cell shapes for $\sigma = 10^{-6}$ kg/s^2 and various contact points** (continued).

$$\begin{aligned} E =& 4\pi\kappa \int_0^{z_{\text{contact}}} H^2 r\sqrt{1+r'^2}dz + 2\pi\sigma \int_0^{z_{\text{contact}}} r\sqrt{1+r'^2}dz \\ &+ \frac{4\pi\kappa}{R_m}\left(\frac{L}{2} - z_{\text{contact}}\right) + 2\pi\sigma R_m\left(\frac{L}{2} - z_{\text{contact}}\right). \end{aligned} \tag{7.13}$$

As the solutions for the membrane shape in $z \in [0, z_{\text{contact}}]$ are only known numerically, we calculate the first two integrals in equation 7.13 using the extended trapezoidal rule [157].

We further require that the curve of the solution for the membrane shape in in $z \in [0, z_{\text{contact}}]$ must not get closer to the nucleus than the membrane arc in $z \in [z_{\text{contact}}, L/2]$. Under this condition, we minimise the total membrane energy to find the most likely membrane shape. The solution in each case turns out to be the one where r_{contact} and z_{contact} have been chosen such that the resulting H in $z \in [0, z_{\text{contact}}]$ is equal to $H_{\text{circle}} = -1/R_m$ for $z \uparrow z_{\text{contact}}$.

The resulting approximate contact radii are listed in Table 7.2. The data in this table again shows the dependencies of the membrane shape on the parameters r_0, L and σ. With increasing σ, the contact radius decreases. Depending on r_0 and L, we also observe a transition between the contact point being located along the side of the nucleus and the contact point being located more or less directly on top of the nucleus. This accompanies the transition from $r(z)$ plateauing at r_{tube} to not reaching or only passing through r_{tube} described earlier. Again, with increasing σ this transition point occurs at decreasing values of L.

Having obtained the ideal contact points for different combinations of r_0, L and σ, we finally predict actual cell geometries and compare these with experimental data. In Figure 7.6 we show four possible solutions using $L = 55$ µm. Here, we also use actual values for the apical and basal cell radii δ_a and δ_b (as calculated in Section 7.2). The resulting shapes are thus predictions for combinations of the cell aspect ratios 15 and 20 with surface tension values $\sigma = 10^{-7}$ kg/s^2 and $\sigma = 10^{-6}$ kg/s^2. For $\sigma = 10^{-7}$ kg/s^2 a contact radius of $r_{\text{contact}} = 2.6$ µm is chosen while for $\sigma = 10^{-6}$ kg/s^2 the value $r_{\text{contact}} = 1.4$ µm is used.

For comparison with experimental data, Figure 7.7 (a) shows the same cell shapes as in the top line of Figure 7.6, now with axes to scale. An experimental image of a retinal progenitor cell is shown in Figure 7.7 (b). This image is extracted and cropped from a video which had been acquired by Tilak Das and has kindly been provided by Prof. William A. Harris (Department of Physiology, Development and Neuroscience, University of Cambridge). In this figure, we have scaled the predicted cell shapes and the experimental image such

Table 7.2 **Approximate membrane contact radii r_{contact}.** Here, the approximate contact radii r_{contact} at which the cell membrane transitions to a circular arc around the nucleus are listed for the various conditions plotted in Figures 7.4 and 7.5. These best solutions are determined based on energy minimisation (where the energy for each shape is calculated using Equation 7.13).

σ [kg/s^2]	r_0 [µm]	L [µm]	r_{contact} [µm]
10^{-7}	3.5	55	2.6 to 2.7
		15	not resolved
		13	3.4 to 3.5
		11	3.4 to 3.5
		9	3.5 to $R_m \approx 3.55$
10^{-7}	0.35	55	2.6 to 2.7
		15	2.6 to 2.7
		13	2.6 to 2.7
		11	2.6 to 2.7
		9	2.3 to 2.4
10^{-6}	3.5	55	1.4 to 1.5
		15	1.4 to 1.5
		13	1.4 to 1.5
		11	not resolved
		9	3.3 to 3.4
10^{-6}	0.35	55	1.4 to 1.5
		15	1.4 to 1.5
		13	1.4 to 1.5
		11	1.4 to 1.5
		9	1.5 to 1.6

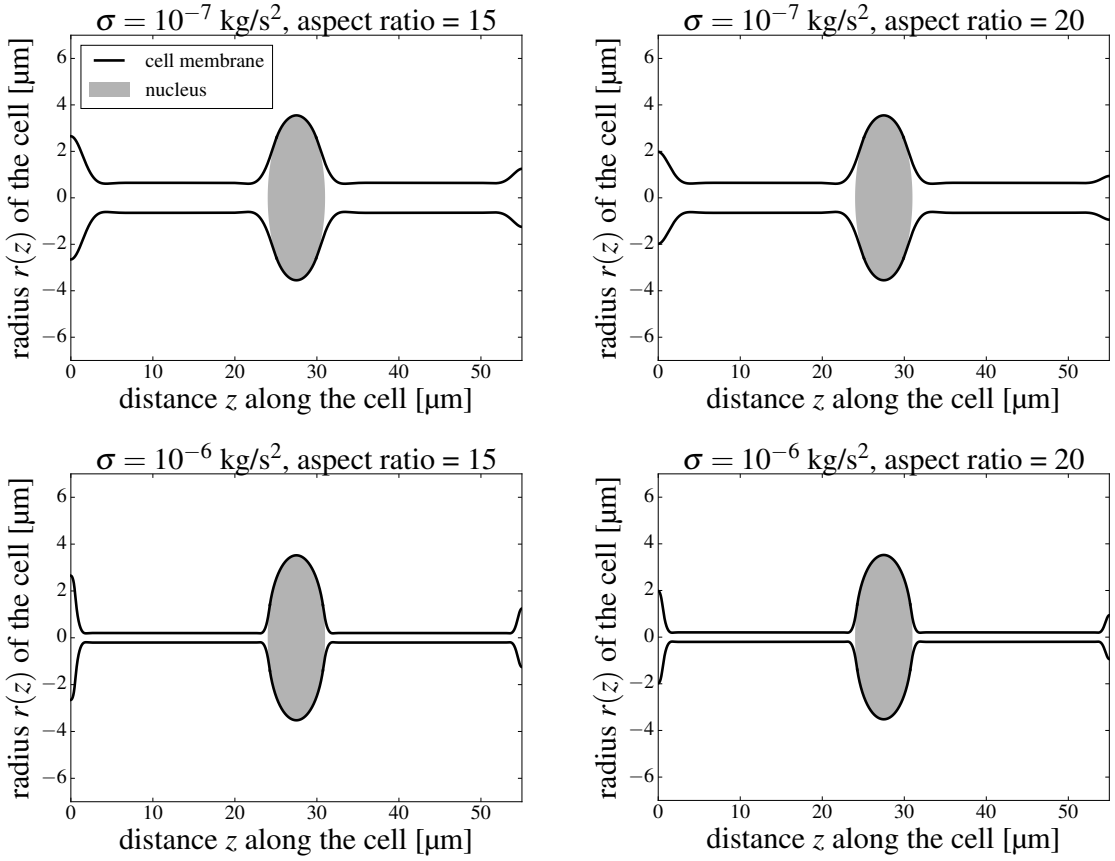

Figure 7.6 **Predicted RPC shapes.** This figure shows predicted shapes for retinal progenitor cells ($L = 55$ µm) as arising from the the Helfrich elastic model for lipid bilayers using the sequence of steps employed here. For these shapes, the apical and basal cell radii, δ_a and δ_b, calculated in Section 7.2 for cell aspect ratios 15 (left column of plots) and 20 (right column of plots) are used. The membrane geometries result from combinations of these aspect ratios and the optimised contact points for $\sigma = 10^{-7}$ kg/s^2 (top row) and $\sigma = 10^{-6}$ kg/s^2 (bottom row) with contact radii as provided in Table 7.2. The cell membrane is represented in black, the grey shaded area represents the nucleus.

that they have approximately the same apicobasal length. Given that RPCs are typically 50 - 60 µm long (compare Chapter 2) and that we used $L = 55$ µm for our predictions (the measure obtained from our own data set), this scaling makes it possible to evaluate the predicted shapes directly. As the images show, our predicted cell shapes, specifically the one generated with cell aspect ratio 15 (top picture in Figure 7.7 (a)), reproduce the apical and basal cell radii very well. This is somewhat to be expected, as the employed cell aspect ratios had been obtained from zebrafish retinas of the same developmental stage by Matejčić, Salbreux and Norden [136]. However, given that these authors only calculated the cell aspect ratios indirectly from the cell number and the average of apical and basal tissue areas, this agreement is also a valuable confirmation of the previously obtained results. Regarding the comparison of the overall cell shape, it might have been beneficial to have access to an experimental image where the nucleus is located more centrally within the cell, as its position close to the apical tissue surface might somewhat mask the apicalmost cellular shape. Nevertheless, the available image indicates that the RPC membrane contracts to a small tube radius over a short length scale close to the apical and basal cell surfaces, very similar to our prediction. Approximately in the middle of the experimental image, this tube radius is also comparable to the one shown in the theoretical plots, although we used a relatively small value of σ, namely $\sigma = 10^{-7}$ kg/s^2. Finally, even though we used a spherical nuclear shape while real RPC nuclei are more ellipsoidal, the experimental image clearly shows that the cell membrane encloses the nucleus tightly along its entire length and contracts to the small tube radius over a short length scale away from it, as we computed. This comparison between calculated and actual RPC shapes indicates that, using the sequence of steps above, the Helfrich elastic model for lipid bilayers can reproduce realistic RPC geometries.

7.4.6 The membrane opening angle is small in RPCs

Having obtained theoretical predictions for the RPC geometry, we can now, *a posteriori*, confirm the applicability of the theory devised by Daniels [147] for our system. To this end, we calculate the theoretical opening angle θ of the membrane tube, as depicted in Figure 7.2 (b). We set δ_m, the average tube radius depicted in Figure 7.2, to $\delta_m = r_{\text{tube}} = \sqrt{\kappa/(2\sigma)}$ and use R_m as in Equation 7.6. Thus

$$\sin(\theta) = \frac{\delta_m}{R_m}. \tag{7.14}$$

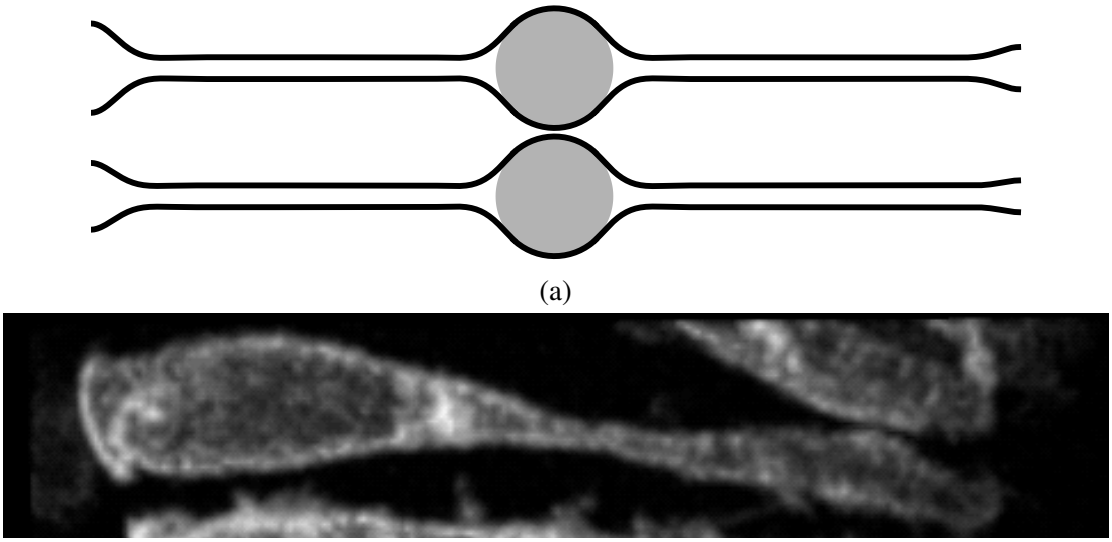

(a)

(b)

Figure 7.7 **Comparison between predicted and real RPC shapes.** (a) Shows the same predicted cell shapes as the top row in Figure 7.6, with axes to scale. For comparison, an experimental image of a RPC is provided in (b). This image has been extracted and cropped from a video which has acquired by Tilak Das and has kindly been provided by Prof. William A. Harris (Department of Physiology, Development and Neuroscience, University of Cambridge).

For $\sigma = 10^{-7}$ kg/s^2, the value used for the plots of computed cell shapes in Figure 7.7, we obtain $\theta \approx 0.1828 \approx 10.5°$ and for $\sigma = 10^{-6}$ kg/s^2 $\theta \approx 0.0580 \approx 3.3°$.

Equation 7.6 for the tube radius R_m, as well as the equations for the membrane's influence on the nuclear diffusion and friction constants used in Chapter 6, have been derived for the case of large membrane deformations, equivalent to small angles θ, by Daniels [147]. As the calculation above reveals, this condition hold true even for relatively small values of the membrane tension, e.g. $\sigma = 10^{-7}$ kg/s^2. Furthermore, θ further decreases with increasing σ. Therefore, we conclude that the theory devised by Daniels [147] is indeed applicable to IKNM in the zebrafish retina.

7.5 Discussion

In this Chapter, we have studied the geometry of cells in the retinal pseudostratified epithelium, as we had previously found a role of this geometry in determining the mobility of nuclei during IKNM. To this end, we first calculated the apical and basal cell radii based on

our experimental data and the available literature. Additionally, we estimated the radius of the membrane around the nucleus, which results to be $R_m \approx R$, leaving only a very small gap between the membrane and the nucleus.

Using the values for δ_a, δ_b and R_m, we then employed the Helfrich elastic model for lipid bilayers to compute more detailed cell membrane geometries. We noticed that (depending on the exact choice of parameters for σ, L and r_0) in many cases it was not enough to consider the presence of the nucleus in one point only. Instead, we had to take the shape of the nucleus into account in an entire region along the length of the cell. Then, energy minimisation led to the selection of the most likely one among the possible solutions for the cell shape. We found a good qualitative agreement between these theoreticaly predicted and experimentally observed cell shapes. Thus we conclude that the physical properties of the cell membrane, in interaction with the nucleus, appear to play a crucial role in determining the cell geometry in the zebrafish retinal pseudostratified epithelium.

Finally, we *a posteriori* confirmed the applicability of the theory derived by Daniels [147] to the case of PSE cells. Although we here used values for the surface tension σ smaller than those assumed in this study, we found the tube opening angle θ to be small enough for the theory by Daniels [147] to hold, even for $\sigma = 10^{-7}$ kg/s^2 or $\sigma = 10^{-6}$ kg/s^2.

We had previously applied the theory by Daniels [147] in Chapter 6 to estimate the change in diffusion constant and friction coefficent of the nucleus due to the presence of the membrane. In that Chapter, we had indeed used the larger surface tension values $\sigma = 10^{-5}$ kg/s^2 to $\sigma = 10^{-4}$ kg/s^2 stated by this author. Furthermore, we discussed that, probably, it is not the membrane alone but an interaction between the membrane and the underlying contractile so-called actin cortex that determines the overall surface tension of the cell. Although we did not explicitely specify this overall surface tension, we argued that the membrane tension alone might be a lower bound to its value. Now comparing the calculated cell shapes with the experimental image of a retinal PSE cell, it seems as if this might have been an overestimation of σ because the microscopy image compares well to shapes calculated for the much smaller surface tension $\sigma = 10^{-7}$ kg/s^2. In theory, a larger surface tension leads to a much smaller equilibrium tube radius r_{tube} which appears unlikely given the microscopy image. However, in the theoretical shape calculations, we have only taken the membrane and the presence of the nucleus into account. We therefore completely neglected the presence of any other intracellular components including the cytoskeleton and other organelles. Their presence will generally widen the radius of the cell in the same way the nucleus itself does,

even if the additional contractile actin cortex is present. For example the diameter of a single microtubule is approx. 25 nm [2], which by itself is already larger than the equilibrium tube radius for $\sigma = 10^{-4}$ kg/s^2, $r_{\text{tube}} \approx 20$ nm. Because cells certainly contain more than just a single cytoskeletal filament, other organelles might be present as well, and the thermal fluctuations of the cell membrane around these intracellular components also have to be taken into account (similarly to their role in maintaining a finite gap between the membrane and the nucleus) [161] [162] [147], the cellular radius appears very likely to be more similar to r_{tube} for $\sigma = 10^{-7}$ kg/s^2, $r_{\text{tube}} \approx 0.65$ µm, than to r_{tube} for $\sigma = 10^{-4}$ kg/s^2. In this sense, the numerical value of σ used in the computations might actually be better understood as an effective parameter, balancing the contractile forces of membrane and cortex with the extensile forces due to the presence of cytoplasmatic components.

Interestingly, for large L, we found necking regions at both ends of the tubular membrane part, analogous to the necking of membrane tethers studied previously by Powers, Huber and Goldstein [160]. These necks arise because bending and tension both play a role in determining the membrane shape in the junction regions [160]. Expanding on the comparison to the previously studied membrane tethers, very long RPCs might be though of, to a first approximation, as a chain of several membrane tethers linked together. In contrast, for small values of L, we found that the distance between the two boundaries with fixed cellular radii was not always large enough for the membrane to reach its equilibrium tube radius r_{tube} at all. In this case, the membrane shape is nearly cylindrical throughout. Taken together, these observations might provide an explanation for the varied cellular geometries that can be observed across the different types of pseudostratified epithelia [84]. If the elastic energy of the membrane (or of the combined membrane and cortex) really was playing a major role in determining the cellular shapes in these tissues, it would not be surprising to find cells in tissues with $L = 10$ µm to $L = 20$ µm (like the *Drosophila* optic lobe and endodermal organ buds [84]) to be nearly cylidrical while cells in a tissue with much larger thickness L would be expected to be thin cylidrical membrane tubes only bulging around their nuclei (as found in the zebrafish retinal PSE, or even more extremely pronounced in the radial glial cells of the mammalian brain, where $L \gg 100$ µm [84]).

Thinking this further, the elastic energy of the cell surface could potentially be an important factor in determining the shapes of other large cell as well. For example, the axons of neurons (large cellular appendices along which signals are transported to be transmitted to other cells) are tubular structures of up to 1 m in length in humans and are mainly filled with microtubules [2]. Although cytoskeletal components and the cellular surroundings are

known to be involved in regulating axonal growth [2], we speculate, based on the results presented here, that the physical properties of cell membranes and cortices might also play a role in determining the axons' thin, cylindrical geometry.

Chapter 8

Conclusion

In this dissertation, we have investigated three different physical aspects of interkinetic nuclear migration and pseudostratified epithelia.

First, we examined IKNM on the tissue scale. Based on our experimental data - a complete set of nuclear tracks within an entire section of the zebrafish retina - we confirmed the variability of nuclear movements during the majority of the cell cycle. This variability, although observed before [94] [92] [96], had so far not been studied on the whole tissue level. The data further enabled us to scrutinise how this variability comes to be. Previously, different hypotheses had been put forward, including the suggestion that G1 and S phase nuclei might move due to collisions with rapidly apicalward moving G2 phase nuclei [92] and the suggestion that the build-up of a nuclear concentration gradient might lead to G1 and S phase nuclei being pushed to areas with lower nuclear concentration, away from the apical tissue surface [86] [87] [103]. We found no evidence for the first hypothesis, but our data showed the existence and build-up of a nuclear concentration gradient and supported the idea of this concentration gradient being a main factor in creating the observed phenomonology of IKNM. We built upon all of these results and devised the first mathematical model for IKNM on the tissue level. The model describes the changes in nuclear concentration across the retinal tissue over time based on a diffusion equation, thus incorporating the apparent stochasticity of nuclear movements and the existence of a nuclear concentration gradient. In its nonlinear form it also includes a maximum nuclear packing density and with this is able to reproduce the nuclear distribution in the zebrafish retina over several hours of tissue development. This result unveils the importance of the overall tissue architecture for nuclear movements during IKNM and presents IKNM as a tissue wide, rather than a single cell phenomenon, suggesting that nuclear movements might be concentration-dependent.

Therefore, in the following, we examined IKNM on the cellular level to study the mechanism underlying this supposed concentration-dependence of nuclear movements. To this end, we first analysed the possible mechanisms underlying IKNM at low nuclear concentrations. We found that the nuclear mobility is much smaller than it would be in the case of free thermal diffusion, but it appears to be much higher than in the case of thermal diffusion within a tightly enveloping membrane tube. Therefore, we reasoned that nuclei must be driven by additional forces throughout the entire cell cycle. The average strength of these forces is compatible with cytoskeletal transport; a result that is also consistent with the observation that nuclear mobility is temperature-dependent independently of the well-known temperature-dependence of cell cycle times in zebrafish development. Based on these low concentration considerations, we devised possible Langevin models for individual nuclear movements within a high nuclear concentration environment. Stochastic simulations of these models and comparison to experimental data suggested that the model with concentration-dependent stochastic force is the one best describing the nuclear movements in the zebrafish retina. This result can be interpreted under the assumptions of cytoskeletal transport underlying IKNM - as indicated by our low concentration calculations - and of cells sensing the nuclear packing density. Given these assumptions, cells might recruit more cytoskeletal components to areas of high nuclear density, resulting in nuclei being transported away from these areas faster and thus having a concentration-dependent mobility.

Finally, because our calculations revealed the crucial importance of the cellular membrane in determining the mobility of individual nuclei even at low concentrations, we examined the cellular geometry of RPCs in closer detail. We found that considerations based on the elastic energy of the cell membrane, and taking the large size of the nucleus in comparison to the cell diameter into account, produced cell shapes not unlike those observed in experiments. Furthermore, the outcome from computations with varying cellular lengths led us to consider that the different cellular geometries found in different pseudostratified epithelia might all simply be due to the combination of cellular legths and membrane easticity.

Summarising all of the above results, we made considerable progress in scrutinising the mechanisms underlying the apparently stochastic movements of nuclei during the majority of IKNM. We provided quantitative mathematical descriptions for both the distribution of nuclei across the tissue over time as well as for the trajectories of individual nuclei. Our models suggest that IKNM has to be understood as a tissue wide phenomenon, in which tissue architecture, cellular geometry and nuclear packing density all play crucial roles. Additionally, our calculations indicated that cytoskeletal transport is likely underlying the

nuclear movements throughout the entire cell cycle, not just during the rapid apicalward movements of nuclei during G2. Finally, our considerations of cellular geometries hint at the membrane (or effective cell surface) elasticity as a potential explanation for the variety of cell shapes found in the different types of pseudostratified epithelia.

Despite this progress, many questions concerning IKNM remain.

Probably most importantly, the exact link between IKNM and cell differentiation is still unclear. Previously, a role of the nuclear distribution in regulating cell fate decision making had been suggested [99] [87] [103]. However, this role is still under debate. Given the ubiquity of pseudostratified epithelia during the embryonic development in a broad rage of animals [84] [85] [92] [89] [8] [96] [99] [88] [7] [94] [86] [87] [100] [105] [163], as well as the negative implications for tissue differentiation when apical nuclear localisation cannot be established during proliferative cell divisions [101] [102] [84] [87], it appears paramount to understand the link between cell fates and IKNM. The mathematical models for IKNM derived here might provide the starting point to do so. In the future, combining them with experiments imaging nuclei throughout the entire course of tissue development until eventual cell differentiation, could ultimately lead to conclusive insights regarding this connection.

Considering a different line of enquiry, the intracellular mechanisms for nuclear movements during G1 and S phase have not received much attention so far. Here we found that cytoskeletal transport might be involved in IKNM throughout the entire cell cycle, as some preceding studies implicated [110] [111]. However, further experimental investigations appear to be required in order to elucidate exactly which cytoskeletal components play a role and whether their contribution is equal in all types of PSE tissues [109].

Finally, when examining the cellular geometry of retinal progenitor cells, we found that lower values of the surface tension than reported [147] resulted in good qualitative agreement between calculated and experimental RPC shapes. Although the discrepancy might be explained by the presence of the cytoskeleton and other organelles, which had not been taken into account in our theoretical considerations, it would certainly be beneficial to study this aspect in more detail. For example, experimental measurements of RPC membrane tension might be undertaken in order to establish the exact value of this parameter. In addition, obtaining a more complete picture of the cellular contents of RPCs as well as their spatial arrangement during the developmental phase examined here would provide valuable input

for more precise models of RPC geometry and of the nuclear mobility during IKNM.

References

[1] D. C. Hodgkin, *Address to the University Students on the Evening of December 10, 1964*, Permission to reproduce this text has been granted by The Nobel Foundation, https://www.nobelprize.org/prizes/chemistry/1964/hodgkin/speech/.

[2] B. Alberts et al., 'Molekularbiologie der Zelle', 5. edition (WILEY-VCH, 2011).

[3] C. Mora et al., 'How Many Species Are There on Earth and in the Ocean?', *PLoS Biology* **9**, e1001127 (2011).
DOI: 10.1371/journal.pbio.1001127.

[4] Y. Roskov et al., *Species 2000 & ITIS Catalogue of Life, 2019 Annual Checklist*, 2019, http://www.catalogueoflife.org/annual-checklist/2019/info/ac (visited on 29/12/2019).

[5] E. Bianconi et al., 'An estimation of the number of cells in the human body', *Annals of Human Biology* **40**, 463–471 (2013).
DOI: 10.3109/03014460.2013.807878.

[6] J. E. Sulston et al., 'The Embryonic Cell Lineage of the Nematode Caenorhabditis elegans', *Developmental Biology* **100**, 64–119 (1983).
DOI: 10.1016/0012-1606(83)90201-4.

[7] F. C. Sauer, 'Mitosis in the neural tube', *Journal of Comparative Neurology* **62**, 377–405 (1935).
DOI: 10.1002/cne.900620207.

[8] H. Boije et al., 'The Independent Probabilistic Firing of Transcription Factors: A Paradigm for Clonal Variability in the Zebrafish Retina', *Developmental Cell* **34**, 532–543 (2015).
DOI: 10.1016/j.devcel.2015.08.011.

[9] A. Avanesov and J. Malicki, 'Analysis of the retina in the zebrafish model', *Methods in Cell Biology* **100**, 153–204 (2010).
DOI: 10.1016/B978-0-12-384892-5.00006-2.

[10] O.-Y. Zhong-can and W. Helfrich, 'Bending energy of vesicle membranes: General expressions for the first, second, and third variation of the shape energy and applications to spheres and c ylinders', *Physical Review A* **39**, 5280–5288 (1989).

[11] A. Azizi, 'Interplay between interkinetic nuclear migration and cell fate determination in the developing zebrafish retina', PhD thesis (University of Cambridge, 2018).

[12] CERN, *The Standard Model*, https://home.cern/science/physics/standard-model (visited on 05/08/2019).

[13] F. Reif, 'Fundamentals of statistical and thermal physics' (McGraw-Hill, Inc., 1965).

[14] K. Huang, 'Statistical mechanics', 2. edition (John Wiley & Sons, Inc., 1987).

[15] R. Livi and P. Politi, 'Nonequilibrium Statistical Physics' (Cambridge University Press, Cambridge, 2017).

[16] S. Rulands and B. D. Simons, 'Emergence and universality in the regulation of stem cell fate', *Current Opinion in Systems Biology* **5**, 57–62 (2017).
DOI: 10.1016/j.coisb.2017.08.001.

[17] R. J. Allen and B. Waclaw, 'Bacterial growth: a statistical physicist's guide', *Reports on Progress in Physics* **82**, 016601 (2019).
DOI: 10.1088/1361-6633/aae546.

[18] X. Trepat and E. Sahai, 'Mesoscale physical principles of collective cell organization', *Nature Physics* **14**, 671–682 (2018).
DOI: 10.1038/s41567-018-0194-9.

[19] I. D. Couzin, 'Collective animal migration', *Current Biology* **28**, R976–R980 (2018).
DOI: 10.1016/j.cub.2018.04.044.

[20] P. Gross, K. V. Kumar and S. W. Grill, 'How Active Mechanics and Regulatory Biochemistry Combine to Form Patterns in Development', *Annual Review of Biophysics* **46**, 337–356 (2017).
DOI: 10.1146/annurev-biophys-070816-033602.

[21] H. Debelius and R. H. Kuiter, 'Atlas mondial des nudibranches' (Ulmer, Paris, 2007).

[22] M. Watanabe and S. Kondo, 'Is pigment patterning in fish skin determined by the Turing mechanism?', *Trends in Genetics* **31**, 88–96 (2015).
DOI: 10.1016/j.tig.2014.11.005.

[23] L. Manukyan et al., 'A living mesoscopic cellular automaton made of skin scales', *Nature* **544**, 173–179 (2017).
DOI: 10.1038/nature22031.

[24] J. C. B. Petersen, 'An identification system for zebra (Equus burchelli, Gray)', *African Journal of Ecology* **10**, 59–63 (1972).
DOI: 10.1111/j.1365-2028.1972.tb00858.x.

[25] J. C. A. Mayer, 'Anatomische Kupfertafeln nebst dazu gehörigen Erklärungen (Band 4): Eilf Kupfertafeln von den Sinnwerkzeugen und den Brüsten' (Georg Jacob Decker und Sohn, Berlin, 1788), http://digi.ub.uni-heidelberg.de/diglit/mayer1788bd4.

[26] K. J. Lee, R. E. Goldstein and E. C. Cox, 'Resetting wave forms in Dictyostelium territories', *Physical Review Letters* **87**, 068101 (2001).
DOI: 10.1103/PhysRevLett.87.068101.

[27] A. H. Knoll, 'The Multiple Origins of Complex Multicellularity', *Annual Review of Earth and Planetary Sciences* **39**, 217–239 (2011).
DOI: 10.1146/annurev.earth.031208.100209.

[28] G. Karp, 'Cell Biology', Int. 7 edition (John Wiley & Sons, Inc., Singapore, 2014).

[29] R. Kolter and E. P. Greenberg, 'The superficial life of microbes', *Nature* **441**, 300–302 (2006).
DOI: 10.1038/441300a.

[30] J. B. Kirkegaard and R. E. Goldstein, 'Filter-feeding, near-field flows, and the morphologies of colonial choanoflagellates', *Physical Review E* **94**, 052401 (2016).
DOI: 10.1103/PhysRevE.94.052401.

[31] W. C. Ratcliff et al., 'Experimental evolution of multicellularity', *Proceedings of the National Academy of Sciences of the United States of America* **109**, 1595–1600 (2012).
DOI: 10.1073/pnas.1115323109.

[32] W. C. Ratcliff et al., 'Experimental evolution of an alternating uni- and multicellular life cycle in Chlamydomonas reinhardtii', *Nature Communications* **4**, 2742 (2013).
DOI: 10.1038/ncomms3742.

[33] K. J. Niklas and S. A. Newman, 'The origins of multicellular organisms', *Evolution and Development* **15**, 41–52 (2013).
DOI: 10.1111/ede.12013.

[34] K. J. Niklas, 'The evolutionary-developmental origins of multicellularity', *American Journal of Botany* **101**, 6–25 (2014).
DOI: 10.3732/ajb.1300314.

[35] R. E. Goldstein, 'Green Algae as Model Organisms for Biological Fluid Dynamics', *Annual Review of Fluid Mechanics* **47**, 343–375 (2015).
DOI: 10.1146/annurev-fluid-010313-141426.

[36] J. F. Ryan et al., 'The Genome of the Ctenophore Mnemiopsis leidyi and its Implications for Cell Type Evolution', *Science* **342**, 1242592 (2013).
DOI: 10.1126/science.1242592.

[37] M. Srivastava et al., 'The Amphimedon queenslandica genome and the evolution of animal complexity', *Nature* **466**, 720–726 (2010).
DOI: 10.1038/nature09201.

[38] M. Srivastava et al., 'The Trichoplax genome and the nature of placozoans', *Nature* **454**, 955–960 (2008).
DOI: 10.1038/nature07191.

[39] N. W. Blackstone, 'A new Look at Some Old Animals', *PLoS Biology* **7**, 29–31 (2009).
DOI: 10.1371/journal.pbio.1000007.

[40] S. F. Gilbert and M. J. F. Barresi, 'Developmental Biology', 11 edition (Sinauer Associates, Inc., Sunderland, MA, 2016).

[41] N. King et al., 'The genome of the choanoflagellate Monosiga brevicollis and the origin of metazoans', *Nature* **451**, 783–788 (2008).
DOI: 10.1038/nature06617.

[42] D. J. Richter and N. King, 'The Genomic and Cellular Foundations of Animal Origins', *Annual Review of Genetics* **47**, 509–537 (2013).
DOI: 10.1146/annurev-genet-111212-133456.

[43] M. Merkel et al., 'Triangles bridge the scales: Quantifying cellular contributions to tissue deformation', *Physical Review E* **95**, 032401 (2017).
DOI: 10.1103/PhysRevE.95.032401.

[44] M. Popović et al., 'Active dynamics of tissue shear flow', *New Journal of Physics* **19**, 033006 (2017).
DOI: 10.1088/1367-2630/aa5756.

[45] M. S. Steinberg, 'On the mechanism of tissue reconstruction by dissociated cells, I. population kinetics, differential adhesiveness, and the absence of directed migration', *Proceedings of the National Academy of Sciences of the United States of America* **48**, 1577–1582 (1962).

[46] M. S. Steinberg, 'Mechanism of Tissue Reconstruction by Dissociated Cells, II: Time-Course of Events', *Science* **137**, 762–763 (1962).
DOI: 10.1126/science.137.3532.762.

[47] M. S. Steinberg, 'On the mechanism of tissue reconstruction by dissociated cells, III. free energy relations and the reorganization of fused, heteronomic tissue fragments', *Proceedings of the National Academy of Sciences of the United States of America* **48**, 1769–1776 (1962).

[48] M. S. Steinberg, 'Differential adhesion in morphogenesis: a modern view', *Current Opinion in Genetics & Development* **17**, 281–286 (2007).
DOI: 10.1016/j.gde.2007.05.002.

[49] O. Voiculescu et al., 'The amniote primitive streak is defined by epithelial cell intercalation before gastrulation', *Nature* **449**, 1049–1052 (2007).
DOI: 10.1038/nature06211.

[50] O. Voiculescu et al., 'Local cell interactions and self-amplifying individual cell ingression drive amniote gastrulation', *eLife* **3**, 1–26 (2014).
DOI: 10.7554/eLife.01817.001.

[51] L. Przybyla, J. M. Muncie and V. M. Weaver, 'Mechanical Control of Epithelial-to-Mesenchymal Transitions in Development and Cancer', *Annual Review of Cell and Developmental Biology* **32**, 527–554 (2016).
DOI: 10.1146/annurev-cellbio-111315-125150.

[52] C. M. Waters and B. L. Bassler, 'Quorum Sensing: Cell-to-Cell Communication in Bacteria', *Annual Review of Cell and Developmental Biology* **21**, 319–346 (2005).
DOI: 10.1146/annurev.cellbio.21.012704.131001.

[53] M. Romanova-Michaelides et al., 'The wing and the eye: A parsimonious theory for scaling and growth control?', *Wiley Interdisciplinary Reviews: Developmental Biology* **4**, 591–608 (2015).
DOI: 10.1002/wdev.195.

[54] T. Gregor et al., 'Diffusion and scaling during early embryonic pattern formation', *Proceedings of the National Academy of Sciences of the United States of America* **102**, 18403–18407 (2005).
DOI: 10.1073/pnas.0509483102.

[55] P. B. Rainey and S. De Monte, 'Resolving Conflicts During the Evolutionary Transition to Multicellular Life', *Annual Review of Ecology, Evolution, and Systematics* **45**, 599–620 (2014).
DOI: 10.1146/annurev-ecolsys-120213-091740.

[56] A. M. Turing, 'The chemical basis of morphogenesis', *Philosophical Transactions of the Royal Society of London. Series B, Biological Sciences* **237**, 37–72 (1952).

[57] F. C. Werner, 'Wortelemente lateinisch-griechischer Fachausdrücke in den biologischen Wissenschaften', 1. edition (Suhrkamp, 1972).

[58] G. M. Cooper and R. E. Hausman, 'The Cell. A Molecular Approach', Int. 7 edition (Sinauer Associates Oxford University Press, New York, Oxford, 2018).

[59] X. Wang et al., 'Mechanical stability of the cell nucleus - roles played by the cytoskeleton in nuclear deformation and strain recovery', *Journal of Cell Science* **131**, jcs209627 (2018).
DOI: 10.1242/jcs.209627.

[60] P. Isermann and J. Lammerding, 'Nuclear Mechanics and Mechanotransduction in Health and Disease', *Current Biology* **23**, R1113–R1121 (2013).
DOI: 10.1016/j.cub.2013.11.009.

[61] C. M. Denais et al., 'Nuclear envelope rupture and repair during cancer cell migration', *Science* **352**, 353–358 (2016).
DOI: 10.1126/science.aad7297.

[62] K. V. Kardong, 'Vertebrates. Comparative Anatomy, Function, Evolution', Int. 6 edition (McGraw-Hill, New York, 2012).

[63] A. Martinez Arias, J. Nichols and C. Schröter, 'A molecular basis for developmental plasticity in early mammalian embryos', *Development* **140**, 3499–3510 (2013).
DOI: 10.1242/dev.091959.

[64] G. Kumano and H. Nishida, 'Ascidian embryonic development: An emerging model system for the study of cell fate specification in chordates', *Developmental Dynamics* **236**, 1732–1747 (2007).
DOI: 10.1002/dvdy.21108.

[65] P. Lemaire, 'Unfolding a chordate developmental program, one cell at a time: Invariant cell lineages, short-range inductions and evolutionary plasticity in ascidians', *Developmental Biology* **332**, 48–60 (2009).
DOI: 10.1016/j.ydbio.2009.05.540.

[66] P. Lemaire, 'Evolutionary crossroads in developmental biology: The tunicates', *Development* **138**, 2143–2152 (2011).
DOI: 10.1242/dev.048975.

[67] J. R. Priess and J. N. Thomson, 'Cellular Interactions in Early C. elegans Embryos', *Cell* **48**, 241–250 (1987).
DOI: 10.1016/0092-8674(87)90427-2.

[68] E. S. Rittershaus, S.-H. Baek and C. M. Sassetti, 'The Normalcy of Dormancy: Common Themes in Microbial Quiescence', *Cell Host and Microbe* **13**, 643–651 (2013).
DOI: 10.1016/j.chom.2013.05.012.

[69] A. Sturm and J. Dworkin, 'Phenotypic Diversity as a Mechanism to Exit Cellular Dormancy', *Current Biology* **25**, 2272–2277 (2015).
DOI: 10.1016/j.cub.2015.07.018.

[70] G. Balázsi, A. van Oudenaarden and J. J. Collins, 'Cellular Decision Making and Biological Noise: From Microbes to Mammals', *Cell* **144**, 910–925 (2011).
DOI: 10.1016/j.cell.2011.01.030.

[71] I. Golding, 'Decision Making in Living Cells: Lessons from a Simple System', *Annual Review of Biophysics* **40**, 63–80 (2011).
DOI: 10.1146/annurev-biophys-042910-155227.

[72] A. Raj and A. van Oudenaarden, 'Nature, Nurture, or Chance: Stochastic Gene Expression and Its Consequences', *Cell* **135**, 216–226 (2008).
DOI: 10.1016/j.cell.2008.09.050.

[73] R. Vassar, J. Ngai and R. Axel, 'Spatial Segregation of Odorant Receptor Expression in the Mammalian Olfactory Epithelium', *Cell* **74**, 309–318 (1993).
DOI: 10.1016/0092-8674(93)90422-M.

[74] A. Degl'Innocenti and A. D'Errico, 'Regulatory Features for Odorant Receptor Genes in the Mouse Genome', *Frontiers in Genetics* **8**, 19 (2017).
DOI: 10.3389/fgene.2017.00019.

[75] E. Clayton et al., 'A single type of progenitor cell maintains normal epidermis', *Nature* **446**, 185–189 (2007).
DOI: 10.1038/nature05574.

[76] S. Rulands and B. D. Simons, 'Tracing cellular dynamics in tissue development, maintenance and disease', *Current Opinion in Cell Biology* **43**, 38–45 (2016).
DOI: 10.1016/j.ceb.2016.07.001.

[77] C. L. G. J. Scheele et al., 'Identity and dynamics of mammary stem cells during branching morphogenesis', *Nature* **542**, 313–317 (2017).
DOI: 10.1038/nature21046.

[78] J. B. Gurdon, 'A community effect in animal development', *Nature* **336**, 772–774 (1988).

[79] J. B. Gurdon et al., 'A community effect in muscle development', *Current Biology* **3**, 1–11 (1993).

[80] J. B. Gurdon, P. Lemaire and K. Kato, 'Community Effects and Related Phenomena in Development', *Cell* **75**, 831–834 (1993).

[81] Y. Saka et al., 'Theoretical basis of the community effect in development', *BMC Systems Biology* **5**, 54 (2011).
DOI: 10.1186/1752-0509-5-54.

[82] L. Robb and P. P. L. Tam, 'Gastrula organiser and embryonic patterning in the mouse', *Seminars in Cell and Developmental Biology* **15**, 543–554 (2004).
DOI: 10.1016/j.semcdb.2004.04.005.

[83] E. M. De Robertis, 'Spemann's organizer and the self-regulation of embryonic fields', *Mechanisms of Development* **126**, 925–941 (2009).
DOI: 10.1016/j.mod.2009.08.004.

[84] C. Norden, 'Pseudostratified epithelia – cell biology, diversity and roles in organ formation at a glance', *Journal of Cell Science* **130**, 1859–1863 (2017).
DOI: 10.1242/jcs.192997.

[85] E. J. Meyer, A. Ikmi and M. C. Gibson, 'Interkinetic nuclear migration is a broadly conserved feature of cell division in pseudostratified epithelia', *Current Biology* **21**, 485–491 (2011).
DOI: 10.1016/j.cub.2011.02.002.

[86] Y. Kosodo et al., 'Regulation of interkinetic nuclear migration by cell cycle-coupled active and passive mechanisms in the developing brain', *The EMBO Journal* **30**, 1690–1704 (2011).
DOI: 10.1038/emboj.2011.81.

[87] M. Okamoto et al., 'TAG-1-assisted progenitor elongation streamlines nuclear migration to optimize subapical crowding', *Nature Neuroscience* **16**, 1556–1566 (2013).
DOI: 10.1038/nn.3525.

[88] A. Murciano et al., 'Interkinetic Nuclear Movement May Provide Spatial Clues to the Regulation of Neurogenesis', *Molecular and Cellular Neuroscience* **21**, 285–300 (2002).
DOI: 10.1006/mcne.2002.1174.

[89] J. He et al., 'How Variable Clones Build an Invariant Retina', *Neuron* **75**, 786–798 (2012).
DOI: 10.1016/j.neuron.2012.06.033.

[90] R. Wetts and S. E. Fraser, 'Multipotent Precursors Can Give Rise to All Major Cell Types of the Frog Retina', *Science* **239**, 1142–1145 (1988).
DOI: 10.1126/science.2449732.

[91] A. D. Almeida et al., 'Spectrum of Fates: a new approach to the study of the developing zebrafish retina', *Development* **141**, 1971–1980 (2014).
DOI: 10.1242/dev.104760.

[92] C. Norden et al., 'Actomyosin Is the Main Driver of Interkinetic Nuclear Migration in the Retina', *Cell* **138**, 1195–1208 (2009).
DOI: 10.1016/j.cell.2009.06.032.

[93] H. Boije, R. B. MacDonald and W. A. Harris, 'Reconciling competence and transcriptional hierarchies with stochasticity in retinal lineages', *Current Opinion in Neurobiology* **27**, 68–74 (2014).
DOI: 10.1016/j.conb.2014.02.014.

[94] L. M. Baye and B. A. Link, 'Interkinetic Nuclear Migration and the Selection of Neurogenic Cell Divisions during Vertebrate Retinogenesis', *The Journal of Neuroscience* **27**, 10143–10152 (2007).
DOI: 10.1523/JNEUROSCI.2754-07.2007.

[95] F. Del Bene, 'Interkinetic nuclear migration: Cell cycle on the move', *EMBO Journal* **30**, 1676–1677 (2011).
DOI: 10.1038/emboj.2011.114.

[96] L. Leung et al., 'Apical migration of nuclei during G2 is a prerequisite for all nuclear motion in zebrafish neuroepithelia', *Development* **138**, 5003–5013 (2011).
DOI: 10.1242/dev.071522.

[97] R. L. Sidman, I. L. Miale and N. Feder, 'Cell Proliferation and Migration in the Primitive Ependymal Zone; An Autoradiographic Study of Histogenesis in the Nervous System', *Experimental Neurology* **1**, 322–333 (1959).
DOI: 10.1016/0014-4886(59)90024-X.

[98] A. P. Barrasso et al., 'Live imaging of developing mouse retinal slices', *Neural Development* **13**, 23 (2018).
DOI: 10.1186/s13064-018-0120-y.

[99] F. Del Bene et al., 'Regulation of Neurogenesis by Interkinetic Nuclear Migration through an Apical-Basal Notch Gradient', *Cell* **134**, 1055–1065 (2008).
DOI: 10.1016/j.cell.2008.07.017.

[100] T. Shinoda et al., 'Elasticity-based boosting of neuroepithelial nucleokinesis via indirect energy transfer from mother to daughter', *PLoS Biology* (2018).
DOI: 10.1371/journal.pbio.2004426.

[101] P. C. Spear and C. A. Erickson, 'Interkinetic nuclear migration: A mysterious process in search of a function', *Development Growth and Differentiation* **54**, 306–316 (2012).
DOI: 10.1111/j.1440-169X.2012.01342.x.

[102] P. J. Strzyz et al., 'Interkinetic Nuclear Migration Is Centrosome Independent and Ensures Apical Cell Division to Maintain Tissue Integrity', *Developmental Cell* **32**, 203–219 (2015).
DOI: 10.1016/j.devcel.2014.12.001.

[103] T. Miyata et al., 'Interkinetic nuclear migration generates and opposes ventricular-zone crowding: insight into tissue mechanics', *Frontiers in Cellular Neuroscience* **8**, 473 (2015).
DOI: 10.3389/fncel.2014.00473.

[104] K. Hori, A. Sen and S. Artavanis-Tsakonas, 'Notch signaling at a glance', *Journal of Cell Science* **126**, 2135–2140 (2013).
DOI: 10.1242/jcs.127308.

[105] R. I. Dorsky, D. H. Rapaport and W. A. Harris, 'Xotch inhibits cell differentiation in the xenopus retina', *Neuron* **14**, 487–496 (1995).
DOI: 10.1016/0896-6273(95)90305-4.

[106] V. Aggarwal, R. B. Dickinson and T. P. Lele, 'Concentration Sensing by the Moving Nucleus in Cell Fate Determination: A Computational Analysis', *PLoS ONE* **11** (2016).
DOI: 10.1371/journal.pone.0149213.

[107] Z. Xie et al., 'Cep120 and TACCs Control Interkinetic Nuclear Migration and the Neural Progenitor Pool', *Neuron* **56**, 79–93 (2007).
DOI: 10.1016/j.neuron.2007.08.026.

[108] J.-W. Tsai, K. H. Bremner and R. B. Vallee, 'Dual subcellular roles for LIS1 and dynein in radial neuronal migration in live brain tissue', *Nature Neuroscience* **10**, 970–979 (2007).
DOI: 10.1038/nn1934.

[109] I. Yanakieva et al., 'Tissue shape determines actin-dependent nuclear migration mechanisms in neuroepithelia', *bioRxiv* (2019).
DOI: 10.1101/536698.

[110] J. Schenk et al., 'Myosin II is required for interkinetic nuclear migration of neural progenitors', *Proceedings of the National Academy of Sciences of the United States of America* **106**, 16487–16492 (2009).
DOI: 10.1073/pnas.0908928106.

[111] J.-W. Tsai et al., 'Kinesin 3 and cytoplasmic dynein mediate interkinetic nuclear migration in neural stem cells', *Nature Neuroscience* **13**, 1463–1472 (2010).
DOI: 10.1038/nn.2665.

[112] R. Brown, 'XXVII. A brief account of microscopical observations made in the months of June, July and August 1827, on the particles contained in the pollen of plants; and on the general existence of active molecules in organic and inorganic bodies', *The Philosophical Magazine* **4**, 161–173 (1828).
DOI: 10.1080/14786442808674769.

[113] R. Brown, 'XXIV. Additional remarks on active molecules', *The Philosophical Magazine* **6**, 161–166 (1829).
DOI: 10.1080/14786442908675115.

[114] A. Einstein, 'Über die von der molekularkinetischen Theorie der Wärme geforderte Bewegung von in ruhenden Flüssigkeiten suspendierten Teilchen', *Annalen der Physik* **322**, 549–560 (1905).
DOI: 10.1002/andp.19053220806.

[115] A. Fick, 'Uber Diffusion', *Annalen der Physik* **170**, 59–86 (1855).
DOI: doi.org/10.1002/andp.18551700105.

[116] Paul Langevin, 'Sur la théorie mouvement brownien', *Comptes-rendus de l'Académie des Sciences (Paris)* **146**, 530–533 (1908).

[117] D. S. Lemons and A. Gythiel, 'Paul Langevin's 1908 paper "On the Theory of Brownian Motion" ["Sur la théorie du mouvement brownien," C. R. Acad. Sci. (Paris) 146 , 530–533 (1908)]', *American Journal of Physics* **65**, 1079–1081 (1997).
DOI: 10.1119/1.18725.

[118] R. P. Feynman, R. B. Leighton and M. Sands, *The Feynman Lectures on Physics, Volume I.* 1964, https://www.feynmanlectures.caltech.edu/ (visited on 20/01/2020).

[119] W. Helfrich, 'Elastic Properties of Lipid Bilayers: Theory and Possible Experiments', *Zeitschrift fur Naturforschung - Section C Journal of Biosciences* **28**, 693–703 (1973).
DOI: 10.1515/znc-1973-11-1209.

[120] P. E. Kloeden and E. Platen, 'Numerical Solution of Stochastic Differential Equations', 1 edition (Springer, Berlin, 1992).

[121] A. Azizi et al., 'Interkinetic nuclear migration in the zebrafish retina as a diffusive process', *sub judice* (2019).
DOI: 10.1101/570606.

[122] K. Svoboda and R. Yasuda, 'Principles of Two-Photon Excitation Microscopy and Its Applications to Neuroscience', *Neuron* **50**, 823–839 (2006).
DOI: 10.1016/j.neuron.2006.05.019.

[123] E. H. K. Stelzer, 'Light-sheet fluorescence microscopy for quantitative biology', *Nature Methods* **12**, 23–26 (2015).
DOI: 10.1038/nmeth.3219.

[124] L. Godinho, 'Imaging Zebrafish Development', *Cold Spring Harbor Protocols* **6**, 879–883 (2011).
DOI: 10.1101/pdb.prot5647.

[125] R. Tomer et al., 'Quantitative high-speed imaging of entire developing embryos with simultaneous multiview light-sheet microscopy', *Nature Methods* **9**, 755–763 (2012).
DOI: 10.1038/nmeth.2062.

[126] E. Baumgart and U. Kubitscheck, 'Scanned light sheet microscopy with confocal slit detection', *Optics Express* **20**, 21805–21814 (2012).
DOI: 10.1364/oe.20.021805.

[127] MathWorks, *Matlab*, https://uk.mathworks.com/products/matlab.html.

[128] F. Amat et al., 'Efficient processing and analysis of large-scale light-sheet microscopy data', *Nature Protocols* **10**, 1679–1696 (2015).
DOI: 10.1038/nprot.2015.111.

[129] F. Amat et al., 'Fast, accurate reconstruction of cell lineages from large-scale fluorescence microscopy data', *Nature Methods* **11**, 951–958 (2014).
DOI: 10.1038/nmeth.3036.

[130] C. Wolff et al., 'Multi-view light-sheet imaging and tracking with the MaMuT software reveals the cell lineage of a direct developing arthropod limb', *eLife* **7**, e34410 (2018).
DOI: 10.7554/eLife.34410.

[131] J. Schindelin et al., 'Fiji: An open-source platform for biological-image analysis', *Nature Methods* **9**, 676–682 (2012).
DOI: 10.1038/nmeth.2019.

[132] *Fiji*, https://imagej.net/Fiji/Downloads (visited on 24/02/2020).

[133] J. Icha et al., 'Independent modes of ganglion cell translocation ensure correct lamination of the zebrafish retina', *Journal of Cell Biology* **215**, 259–275 (2016).
DOI: 10.1083/jcb.201604095.

[134] M. H. Zwietering et al., 'Modeling of the bacterial growth curve', *Applied and Environmental Microbiology* **56**, 1875–1881 (1990).

[135] O. Biehlmaier, S. C. F. Neuhauss and K. Kohler, 'Onset and time course of apoptosis in the developing zebrafish retina', *Cell and Tissue Research* **306**, 199–207 (2001).
DOI: 10.1007/s004410100447.

[136] M. Matejčić, G. Salbreux and C. Norden, 'A non-cell autonomous actin redistribution enables isotropic retinal growth', (2018).
DOI: 10.1101/293951.

[137] P. R. Bevington and D. K. Robinson, 'Data Reduction and Error Analysis for the Physical Sciences', 3. edition (McGraw-Hill, 2003).

[138] C. E. Shannon, 'Communication in the Presence of Noise', *Proceedings of the IRE* **37**, 10 –21 (1949).
DOI: 10.1109/JRPROC.1949.232969.

[139] A. Donev et al., 'Unusually dense crystal packings of ellipsoids', *Physical Review Letters* **92**, 255506 (2004).
DOI: 10.1103/PhysRevLett.92.255506.

[140] MathWorks, *Matlab Documentation: pdepe*, https://uk.mathworks.com/help/matlab/ref/pdepe.html.

[141] C. B. Kimmel et al., 'Stages of Embryonic Development of the Zebrafish', *Developmental dynamics* **203**, 253–310 (1995).
DOI: 10.1002/aja.1002030302.

[142] M. Reider and V. P. Connaughton, 'Effects of Low-Dose Embryonic Thyroid Disruption and Rearing Temperature on the Development of the Eye and Retina in Zebrafish', *Birth Defects Research. Part B, Developmental and Reproductive Toxicology* **101**, 347–354 (2014).
DOI: 10.1002/bdrb.21118.

[143] M. Precht and R. Kraft, 'Bio-Statistik 2', 5. edition (De Gruyter, 2015).

[144] D. J. Hartshorne et al., 'The effect of temperature on actomyosin', *Biochimica et Biophysica Acta (BBA) - Bioenergetics* **267**, 190–202 (1972).
DOI: 10.1016/0005-2728(72)90150-8.

[145] W. Hong et al., 'The Effect of Temperature on Microtubule-Based Transport by Cytoplasmic Dynein and Kinesin-1 Motors', *Biophysical Journal* **111**, 1287–1294 (2016).
DOI: 10.1016/j.bpj.2016.08.006.

[146] R. E. Goldstein, 'Are theoretical results ' Results '?', *eLife* (2018).

[147] D. R. Daniels, 'Transport of solid bodies along tubular membrane tethers', *PLoS ONE* **14**, e0210259 (2019).
DOI: 10.1371/journal.pone.0210259.

[148] R. Milo, R. Phillips and N. Orme, 'Cell biology by the numbers' (Garland Science, Taylor & Francis Group, LLC, 2016), http://book.bionumbers.org/.

[149] C. S. Peskin, G. M. Odell and G. F. Oster, 'Cellular Motions and Thermal Fluctuations: The Brownian Ratchet', *Biophysical Journal* **65**, 316–324 (1993).
DOI: 10.1016/S0006-3495(93)81035-X.

[150] M. J. Footer et al., 'Direct measurement of force generation by actin filament polymerization using an optical trap', *Proceedings of the National Academy of Sciences of the United States of America* **104**, 2181–2186 (2007).
DOI: 10.1073/pnas.0607052104.

[151] *Python*, https://www.python.org/.

[152] P. a. Janmey et al., 'From tissue mechanics to transcription factors.' *Differentiation; research in biological diversity* **86**, 112–20 (2013).
DOI: 10.1016/j.diff.2013.07.004.

[153] G. Salbreux, G. Charras and E. Paluch, 'Actin cortex mechanics and cellular morphogenesis', *Trends in Cell Biology* **22**, 536–545 (2012).
DOI: 10.1016/j.tcb.2012.07.001.

[154] P. Chugh and E. K. Paluch, 'The actin cortex at a glance', *Journal of Cell Science* **131**, jcs186254 (2018).
DOI: 10.1242/jcs.186254.

[155] B. Wang et al., 'Anomalous yet Brownian', *Proceedings of the National Academy of Sciences of the United States of America* **106**, 15160–15164 (2009).
DOI: 10.1073/pnas.0903554106.

[156] K. C. Leptos et al., 'Dynamics of Enhanced Tracer Diffusion in Suspensions of Swimming Eukaryotic Microorganisms', *Physical Review Letters* **103**, 198103 (2009).
DOI: 10.1103/PhysRevLett.103.198103.

[157] W. H. Press et al., 'Numerical Recipes. The Art of Scientific Computing', 3 edition (Cambridge University Press, Cambridge, 2007).

[158] MathWorks, *Matlab Documentation: Solving Boundary Value Problems*, https://uk.mathworks.com/help/matlab/math/boundary-value-problems.html.

[159] MathWorks, *Matlab Documentation: bvp5c*, https://uk.mathworks.com/help/matlab/ref/bvp5c.html.

[160] T. R. Powers, G. Huber and R. E. Goldstein, 'Fluid-membrane tethers: Minimal surfaces and elastic boundary layers', *Physical Review E* **65**, 041901 (2002). DOI: 10.1103/PhysRevE.65.041901.

[161] W. Helfrich, 'Steric Interaction of Fluid Membranes in Multilayer Systems', *Zeitschrift für Naturforschung - Section A Journal of Physical Sciences* **33**, 305–315 (1978). DOI: 10.1515/zna-1978-0308.

[162] D. R. Daniels and M. S. Turner, 'Spicules and the Effect of Rigid Rods on Enclosing Membrane Tubes', *Physical Review Letters* **95**, 238101 (2005). DOI: 10.1103/PhysRevLett.95.238101.

[163] C. Cepko, 'Intrinsically different retinal progenitor cells produce specific types of progeny', *Nature Reviews Neuroscience* **15**, 615–627 (2014). DOI: 10.1038/nrn3767.